Highly siderophile element and Os isotope results from the structurally atypical Batin dunite in the Wadi Tayin massif of the Oman ophiolite

Delphine Klaessens, Laurie Reisberg, David Jousselin

Highly siderophile element and Os isotope results from the structurally atypical Batin dunite in the Wadi Tayin massif of the Oman ophiolite

Delphine KLAESSENS[1]*, Laurie REISBERG[1], David JOUSSELIN[1], the Oman Drilling Project Science Team

[1]Centre de Recherches Pétrographiques et Géochimiques, UMR 7358 CNRS -Université de Lorraine, 15 rue Notre Dame des Pauvres, F-54501 Vandoeuvre-lès-Nancy, France

Corresponding author: Delphine KLAESSENS (delphine.klaessens@univ-lorraine.fr)

Key Points

1. The Batin dunite is an exceptionally large dunite, interspersed in the mantle section, discordant to asthenospheric flow.
2. Its major and highly siderophile element composition becomes progressively less fertile with increasing height.
3. Magmas were injected in a late melt pulse at unusual depth, and progressively lost their reactive capacity as they migrated upward.

8156 words

Plain Language Summary

Dunites in ophiolites form by pyroxene dissolution and olivine precipitation during melt-peridotite interaction. Highly siderophile elements (HSE) and Os isotopes are excellent tracers of this process. We present structural and geochemical data on dunites and interspersed harzburgites from borehole BA4A ,of the ICDP Oman Drilling Project in the Batin region (Wadi Tayin massif) of the Oman ophiolite. This region features an exceptionally large dunite body, included in the harzburgitic mantle section. This exploratory study of the Batin dunite shows that it contrasts chemically and structurally with dunites from the Moho Transition Zone and basal section of the ophiolite, but presents similarities with dunitic veins of the main mantle section. Nevertheless, its composition changes systematically with height, becoming progressively less fertile, and depleted in the incompatible HSE, platinum and palladium. We suggest that the Batin dunite formed by interaction of the preexisting harzburgite with a large melt pulse that stagnated at ~1200 meters below the Moho. As these melts ascended through the overlying ~300 meters, their composition was modified through interaction with the harzburgite, eliminating their undersaturation in pyroxene and thus their capacity to form dunite. This may explain the upper limit of the dunite at ~900 meters beneath the Moho.

199 words

Abstract

Dunites in ophiolites form by pyroxene dissolution and olivine precipitation during melt-peridotite interaction. We present structural and geochemical data on peridotites from the Batin region (Wadi Tayin massif) of the Oman ophiolite, where an exceptionally large (~9.5 kilometer long) dunite body was sampled by the ICDP Oman Drilling Project (BA4A borehole). 900-1200 meters beneath the petrological Moho, this dunite is overlain by harzburgite hosting pyroxene-depleted and pyroxene-rich bands. Highly siderophile elements (HSE) and Os isotopes, excellent tracers of melt flow through peridotites, were measured in dunites and interspersed harzburgites from BA4A borehole. The Batin dunite is structurally and chemically distinct from dunites from the Moho Transition Zone and basal section of the ophiolite, resembling instead sparse dunite veins in the main mantle section. Batin dunites have fairly uniform Os, Ir and Ru abundances, but Pd and Pt contents increasing with depth. One deep dunite sample has initial $^{187}Os/^{188}Os$ more radiogenic than MORB. Though the limited number of data demands prudence, we suggest that the Batin dunite formed from a large pulse of radiogenic melts, whose flow was impeded ~1200 meters below the Moho. As these melts ascended, they may have lost their radiogenic character and relative Pt and Pd enrichment through interaction with peridotites, which have much higher HSE contents than melts. Such interaction would also diminish the under-saturation in pyroxene of the melts, eliminating their capacity to sufficiently dissolve the pyroxene of the host harzburgite to form dunite, thus explaining the upper limit of the dunite at ~900 meters.

250 words

Keywords

Oman ophiolite, Mantle, Melt, Dunite, Highly siderophile elements, Osmium isotopes

1. Introduction

The large and well-exposed Oman ophiolite constitutes an ideal laboratory for studying melt migration in the uppermost mantle. Its ~15 kilometer thick mantle section is mainly composed of harzburgite, which hosts a variety of dunite bodies (e.g. Boudier & Coleman (1981)). Ophiolitic dunites are generally viewed as transport pathways for ascending melts (Büchl et al., 2002, 2004; Kelemen et al., 1995; O'Driscoll et al., 2012) resulting from complete pyroxene dissolution and olivine precipitation in the host peridotite by melt-peridotite interactions (Boudier & Nicolas, 1977; Dick, 1977; Kelemen, 1990; Lambart et al., 2009; Morgan & Liang, 2003). An exceptionally large dunite body, which outcrops in the mantle section in the Batin area (Fig. 1), was sampled by the ICDP Oman Drilling Project (Kelemen et al., 2020) (https://www.omandrilling.ac.uk), and constitutes the only dunite body within the harzburgitic section with a size allowing mapping at the 1/25000 to 1/100000 scale. The origin of this highly unusual dunite is still unknown.

Here, we present structural observations and whole-rock geochemical data on eight samples collected in the ICDP BA4A cored borehole traversing the Batin dunite body. These samples, which comprise four dunites each coupled with a nearby host harzburgite, provide information on melt migration and dunite formation. We focus on the highly siderophile elements (HSE), which include the platinum group elements (PGE: Os, Ir, Ru, Rh, Pt, Pd) as well as Au and Re. A particular emphasis is placed on the Re-Os radiometric system, in which ^{187}Re decays to form ^{187}Os ($t_{1/2}$= 41.6 Ga, $\lambda = 1.666 \times 10^{-11}$) (Smoliar et al., 1996). While all of the HSE are siderophile and moderately to extremely chalcophile, they display different bulk behavior during partial melting of the upper mantle (e.g. Fischer-Gödde et al. (2011)): PPGE (platinum-group PGE: Pt, Pd), Au and Re are slightly to moderately incompatible, while IPGE (iridium-group PGE: Os, Ir, Ru, Rh) are highly compatible. This contrasting behavior creates Earth reservoirs with strikingly different Re/Os ratios, which develop with time distinct Os isotope ratios (Shirey & Walker, 1998). Compared to fertile lherzolites, mantle harzburgites typically have similar to slightly higher IPGE abundances, lower PPGE, Au and Re concentrations and unradiogenic Os isotope compositions (cf. summary in Becker & Dale (2016)). In

contrast, recycled oceanic crust and sediments have very low IPGE contents, and are relatively enriched in PPGE, Au and Re, and as a result, are highly radiogenic (Peucker-Ehrenbrink et al., 2003).

Osmium isotopes are particularly useful for studying melt migration through peridotites, and more specifically dunites, because these rocks are very rich in Os compared to typical mantle melts. During melt migration through dunite, the isotopic and elemental compositions of incompatible elements (e.g. light rare earth elements) will be rapidly overprinted in the dunite by equilibration with the magma (Godard et al., 2000; Kelemen et al., 1995), which has much higher concentrations of these elements. For Os (and the other IPGE), however, the mass balance is reversed, allowing gradual changes in Os isotope composition to be recorded in the dunite as melt progressively passes through. We explored this process in an earlier contribution based on a large set of structural observations and geochemical data for peridotites from the Wadi Tayin, Sumail, Nakhl-Rustaq and Haylayn massifs of the southeastern Oman ophiolite (Klaessens et al., 2021). In this previous study, we identified three types of dunite, corresponding to the Moho Transition Zone (MTZ), the main and the basal mantle sections. A strong correlation was observed between the Os isotope compositions of these three types of dunite and their structural contexts. In contrast, the host harzburgites have Os isotope signatures spanning the abyssal peridotite range and not varying systematically with setting. Basal dunites display compositions similar to harzburgite values, while main section dunites have somewhat more radiogenic compositions. MTZ dunites have highly radiogenic compositions similar to those of the overlying lower crust (Peucker-Ehrenbrink et al., 2012), requiring extensive interaction with melts, probably slab-derived, that are more radiogenic than MORB. Such melts cannot have equilibrated with harzburgite or dunite along the path from the source to the Moho, or this radiogenic signature would have been erased. This suggests a very rapid transport mechanism with little melt/rock interaction, possibly hydrofracturing rather than percolation in dunite channels.

Our goal in the current contribution is to determine how, or if, the Batin dunite fits into the highly systematic framework provided by our previous study of dunites from throughout the southeastern Oman ophiolite. We do this by examining the variation of $^{187}Os/^{188}Os$ and HSE abundances with

106 height in this atypical and large dunite body. The results are interpreted in light of the structural
107 relationships between the dunite and the overlying and underlying lithologies, with the aim of
108 understanding the conditions that permitted the formation of such a large mass of dunite within the
109 mantle section. Nevertheless, this study is only exploratory and a more extensive investigation will
110 be needed to fully understand the origin of this intriguing feature and whether it relates to crustal
111 accretion of other processes.

112 ## 2. Geological context

113 ### *2.1. The Oman ophiolite: a fast spreading center above a subducted slab*

114 The Oman ophiolite is a 500 kilometer long, 50-100 kilometer wide nappe divided into 13 structurally
115 continuous massifs (Nicolas, et al., 2000a). It originates from an accretion center in the Neothethys
116 active ~95 Myr ago (Rioux et al., 2012). The ophiolite is underlain by a thin (0-100 meters),
117 discontinuous high-temperature metamorphic sole, formed from relics of the oceanic basin over
118 which the ophiolite was thrust before its obduction onto the continent. This overridden unit has a Lu-
119 Hf metamorphic age of 104 Myr (Guilmette et al., 2018), which substantially predates the accretion
120 age of the overlying spreading center. This chronological information, coupled with lava chemical
121 compositions indicating hydrous magmatic fractionation trends (MacLeod et al., 2013), suggests that
122 the spreading center parental to the ophiolite was active above a subducting oceanic slab.

123 Low temperature deformation ascribed to ophiolite emplacement is restricted to the first few
124 hundred meters of the nappe, often at the base of the mantle section. Most of the ophiolite
125 peridotite section preserves coarse-grained porphyroclastic textures, ascribed to "fossilized"
126 asthenospheric mantle flow, while in the crust, gabbros have a grain shape preferred orientation of
127 euhedral crystals, with no superimposed plastic deformation, thus preserving the imprint of
128 magmatic flow (Nicolas, et al. (2000a) and references therein). Plastic flow lineations in the upper
129 mantle and magmatic lineations in the lower crust are parallel, demonstrating that these flow

structures formed synchronously at the ridge (Nicolas et al., 1994). The sheeted dike complex is generally near vertical, and the crust-mantle interface (referred to hereafter as the Moho) is nearly horizontal, gently dipping to the east in the northern massifs, and to the south and south-east in the southern massifs. The Oman ophiolite can thus be seen as a paleo-oceanic lithosphere, slightly tilted and dissected by erosion, without any important subsequent deformation (Nicolas, 1989; Nicolas & Boudier, 1995). Given its continuous crustal section and the rarity of faults, the ophiolite is thought to derive from a fast spreading center with a permanent magma chamber; a 5 to 10 cm/yr spreading rate is confirmed by U-Pb dating of zircons from the upper gabbros (Rioux et al., 2012). Systematic structural mapping of the southern massifs has revealed a paleoridge organization resembling microplates at the East Pacific Ridge (Boudier et al., 1997). Notably, a distinct change in dike orientation outlines the limits of a NW-SE spreading center (Fig. 1). Several zones characterized by plunging mantle lineations and capped by a thick Moho Transition Zone (MTZ) (see next section), are interpreted as mantle diapirs, underlying the paleo-ridge axis (Jousselin et al., 1998; Nicolas & Boudier, 1995).

2.2. Dunite distribution in the mantle section

The mantle section of the Oman ophiolite is mainly composed of harzburgite but dunitic bodies of various geometries and structural contexts are also observed. Klaessens et al. (2021) identified three types of dunite on the basis of field observations in the southeastern part of the ophiolite, each associated with a specific part of the mantle section. These include:

(1) The Moho Transition Zone (MTZ) (Boudier & Nicolas, 1995; Godard et al., 2000; Klaessens et al., 2021; Koga et al., 2001; Rospabé et al., 2018), a 10-500 meter thick horizontal melt storage and reaction zone, composed of pure and plagioclase/clinopyroxene-impregnated dunites and situated just beneath the crust-mantle interface. This zone is thickest above harzburgite diapirs and represents the largest dunite volume in the ophiolite, as shown on various maps (Glennie et al., 1974; Ministry Petroleum and Minerals of Sultanate of Oman, 1986; Nicolas, et al., 2000a).

(2) Dunitic veins and bands scattered in the harzburgitic main mantle section (MMS) (Bartholomew, 1983; Boudier & Coleman, 1981; Klaessens et al., 2021; Nicolas, et al., 2000b), corresponding to 0-1 meter, rarely up to 5 meters, wide dunitic reaction zones along discordant gabbroic and pyroxenitic dikes. Most crosscut the peridotite foliation (henceforth referred to as "dunite veins").In some cases, the dike fracture closed completely, with all of its melt extracted to shallower levels, leaving only the dunite reaction zone as an indicator of the magma passage. Rare dunites parallel to the foliation are also observed in the MMS (henceforth "dunite bands"), possibly representing examples of dunite veins transposed by mantle flow.

(3) The Basal banded unit (BBU) (Boudier & Coleman, 1981; Klaessens et al., 2021; Lippard et al., 1986), a highly deformed mantle unit near the basal thrust hosting abundant, 0-20 meter thick, concordant dunitic bands. In some cases, orthopyroxene-depleted harzburgite is found instead of dunite. While these bands present spectacular outcrops such as near the capital Mascate, they are difficult to map at scales larger than 1/10000 and represent a minor volume of dunite in comparison to the MTZ. Their high concentration in the BBU is poorly understood.

2.3. Study area: the Batin dunite

The subject of our study, the Batin dunite located in the eastern Wadi Tayin massif (Fig. 1a), does not fit into any of the three types of dunites defined above. This dunite body is exceptionally large, ≤250 meter thick, ~9.5 kilometer long and 2 kilometer wide (Fig. 1b), dips slightly towards the south-east, and is elongated perpendicular to the lineation. In this region, the sheeted dike complex is vertical, striking N-S, and mantle flow is horizontal with a lineation direction of ~N70. A mantle diapir has been mapped at the northern end of the dunite body, centered on 22°57'N-58°40'E (Ildefonse et al., 1993), prompting the question of whether the dunite body could correspond to the MTZ above the diapir. However, the diapir is not centered on this thick dunite body, and our complementary mapping of the area shows that the Batin dunite is overlain by ~900 meters of harzburgite beneath the Moho (Fig. 1c). A ridge axis (the Khazinah-Batin segment) has been associated with the diapir; its estimated location based on radiogenic dating, with increasing ages on each side (Rioux et al., 2012),

coincides with the structural limit between upper gabbro foliations dipping to the east (east flank) or dipping to the west (west flank) (Nicolas & Boudier, 2015). This axis is oriented N-S (parallel to the sheeted dikes), mostly along the 58°37'E longitude; thus placing the Batin dunite 1 (in the north) to 9 (in the south) kilometers east of the axis.

Nearly 5 kilometers southeast of the southern tip of the Batin dunite, the Moho dips slightly to the south, overlying a very thin MTZ (~1-3 meters) (Fig. 1b, southernmost orange observation point, and Fig. 2a). Heterogeneous harzburgite, containing pyroxene-rich patches as well as pyroxene-depleted layers (orange dots in Fig. 1b; Fig. 1c), is dominant between this thin MTZ and the Batin dunite. Dunite crops out near the BA4A borehole in the form of lenses. This dunite is crosscut by numerous gabbroic and pyroxenitic dikes (Fig. 1c, 2b), and includes some harzburgite clasts (Fig. 2e). To the north of the BA site, dunite dominates the landscape (Fig. 2c, 2d) and continues to contain coarse-grained harzburgite clasts (brown dots in Fig. 1b). Further north, beneath the Batin dunite, dunite is interlayered with harzburgite, in the form of veins, semi-concordant bands, lenses or breccia (purple dots in Fig. 1b; Fig. 1c, 2d, 2f) until the basal banded unit (located further north off the map). The Batin dunite was sampled by the ICDP Oman Drilling Project (Kelemen et al., 2020) (https://www.omandrilling.ac.uk) in the BA borehole series (Fig. 1b), mainly dedicated to studies of serpentinization processes.

3. Samples and analytical techniques

3.1. BA hole and sample description

The BA site consists of three cored boreholes, BA1B, BA3A and BA4A (Fig. 1b) (Kelemen et al., 2020) (https://www.omandrilling.ac.uk). As the rocks dip gently towards the southeast, the southernmost hole, BA3A, is closest to the Moho and structurally overlies the middle hole, BA1B, which in turn structurally overlies BA4A, the hole from which our samples are taken. The 300 meter long BA3A hole is mainly composed of harzburgite (Fig. 3) overlying the Batin dunite. The 400 meter long BA1B

hole begins in dunite, corresponding to a smaller dunitic body with harzburgite intervals located above the main Batin dunite (Fig. 3); below a depth of ~160 meters, this hole is dominated by harzburgite, sometimes crossed by dunite veins or lenses (0.05-2 meter thick). The 300 meter long BA4A hole was drilled ~700 meters to the NW of the BA1B hole, at the southern tip of the large Batin dunite; in other words, the first meters of the BA4A hole drill the summit of the buried extension of this dunite. BA4A hole mainly contains dunite, intersected with decametric to metric harzburgite (Fig. 3), with a maximum continuous dunitic thickness of ~26 meters.

In this study, we present major element, highly siderophile element (HSE: Os, Ir, Ru, Pt, Pd, Re) and Os isotopic data for four dunites and four harzburgites (chosen for freshness and very low vein and crack contents) from the BA4A hole; these "harzburgite/dunite pairs" were collected at ~100 meter intervals (Table 1 and Fig. 3). Harzburgites were sampled at distances varying from 3 to 20 meters from their corresponding dunites (Table 1). Batin harzburgites are moderately serpentinized with coarse-grained porphyroclastic textures. Harzburgite BA4A 10 (near 200 meters depth) is visually depleted in orthopyroxene, relative to the 20-25% common orthopyroxene content of Oman harzburgites (Godard et al., 2000), while the shallowest harzbugite BA4A 1 contains aggregates of small orthopyroxene grains with concave and serrated boundaries, suggesting they are partially dissolved by circulating melt, as observed in some harzburgite relics in the MTZ (Boudier & Nicolas, 1995). Dunites are moderately to very strongly serpentinized (sample BA4A 2 in particular). They display high-temperature porphyroclastic and granular textures; dunite BA4A 5 shows annealed textures with large overgrown olivine crystals (up to 1 centimeter).

3.2. Analytical methods

Whole-rock major element concentrations were measured by the SARM at the CRPG laboratory (Nancy, France) using an ICP-OES iCap6500 (Carignan et al., 2001). Uncertainties vary from <2% for SiO_2 to <20% for MnO, based on the concentrations presented in Table 1. After chemical separation, HSE and Os isotopic analyses (Table 2 and Supplementary Tables 1-3) were done at CRPG by MC-ICP-

MS (ThermoScientific Neptune +) (Ir, Ru, Pt, Pd and Re), and N-TIMS using a Finnigan MAT262 mass spectrometer (Os). Details of analytical methods are provided in the Supplementary Material.

4. Results

Batin harzburgite major element compositions are coherent with those of other Oman harzburgite samples (Godard et al., 2000; Hanghøj et al., 2010; Klaessens et al., 2021), except for their slightly higher water contents (LOI = 12.41-14.01 wt.%) (Table 1). Their Mg# (0.904-0.911), Al_2O_3 contents (0.45-0.74 wt.%) and Os concentrations (3.63-6.1 ppb) are confined to a limited range (Table 2 and Fig. 4, 5a). A negative correlation exists between Al_2O_3 and MgO contents (recalculated on a volatile-free basis) in Fig. 4a. Batin harzburgites have unradiogenic Os isotopic compositions ($^{187}Os/^{188}Os_{95Ma}$ = 0.1167-0.1286) in the range of those of abyssal peridotites (Day et al., 2017) (Fig. 5a); all Os isotope ratios have been corrected for radiogenic ingrowth since ophiolite emplacement at 95 Ma. Harzburgite CI chondrite (Horan et al., 2003) normalized HSE abundances display mostly flat patterns broadly similar to Primitive Upper Mantle (PUM) estimates (Becker et al., 2006; Day et al., 2017) (Table 2 and Fig. 6a-b). Harzburgite IPGE abundances plot towards the high end of the range observed elsewhere in the Oman ophiolite (Ahmed & Arai, 2002; Hanghøj et al., 2010; Klaessens, 2021; Lorand et al., 2009), while their PPGE and Re concentrations are more variable. The shallow harzburgite BA4A 1 shows a moderate enrichment in Pt and Pd and especially in Re. In contrast, other harzburgites, and particularly BA4A 6 (near 100 meters depth), are depleted in PPGE and Re. In addition, harzburgite BA4A 6 displays a V-shaped figure for the IPGE Os-Ir-Ru, suggesting the presence of Platinum Group Minerals (PGM) rich in Ru and Os (e.g. laurite RuS_2 and erlichmanite OsS_2). This harzburgite also has an unradiogenic Os isotopic composition ($^{187}Os/^{188}Os_{95Ma}$ = 0.1167), arguing for extensive melt extraction more than 1 billion years ago, which could explain its low Re content.

Batin dunites have somewhat higher water contents (LOI = 15.38-17.51 wt.%) than dunites and harzburgites from elsewhere in the Oman ophiolite (Godard et al., 2000; Hanghøj et al., 2010;

Klaessens et al., 2021). Nevertheless, their volatile corrected major element contents fall on trends defined by peridotites from throughout the ophiolite. Their Al_2O_3 contents (0.17-0.46 wt.%) and Mg# (0.890-0.902) (Table 1 and Fig. 4) are lower than those of the harzburgites, and are similar to those of the MMS dunites. Their Al_2O_3 and MgO contents correlate negatively along the extension of the harzburgite trend (Fig. 4a). In contrast with the harzburgites, the position of each dunite on the trend is a function of the dunite depth, with the lowest Al_2O_3 and highest MgO contents found in the shallow dunite BA4A 2, while the highest Al_2O_3 and lowest MgO contents occur in the deepest dunite BA4A 14. As they are composed almost exclusively of olivine, Batin dunites, with the exception of sample BA4A 14, are aligned along the olivine composition line, which assumes that FeO + MgO = 66.67 mol%, in Fig. 4b. Their Os concentrations (3.40-5.46 ppb; Table 2; Fig. 5b) are fairly constant and in the range of those observed in the Oman MMS and basal dunites (Hanghøj et al., 2010; Klaessens et al., 2021), but clearly higher than those of the MTZ dunites (Klaessens et al., 2021; Xiong et al., 2020a, 2020b). The $^{187}Os/^{188}Os_{95Ma}$ ratios of the Batin dunites range from 0.1220 to 0.1373 and are similar to those of the MMS dunites (Klaessens et al., 2021). Sample BA4A 11 (near 200 meters depth) is quite different from the other Batin dunites: its Mg# is lower (0.890 vs. 0.898-0.902) (Fig. 4a) and its Os isotopic composition is more radiogenic ($^{187}Os/^{188}Os_{95Ma}$ = 0.1354-0.1373 vs. 0.1220-0.1302) (Fig. 5b). In harzburgite/dunite pairs, dunites are more radiogenic than their corresponding harzburgites with the exception of the BA4A 1/BA4A 2 pair located near the surface (Fig. 5c). Because of sampling constraints, harzburgites and dunites from the same pair were not always collected in close proximity (3-20 meters separation) (Table 1). As shown by tightly spaced sampling of other ophiolites (Haller et al., 2021; O'Driscoll et al., 2018; Snortum & Day, 2020) large Os isotope variations can occur between harzburgites separated by a few meters or even centimeters. The relatively large separation between each dunite and its paired harzburgite thus implies that the compositions of the harzburgites do not necessarily represent those of the harzburgites parental to the associated dunites. Batin dunites display relatively homogenous chondrite normalized HSE abundance patterns (Table 2 and Fig. 6a-b), which contrast with the great variety of HSE spectra

281 determined for dunites from elsewhere in the ophiolite, including those from the Wadi Tayin massif
282 (Hanghøj et al., 2010; Klaessens, 2021). Unlike other Oman dunites, the Batin dunites are enriched in
283 Pd (and Pt); this enrichment increases with depth (Fig. 6c-d). A V-shaped figure for the IPGE Os-Ir-Ru
284 is also observed with lower Ir abundances and generally higher Os concentrations than estimated
285 PUM values (Becker et al., 2006) (Fig. 6a-b). Shallow dunite BA4A 2 has, like its adjacent harzburgite,
286 a higher Re concentration than the other Batin dunites. In contrast, dunite BA4A 5 (near 100 meters
287 depth) shows the lowest Pt and Re abundances of Batin dunites, consistent with the low abundances
288 of these elements in its associated harzburgite BA4A 6 (Fig. 6).

289 ## 5. Discussion

290 ### *5.1. Seawater contamination versus Magmatic process*

291 We first consider whether the radiogenic compositions of some Batin dunites result from
292 hydrothermal circulation of seawater. Seawater had high $^{187}Os/^{188}Os$ (~0.51–0.57 in the mid-
293 Cretaceous; Ravizza et al. (2001)), so hydrothermal alteration or serpentinization could potentially
294 modify $^{187}Os/^{188}Os$ in these oceanic peridotites. Many authors have considered whether such
295 secondary processes could explain radiogenic compositions observed in peridotite samples;
296 arguments are summarized in Becker & Dale (2016). Seawater has a very low Os concentration (~10
297 fg/g) (Levasseur et al., 1998), implying that extremely high water/rock ratios (>1000) are needed to
298 significantly change Os compositions of peridotites. In ophiolitic peridotites, these ratios are almost
299 always <100 (McCulloch et al., 1981), so significant modification of $^{187}Os/^{188}Os$ should be rare.

300 Our samples have water contents (LOI < 17.5%, most <15.5%) (Table 1) typical of serpentinized
301 peridotites, but slightly higher than those of other Oman peridotites (Godard et al., 2000; Hanghøj et
302 al., 2010; Klaessens et al., 2021). No correlation is observed between this potential indicator of
303 seawater contamination and Os isotope composition (Supplementary Fig. 1a); moreover, the most
304 radiogenic dunite BA4A 11 (near 200 meters depth) has the lowest LOI value among the Batin

dunites. Another indicator of seawater contamination is the Th/U ratio (e.g. Sanfilippo et al. (2016)), because the Th/U ratio of seawater (~1.5×10^{-6}) is ~6 orders of magnitude lower than that of typical peridotite (~3). A simple two-component mixing model (details and parameters in Supplementary Material) was used to determine the variation of $^{187}Os/^{188}Os$ with Th/U in peridotite with increasing seawater circulation (Supplementary Fig. 1b). For seawater contamination to raise the $^{187}Os/^{188}Os$ ratio of a dunite with 4 ppb Os from a typical peridotitic value of ~0.124 to the most radiogenic composition measured in the Batin dunites (~0.136, sample BA4A 11), a water/rock ratio of >10 000 would be required, which would lower the Th/U ratio of this sample to ~0.0003. Though Th and U data are unfortunately not available for this sample, Aupart et al. (in revision) analyzed an immediately adjacent sample (their number BA4A 80-4 (44-49)) and obtained a Th/U ratio of 2.16, implying very low water/rock ratios in this part of the borehole. Other dunites analyzed by these authors from the BA4A hole, as well as harzburgites from BA3A and BA1B holes, have Th/U ratios of 0.1-3.8, implying water/rock ratios <50, which are much too low to significantly modify peridotite $^{187}Os/^{188}Os$ ratios. This is coherent with Th/U results from elsewhere in the ophiolite which imply water/rock ratios of <100 even in dunites with highly radiogenic Os compositions (Klaessens et al., 2021).

These considerations argue strongly that the Os isotope signatures of the Batin samples reflect essentially magmatic processes. While the evidence in favor of stability of PGE abundances during serpentinization is more equivocal than for Os isotopes, similarity in PGE abundances between variably serpentinized samples is often used to argue that the effects of this process are minimal (Becker & Dale, 2016). Furthermore, sulfides, which are the main PGE host phase, are expected to be stable under the reducing conditions typical of serpentinization in ophiolites (e.g. O'Driscoll et al. (2015)). For these reasons, we will assume, as most previous authors have done, that the PGE abundances in our peridotites were primarily controlled by magmatic processes. Rhenium abundances, on the other hand, may be more problematic, as Re is a fluid mobile element. It is thus possible that the elevated Re contents of some of the Batin samples may result from late Re addition

rather than magmatic processes. However, in all cases the $^{187}Re/^{188}Os$ ratios are sufficiently low that radiogenic ingrowth over the past 95 Ma does not influence interpretation of the Os isotope data.

5.2. Record of ancient partial melting event

The Batin harzburgites have major element contents (Fig. 4), Os isotope compositions (Fig. 5) and CI chondrite normalized HSE abundance patterns (Fig. 6) similar to those of harzburgites from elsewhere in the Oman ophiolite (Ahmed & Arai, 2002; Godard et al., 2000; Hanghøj et al., 2010; Klaessens, 2021; Klaessens et al., 2021; Lorand et al., 2009) and more generally, those of abyssal peridotites (Becker & Dale, 2016; Day et al., 2017). The $^{187}Os/^{188}Os_{95\ Ma}$ ratios of these harzburgites are slightly (~0.128; BA4A 1) to greatly (~0.117; BA4A 6) lower than estimates for the PUM (~0.1285 at 95 Ma; Day et al. (2017); Meisel et al. (2001)), indicating that (with the possible exception of BA4A 1) they experienced one or more ancient partial melting events that predated formation of the ophiolite sequence by hundreds of millions of years. Though the ancient nature of these episodes can be directly inferred only from their Os isotope compositions, such events would also have modified the major element and HSE abundance patterns of these samples. Thus, the compositional variations observed in the harzburgites probably reflect superposition of the effects of melting at the Oman ridge axis on peridotites that were already heterogeneous. Harzburgite BA4A 6 (near 100 meters depth) has the lowest Al_2O_3 content and highest MgO content of all of the harzburgites studied, indicating a high degree of melt extraction. This sample displays a marked V-shaped figure for the IPGE (Os-Ir-Ru) portion of its HSE pattern, coupled with a depletion in PPGE and Re (Fig. 6). These observations suggest that partial melting of this sample was extensive enough to remove nearly all base metal sulphides (BMS) and form Ru and Os-rich PGM (e.g. RuS_2 laurite and OsS_2 erlichmanite) by precipitation and/or exsolution. Furthermore, experimental data indicate that Ru, Os and Ir are moderately compatible in olivine and chromite (Brenan et al., 2016) while Pd, Pt and Re are incompatible. Thus, it can be hypothesized that, after sulfide exhaustion, Ru and Os were retained in laurite/erlichmanite, olivine and chromite, Ir was retained mostly in olivine and chromite, while Pt,

356 Pd and Re were largely removed. Nevertheless, this suggestion should be verified by careful *in situ*
357 studies.

358 The very unradiogenic Os isotopic composition ($^{187}Os/^{188}Os_{95Ma}$ = 0.1167) of harzburgite BA4A 6
359 corresponds to a Re-depletion model age (T_{RD}) of ~1.7 Ga (using PUM mantle evolution curve of
360 Meisel et al. (2001)). This represents a minimum age for the melt extraction event evident in the HSE
361 and major element systematics of this sample. In Fig. 6c, a rough correlation is observed between the
362 $^{187}Os/^{188}Os_{95Ma}$ and the Pd/Ir ratios of the Batin harzburgites. It is possible that, at approximately 1.7
363 Ga, one or more melting events caused the Batin harzburgites to become variably depleted in PPGE
364 and Re, leading to a correlation between Re/Os and Pd/Ir, and over time to the development of the
365 observed correlation between Pd/Ir and $^{187}Os/^{188}Os$ by radioactive decay of ^{187}Re, though we stress
366 that this interpretation is speculative and based on very few data. These ancient events would be
367 completely unrelated to the formation of the Batin dunite, which is a late-stage feature, as shown by
368 its elongation perpendicular to the lineation. Though this correlation may have been modified by
369 additional melting during formation of the ophiolite sequence at ~95 Ma, traces of the original
370 relationship remain. In theory, it would be more straightforward to consider the relationship
371 between $^{187}Os/^{188}Os_{95Ma}$ and Re/Os, and a rough correlation between these parameters in the
372 harzburgites is indeed observed. However, data are available for only three of the four samples, and
373 the Re content of harzburgite BA4A 1 is surprisingly high, suggesting that the Re in this shallowest
374 sample may have been overprinted. Nevertheless, the Re/Os ratio of harzburgite BA4A 6 is indeed
375 the lowest, as expected.

376 ### *5.3. Systematic chemical variations in the Batin dunite*

377 As the preceding discussion indicates, the Oman harzburgites, including those from the Batin area,
378 display chemical and Os isotopic compositions similar to those of abyssal peridotites, and no obvious
379 relationship exists between composition and position of the harzburgites in the ophiolite section. In
380 contrast, the compositions of dunites from throughout the southeastern part of the ophiolite vary
381 systematically with structural setting (literature data in Fig. 5b). This is particularly obvious in their Os

isotope compositions: BBU dunites, at the base of the ophiolite, have low $^{187}Os/^{188}Os_{95Ma}$ ratios indistinguishable from those of nearby harzburgites; MTZ dunites , just below the crust, have highly radiogenic compositions and low Os concentrations; while dunites from the intervening MMS have intermediate Os compositions. These differences in Os composition between the three types of dunites, which are accompanied by more subtle tendencies in major element composition, reflect variations in the extent of melt-rock interaction experienced by dunites in the different parts of the mantle section (Klaessens et al., 2021). This systematic variation provides a framework for interpretation of results from the Batin area.

The Batin dunite is exceptionally large with a maximal thickness of 250 meters (Fig. 1). Elsewhere in the ophiolite, such thick dunite bodies are only found in the MTZ above harzburgite diapirs (Nicolas et al., 1996). However, thick MTZ dunites typically include chromitite pods and layered gabbroic lenses, and the underlying harzburgite displays steeply plunging lineations. None of these features have been reported for the Batin dunite. MTZ dunites (Klaessens et al., 2021; Xiong et al., 2020a, 2020b) have highly variable Mg# (0.897-0.920) and Al_2O_3 contents (0.09-1.71 wt.%), but most samples plot towards the low Mg# and high Al_2O_3 ends of these ranges (Fig. 4). This relatively fertile character cannot be attributed to plagioclase impregnation, as only one of the MTZ dunites is plagioclase bearing. The MTZ dunites also have low Os concentrations (0.4 to 2.3 ppb) and high initial $^{187}Os/^{188}Os$ ratios (0.132 to 0.149) (Fig. 5b). Dunite Os concentrations are expected to decrease progressively during melt-rock interaction, after near total exhaustion of base metal sulfides lowers the bulk rock Os partition coefficient, while $^{187}Os/^{188}Os$ ratios should increase if the melt is more radiogenic than the peridotite (see Klaessens et al. (2021) for modeling). Thus, the very low Os abundances, high $^{187}Os/^{188}Os$ and fertile major element compositions of the MTZ dunites suggest that such interaction processes have been extensive in the MTZ. In contrast, Os abundances in the Batin dunites are rather high (3.4-5.5 ppb) (Fig. 5b and Table 2), and similar to those of harzburgites (3.6-6.1 ppb), while their initial $^{187}Os/^{188}Os$ ratios vary from 0.1220 to 0.1373, and so are lower than those of MTZ dunites (Fig. 5b).

Batin dunite chemistry also differs from that of BBU dunites (Klaessens, 2021; Klaessens et al., 2021). While the Al_2O_3 contents of the Batin dunites are similar to those of the basal unit, their Mg# (0.890-0.902) are distinctly lower than basal dunite values (0.908-0.923) (Fig. 4). The strong PPGE depletion observed in the BBU dunites is absent in the Batin dunites, and the V-shaped figures for the IPGE Os-Ir-Ru chondrite normalized abundances are less pronounced (Fig. 6b). Os isotope ratios of Batin dunites ($^{187}Os/^{188}Os_{95Ma}$ = 0.1220-0.1373) overlap those of the basal dunites (0.1165-0.1280) (Fig. 5b), but tend to be more radiogenic. Unlike at the base of the ophiolite, where dunites and adjacent harzburgites have nearly identical Os isotope compositions (Klaessens et al., 2021), the Batin dunites tend to be more radiogenic than the nearby harzburgites (Fig. 5c).

Thus, the Batin dunites display differences with MTZ and BBU dunites of the ophiolite. Instead, they have major element, HSE and Os isotope compositions similar to those of MMS dunites (Fig. 4-5) (Godard et al., 2000; Hanghøj et al., 2010; Klaessens, 2021; Klaessens et al., 2021; Xiong et al., 2020a, 2020b). The Os concentrations of the Batin dunites (3.4-5.5 ppb; Table 1) are much less variable than those observed in the MMS (1.1-11.8 ppb), but this may simply reflect the collection of the Batin samples in a much more limited zone. This could also explain the limited variability of the Batin dunite chondrite-normalized HSE abundance patterns (Fig. 6a-b). An affinity with MMS dunites from elsewhere in the ophiolite is logical as the Batin dunite is indeed located within the main mantle section. Nevertheless, the Batin body is dramatically larger than the dunite veins and bands seen elsewhere in the MMS.

While the Batin dunites appear to bear some kinship with the MMS dunites from elsewhere in the ophiolite, they show some particular features. In addition to their high IPGE abundances, Batin dunites show enrichment in Pd (from 5.4 to 12.8 ppb) and possibly in Pt (from 7.4 to 9.3 ppb) increasing with depth (Fig. 6). A negative relationship is also observed between Al_2O_3 and MgO contents correlating with depth (Fig. 4a): the deepest dunite BA4A 14 is the richest in Al_2O_3 and PPGE, and the poorest in MgO, while the shallow dunite BA4A 2 contains the lowest Al_2O_3 and PPGE abundances, and the highest MgO contents. The deep dunite BA4A 11 also has a markedly radiogenic

Os isotopic composition (Fig. 5b, 6c). The very shallow harzburgite/dunite pair BA4A 1 and 2 (at 10 and 13 meters respectively; Table 1) is enriched in Re relative to other Batin peridotites (Fig. 6a-b). However, the Re/Os ratio of the dunite is much higher than that of the harzburgite, despite the close similarity of the $^{187}Os/^{188}Os$ ratios of the two lithologies, strongly suggesting recent enrichment in Re in these shallow samples.

5.4. Batin dunite formation

The Batin dunite is unique in the Oman ophiolite because of its exceptionally large size and unusual structural setting, nearly 1 kilometer beneath the Moho. As discussed above, in many respects, the chemical composition of this body resembles those of MMS dunitic veins and bands (Godard et al., 2000; Hanghøj et al., 2010; Klaessens, 2021; Klaessens et al., 2021; Xiong et al., 2020a, 2020b). Nevertheless, not all of the chemical characteristics of the Batin dunite correspond to those of the small MMS dunitic veins. A chemical evolution is observed within the Batin dunite, with more fertile compositions (higher Al_2O_3 and lower MgO contents, as well as higher Pt and Pd abundances) found towards the bottom, evolving to less fertile compositions with increasing height (Fig. 4, 6). Furthermore, orthopyroxene-depleted harzburgite bands instead of dunites are often found in the harzburgite overlying the Batin dunite and may result from interaction with melts insufficiently undersaturated in pyroxene to permit complete removal of this phase.

We present below a model that may explain many of these observations. This model is unavoidably speculative, as it is based on a small number of samples. As several studies have shown (Haller et al., 2021; O'Driscoll et al., 2018; Snortum & Day, 2020), large heterogeneities in Os isotopic composition and HSE abundances can exist on length scales of a meter or less in ophiolites. Therefore, drawing conclusions from a few widely spaced samples may be unwise. Nevertheless, we are struck by the limited variation and surprisingly systematic nature of the dunite HSE patterns, which differ from those seen in dunites from elsewhere in the massif (e.g. Hanghøj et al. (2010); Klaessens (2021)). This relative uniformity may suggest that the magma/rock interaction process that produced the dunites was sufficiently intense to overprint most of the preexisting heterogeneity in the parental

460 harzburgite. We thus suggest that a possible explanation of the existing data is the partial blockage of
461 a large melt volume during its ascent at ~1200 meters below the Moho, forming the base of the Batin
462 dunite by dissolution of the orthopyroxene of the host harzburgite. As these melts slowly continued
463 their migration upwards, their compositions changed through interaction with the harzburgitic
464 precursors and the formation of the thick dunite body, leading to decreasing Al_2O_3 and increasing
465 MgO contents, coupled with a decrease in the degree of melt undersaturation in orthopyroxene. This
466 change in melt composition is evident in the HSE spectra, which suggest that the initial melts were
467 relatively enriched in PPGE, and that this enrichment decreased with continued interaction with the
468 harzburgites as the melts ascended. The elevated $^{187}Os/^{188}Os$ $ratio_{95\ Ma}$ of dunite BA4A 11, one of the
469 two deepest dunites, indicates that these melts were more radiogenic than MORB, and likely similar
470 to those that interacted with MTZ and MMS dunites elsewhere in the ophiolite (Klaessens et al.,
471 2021). As these melts interacted with the peridotite during ascent, they would have become less
472 radiogenic, making them unable to modify the $^{187}Os/^{188}Os$ ratios of the uppermost peridotites, as
473 shown by the isotopic similarity between the shallow dunite BA4A 2 and the nearby harzburgite
474 BA4A 1. If this model is correct, the lack of a systematic, monotonic decrease in $^{187}Os/^{188}Os$ with
475 height may reflect the fact that the melt-peridotite interaction was superimposed on precursor
476 harzburgites that were already heterogeneous (Fig. 5).

477 In this scenario, the top of the dunite may represent the limit above which the melts were no longer
478 sufficiently undersaturated in pyroxene to fully transform harzburgite into dunite. The pyroxene-
479 poor harzburgite bands observed above the dunite could have formed from interaction with such
480 melts. As noted earlier, pyroxene-rich harzburgites are also found above the Batin dunite, which may
481 suggest that some melts became so enriched in the pyroxene component during melt-rock
482 interaction that they reached saturation in this phase. Minor changes in conditions and/or melt
483 composition could then have triggered pyroxene precipitation. Thus, both the pyroxene-depleted
484 harzburgite bands and the pyroxene-rich harzburgite patches in the region above the Batin dunite

485 could potentially be explained by the intensive melt-rock interaction processes that occurred during
486 production of the dunite.

487 The reason for melt blockage at depth, sufficient to produce this massive dunite body, is unclear. As
488 mentioned above, the Batin dunite shows discordant contacts at its upper and lower limits, where
489 some magmatic breccia are observed (Fig. 2e-f). The NE-SW elongation of this body also crosscuts at
490 high angle the asthenospheric mantle lineation; it is thus not transposed by mantle flow. These
491 observations suggest that the giant dunite body was formed when and/or where mantle had stopped
492 flowing, in near-lithospheric conditions. A possible explanation of the melt ponding depth may be its
493 correspondence to the lithosphere-asthenosphere boundary. Melt emplacement away from the
494 accretion center, or as a late magmatic event, during the cooling history of the ophiolite could then
495 explain the abundance of melt at this level.

496 ## 6. Conclusions

497 This exploratory study of the large Batin dunite body shows that it contrasts chemically and
498 structurally with MTZ and basal dunites of the Oman ophiolite, but presents numerous chemical
499 similarities with dunitic veins and bands of the main mantle section. Nevertheless, the composition
500 changes systematically with height, becoming progressively less fertile, and showing decreasing
501 abundances of the incompatible Platinum Group Elements, Pt and Pd. One interpretation of our field
502 and analytical data may be that the Batin dunite formed by interaction of the preexisting harzburgite
503 with a large pulse of melt that stagnated at ~1200 meters below the Moho. As is true elsewhere in
504 the ophiolite, the dunite-forming melts had more radiogenic Os isotopic compositions than MORB, as
505 shown by the high $^{187}Os/^{188}Os$ ratio of one of the deepest dunites. As the melts migrated upwards,
506 interacting with the harzburgite to form dunite, they would have become less radiogenic and their Pt
507 and Pd concentrations would have decreased. They would also have become progressively less
508 undersaturated in pyroxene as they ascended. This suggestion is supported by the bands of

pyroxene-poor harzburgites in the zone above the dunite, which likely formed by interaction with melts that lacked the capacity to fully digest all of the pyroxene present in the original rock.

This simple model is based on a very limited number of samples and will surely evolve as more data become available. Structural and geochemical studies of the lithologies overlying and underlying the dunite will be particularly valuable for improving our understanding of this intriguing feature in the Oman ophiolite.

Acknowledgements

We are very grateful to C. Zimmermann for her helpful assistance during Re-Os chemistry and isotope analyses by N-TIMS and MC-ICP-MS. We also thank C. Parmentier for her help with chemistry, D. Cividini and A. Schumacher for their technical support during MC-ICP-MS sessions, the SARM staff for whole-rock major element analyses, and C. Aupart for her trace element data and BA hole cross-section figure. All the members of the Oman Drilling Project and the Chikyu vessel staff are also warmly thanked with a particular thought for J. A. Coggon, M. Godard and R. Senda. We thank J. Day and E. Rampone for their thorough and constructive reviews, and associate editor J. Lassiter for his helpful comments. Financial support was provided by the TelluS Program of CNRS/INSU. We are highly grateful to the Ministry of Commerce and Industry, Sultanate of Oman, for its hospitality in Oman. Data will be accessible on ORDAR, the OTELo Research Data Repository (https://ordar.otelo.univ-lorraine.fr).

Author Contributions

D. Klaessens, D. Jousselin and L. Reisberg participated in fieldwork and the Oman Drilling Project. D. Jousselin provided geological context. The Oman Drilling Project Science Team supplies samples. D. Klaessens completed most of the analyses and wrote the initial manuscript. L. Reisberg supervised Re-Os analyses. D. Klaessens, L. Reisberg and D. Jousselin discussed the results and their implications, and assisted in the final revisions to the manuscript.

CRediT author statement

Delphine Klaessens: Conceptualization, Methodology, Formal analysis, Validation, Investigation, Visualization, Writing - Original Draft, Writing - Review & Editing

Laurie Reisberg: Conceptualization, Methodology, Investigation, Writing - Review & Editing, Supervision, Funding acquisition

David Jousselin: Conceptualization, Investigation, Writing - Review & Editing, Supervision, Funding acquisition

The Oman Drilling Project Science Team: Resources, Project Administration

Competing Interests statement

None of the authors have competing interests.

References

Ahmed, A. H., & Arai, S. (2002). Unexpectedly high-PGE chromitite from the deeper mantle section of the northern Oman ophiolite and its tectonic implications. *Contributions to Mineralogy and Petrology*, *143*(3), 263–278. https://doi.org/10.1007/s00410-002-0347-8

Aupart, C., Morales, L., Godard, M., Jamtveit, B., & the Oman DP Science Team. (in revision). Microstructures and mass-transfer associated with early faults in peridotites from the Samail Ophiolite, Oman. Under review at EPSL. *Earth and Planetary Science Letters*.

Bartholomew, I. D. (1983). *The primary structures and fabrics of the upper mantle and lower crust from ophiolite complexes*. The Open University, Milton Keynes.

Becker, H., & Dale, C. W. (2016). Re–Pt–Os isotopic and highly siderophile element behavior in oceanic and continental mantle tectonites. *Reviews in Mineralogy and Geochemistry*, *81*(1), 369–440. https://doi.org/10.2138/rmg.2016.81.7

Becker, H., Horan, M. F., Walker, R. J., Gao, S., Lorand, J. P., & Rudnick, R. L. (2006). Highly siderophile

556 element composition of the Earth's primitive upper mantle: Constraints from new data on
557 peridotite massifs and xenoliths. *Geochimica et Cosmochimica Acta*, *70*(17), 4528–4550.
558 https://doi.org/10.1016/j.gca.2006.06.004

559 Boudier, F., & Coleman, R. G. (1981). Cross section through the peridotite in the Samail Ophiolite,
560 southeastern Oman Mountains. *Journal of Geophysical Research: Solid Earth*, *86*(B4), 2573–
561 2592. https://doi.org/10.1029/JB086iB04p02573

562 Boudier, F., & Nicolas, A. (1977). Structural control on the partial melting of the Lanzo peridotite.
563 *AGU Chapman Conf. Proc. Bull. 96*.

564 Boudier, F., & Nicolas, A. (1995). Nature of the Moho Transition zone in the Oman ophiolite. *Journal*
565 *of Petrology*, *36*(3), 777–796. https://doi.org/10.1093/petrology/36.3.777

566 Boudier, F., Nicolas, A., Ildefonse, B., & Jousselin, D. (1997). EPR microplates, a model for the Oman
567 Ophiolite. *Terra Nova*, *9*(2), 79–82. https://doi.org/10.1111/j.1365-3121.1997.tb00007.x

568 Brenan, J. M., Bennett, N. R., & Zajacz, Z. (2016). Experimental results on fractionation of the highly
569 siderophile elements (HSE) at variable pressures and temperatures during planetary and
570 magmatic differentiation. *Reviews in Mineralogy and Geochemistry*, *81*(1), 1–87.
571 https://doi.org/10.2138/rmg.2016.81.1

572 Büchl, A., Brügmann, G. E., Batanova, V. G., & Hofmann, A. W. (2004). Os mobilization during melt
573 percolation: The evolution of Os isotope heterogeneities in the mantle sequence of the Troodos
574 ophiolite, Cyprus. *Geochimica et Cosmochimica Acta*, *68*(16), 3397–3408.
575 https://doi.org/10.1016/j.gca.2004.02.005

576 Büchl, A., Brügmann, G. E., Batanova, V. G., Münker, C., & Hofmann, A. W. (2002). Melt percolation
577 monitored by Os isotopes and HSE abundances: A case study from the mantle section of the
578 Troodos Ophiolite. *Earth and Planetary Science Letters*, *204*(3–4), 385–402.
579 https://doi.org/10.1016/S0012-821X(02)00977-9

580 Carignan, J., Hild, P., Mevelle, G., Morel, J., & Yeghicheyan, D. (2001). Routine analyses of trace
581 elements in geological samples using flow injection and low pressure on-line liquid
582 chromatography coupled to ICP-MS: A study of geochemical reference materials BR, DR-N, UB-
583 N, AN-G and GH. *Geostandards Newsletter*, *25*(2–3), 187–198. https://doi.org/10.1111/j.1751-
584 908x.2001.tb00595.x

585 Day, J. M. D., Walker, R. J., & Warren, J. M. (2017). ^{186}Os–^{187}Os and highly siderophile element
586 abundance systematics of the mantle revealed by abyssal peridotites and Os-rich alloys.
587 *Geochim Cosmochim Acta*, *200*, 232–254. https://doi.org/10.1016/j.gca.2016.12.013

588 Dick, H. J. B. (1977). Evidence of partial melting in the Josephine peridotite. *Bull Oregon Dept Geol*
589 *Mineral Ind*, *96*, 59–62.

590 Fischer-Gödde, M., Becker, H., & Wombacher, F. (2011). Rhodium, gold and other highly siderophile
591 elements in orogenic peridotites and peridotite xenoliths. *Chemical Geology*, *280*(3–4), 365–
592 383. https://doi.org/10.1016/j.chemgeo.2010.11.024

593 Gannoun, A., Burton, K. W., Day, J. M. D., Harvey, J., Schiano, P., & Parkinson, I. (2016). Highly
594 siderophile element and Os isotope systematics of volcanic rocks at divergent and convergent
595 plate boundaries and in intraplate settings. *Reviews in Mineralogy and Geochemistry*, *81*(1),
596 651–724. https://doi.org/10.2138/rmg.2016.81.11

597 Glennie, K. W., Boeuf, M. G. A., Hughes-Clark, M. W., Moody-Stuart, M. N., Pilaar, W. F. H., &
598 Reinhardt, B. M. (1974). *Geology of the Oman Mountains* (K. N. G. M. G. Vern. (ed.); Vol. 31).

599 Godard, M., Jousselin, D., & Bodinier, J. L. (2000). Relationships between geochemistry and structure
600 beneath a palaeo-spreading centre: A study of the mantle section in the Oman ophiolite. *Earth*
601 *and Planetary Science Letters*, *180*(1–2), 133–148. https://doi.org/10.1016/S0012-
602 821X(00)00149-7

603 Guilmette, C., Smit, M. A., van Hinsbergen, D. J. J., Gürer, D., Corfu, F., Charette, B., Maffione, M.,
604 Rabeau, O., & Savard, D. (2018). Forced subduction initiation recorded in the sole and crust of

605 the Semail ophiolite of Oman. *Nature Geoscience*, *11*(September), 688–695.
606 https://doi.org/10.1038/s41561-018-0209-2

607 Haller, M. B., O'Driscoll, B., Day, J. M. D., Daly, J. S., Piccoli, P. M., & Walker, R. J. (2021). Meter-Scale
608 Chemical and Isotopic Heterogeneities in the Oceanic Mantle, Leka Ophiolite Complex, Norway.
609 *Journal of Petrology*. https://doi.org/10.1093/petrology/egab061

610 Hanghøj, K., Kelemen, P. B., Hassler, D., & Godard, M. (2010). Composition and genesis of depleted
611 mantle peridotites from the Wadi Tayin massif, Oman ophiolite; Major and trace element
612 geochemistry, and Os isotope and PGE systematics. *Journal of Petrology*, *51*(1–2), 201–227.
613 https://doi.org/10.1093/petrology/egp077

614 Horan, M. F., Walker, R. J., Morgan, J. W., Grossman, J. N., & Rubin, A. E. (2003). Highly siderophile
615 elements in chondrites. *Chemical Geology*, *196*(1–4), 5–20. https://doi.org/10.1016/S0009-
616 2541(02)00405-9

617 Ildefonse, B., Nicolas, A., & Boudier, F. (1993). Evidence from the Oman ophiolite for sudden stress
618 changes during melt injection at oceanic spreading centres. *Nature*, *366*(6456), 673–675.
619 https://doi.org/10.1038/366673a0

620 Jousselin, D., Nicolas, A., & Boudier, F. (1998). Detailed mapping of a mantle diapir below a paleo-
621 spreading center in the Oman ophiolite. *Journal of Geophysical Research: Solid Earth*, *103*(B8),
622 18153–18170. https://doi.org/10.1029/98JB01493

623 Kelemen, P. B. (1990). Reaction between ultramafic rock and fractionating basaltic magma I. Phase
624 relations, the origin of calc-alkaline magma series, and the formation of discordant dunite.
625 *Journal of Petrology*, *31*(1), 51–98. https://doi.org/10.1093/petrology/31.1.51

626 Kelemen, P. B., Matter, J. M., Teagle, D. A. H., Coggon, J. A., & the Oman Drilling Project Science
627 Team. (2020). *Proceedings of the Oman Drilling Project*.
628 https://doi.org/10.14379/OmanDP.proc.2020

Kelemen, P. B., Shimizu, N., & Salters, V. J. M. (1995). Extraction of mid-ocean-ridge basalt from the upwelling mantle by focused flow of melt in dunite channels. *Nature*, *375*(6534), 747–753. https://doi.org/10.1038/375747a0

Klaessens, D. (2021). *Migration des liquides de fusion et formation des dunites dans le manteau de l'ophiolite d'Oman*. Université de Lorraine.

Klaessens, D., Reisberg, L., Jousselin, D., Godard, M., & Aupart, C. (2021). Osmium isotope evidence for rapid melt migration towards the Moho in the Oman ophiolite. *Earth and Planetary Science Letters*, *572*, 117111. https://doi.org/10.1016/j.epsl.2021.117111

Koga, K. T., Kelemen, P. B., & Shimizu, N. (2001). Petrogenesis of the crust-mantle transition zone and the origin of lower crustal wehrlite in the Oman ophiolite. *Geochemistry, Geophysics, Geosystems*, *2*(9). https://doi.org/10.1029/2000GC000132

Lambart, S., Laporte, D., & Schiano, P. (2009). An experimental study of focused magma transport and basalt-peridotite interactions beneath mid-ocean ridges: Implications for the generation of primitive MORB compositions. *Contributions to Mineralogy and Petrology*, *157*(4), 429–451. https://doi.org/10.1007/s00410-008-0344-7

Levasseur, S., Birck, J. L., & Allègre, C. J. (1998). Direct measurement of femtomoles of osmium and the $^{187}Os/^{186}Os$ ratio in seawater. *Science*, *282*(5387), 272–274. https://doi.org/10.1126/science.282.5387.272

Lippard, S. J., Shelton, A. W., & Gass, I. G. (1986). The Ophiolite of Northern Oman. In *The Geological Society Memoirs* (Vol. 11, p. 178). Backwell Scientific Publications. https://doi.org/10.1144/GSL.MEM.1986.011.01.03

Lorand, J. P., Alard, O., & Godard, M. (2009). Platinum-group element signature of the primitive mantle rejuvenated by melt-rock reactions: evidence from Sumail peridotites (Oman Ophiolite). *Terra Nova*, *21*(1), 35–40. https://doi.org/10.1111/j.1365-3121.2008.00850.x

MacLeod, C. J., Lissenberg, C. J., & Bibby, L. E. (2013). “Moist MORB” axial magmatism in the Oman ophiolite: The evidence against a mid-ocean ridge origin. *Geology*, *41*(4), 459–462. https://doi.org/10.1130/G33904.1

McCulloch, M. T., Gregory, R. T., Wasserburg, G. J., & Taylor, H. P. J. (1981). Sm-Nd, Rb-Sr, and $^{18}O/^{16}O$ isotopic systematics in an oceanic crustal section: Evidence from the Samail Ophiolite. *Journal of Geophysical Research: Solid Earth*, *86*(B4), 2721–2735. https://doi.org/10.1029/JB086iB04p02721

Meisel, T., Walker, R. J., Irving, A. J., & Lorand, J. P. (2001). Osmium isotopic compositions of mantle xenoliths : A global perspective. *Geochim Cosmochim Acta*, *65*(8), 1311–1323.

Ministry Petroleum and Minerals of Sultanate of Oman. (1986). *Geological Map of Oman (1/100 000 and 1/50 000)*.

Morgan, Z., & Liang, Y. (2003). An experimental and numerical study of the kinetics of harzburgite reactive dissolution with applications to dunite dike formation. *Earth and Planetary Science Letters*, *214*(1–2), 59–74. https://doi.org/10.1016/S0012-821X(03)00375-3

Nicolas, A. (1989). *Structures of Ophiolites and Dynamics of Oceanic Lithosphere* (Springer (ed.); Kluwer Aca). https://doi.org/10.1007/978-94-009-2374-4

Nicolas, A., & Boudier, F. (1995). Mapping ridge segments in Oman ophiolite. *Jour. Geophys. Res.*, *100*(B4), 6179–6197.

Nicolas, A., & Boudier, F. (2015). Inside the magma chamber of a dying ridge segment in the Oman ophiolite. *Terra Nova*, *27*(1), 69–76. https://doi.org/10.1111/ter.12130

Nicolas, A., Boudier, F., & Ildefonse, B. (1994). Evidence from the Oman ophiolite for active mantle upwelling beneath a fast-spreading ridge. *Nature*, *370*(6484), 51–53. https://doi.org/10.1038/370051a0

Nicolas, A., Boudier, F., & Ildefonse, B. (1996). Variable crustal thickness in the Oman ophiolite:

677 Implication for oceanic crust. *Journal of Geophysical Research: Solid Earth*, *101*(B8), 17941–
678 17950. https://doi.org/10.1029/96JB00195

679 Nicolas, A., Boudier, F., Ildefonse, B., & Ball, E. (2000a). Accretion of Oman and United Arab Emirates
680 ophiolite – Discussion of a new structural map. *Marine Geophysical Researches*, *21*(3), 147–180.
681 https://doi.org/10.1023/A:1026769727917

682 Nicolas, A., Ildefonse, B., Boudier, F., Lenoir, X., & Ben Ismail, W. (2000b). Dike distribution in the
683 Oman-United Arab Emirates ophiolite. *Marine Geophysical Researches*, *21*(3), 269–287.
684 https://doi.org/10.1023/A:1026718026951

685 Noël, J. (2018). *Etude pétro-structurale et géochimique des processus de serpentinisation et de*
686 *carbonatation des péridotites de l'ophiolite d'Oman*. Université de Montpellier.

687 O'Driscoll, B., Day, J. M. D., Walker, R. J., Daly, J. S., McDonough, W. F., & Piccoli, P. M. (2012).
688 Chemical heterogeneity in the upper mantle recorded by peridotites and chromitites from the
689 Shetland Ophiolite Complex, Scotland. *Earth and Planetary Science Letters*, *333–334*, 226–237.
690 https://doi.org/10.1016/j.epsl.2012.03.035

691 O'Driscoll, B., Walker, R. J., Clay, P. L., Day, J. M. D., Ash, R. D., & Daly, J. S. (2018). Length-scales of
692 chemical and isotopic heterogeneity in the mantle section of the Shetland Ophiolite Complex,
693 Scotland. *Earth and Planetary Science Letters*, *488*, 144–154.
694 https://doi.org/10.1016/j.epsl.2018.02.020

695 O'Driscoll, B., Walker, R. J., Day, J. M. D., Ash, R. D., & Daly, J. S. (2015). Generations of Melt
696 Extraction, Melt–Rock Interaction and High-Temperature Metasomatism Preserved in
697 Peridotites of the ~497 Ma Leka Ophiolite Complex, Norway. *Journal of Petrology*, *56*(9), 1797–
698 1828. https://doi.org/10.1093/petrology/egv055

699 Peucker-Ehrenbrink, B., Bach, W., Hart, S. R., Blusztajn, J. S., & Abbruzzese, T. (2003). Rhenium-
700 osmium isotope systematics and platinum group element concentrations in oceanic crust from
701 DSDP/ODP Sites 504 and 417/418. *Geochemistry, Geophysics, Geosystems*, *4*(7), 1–28.

https://doi.org/10.1029/2002GC000414

Peucker-Ehrenbrink, B., Hanghøj, K., Atwood, T., & Kelemen, P. B. (2012). Rhenium-osmium isotope systematics and platinum group element concentrations in oceanic crust. *Geology*, *40*(3), 199–202. https://doi.org/10.1130/G32431.1

Ravizza, G., Blusztajn, J., & Prichard, H. M. (2001). Re-Os systematics and platinum-group element distribution in metalliferous sediments from the Troodos ophiolite. *Earth and Planetary Science Letters*, *188*(3–4), 369–381. https://doi.org/10.1016/S0012-821X(01)00337-5

Rioux, M., Bowring, S., Kelemen, P. B., Gordon, S., Dudás, F., & Miller, R. (2012). Rapid crustal accretion and magma assimilation in the Oman-U.A.E. ophiolite: High precision U-Pb zircon geochronology of the gabbroic crust. *Journal of Geophysical Research: Solid Earth*, *117*(B7), 1–12. https://doi.org/10.1029/2012JB009273

Rospabé, M., Benoit, M., Ceuleneer, G., Hodel, F., & Kaczmarek, M. A. (2018). Extreme geochemical variability through the dunitic transition zone of the Oman ophiolite : Implications for melt/fluid-rock reactions at Moho level beneath oceanic spreading centers. *Geochim Cosmochim Acta*, *234*, 1–23. https://doi.org/10.1016/j.gca.2018.05.012

Sanfilippo, A., Morishita, T., & Senda, R. (2016). Rhenium-osmium isotope fractionation at the oceanic crust-mantle boundary. *Geology*, *44*(2), 167–170. https://doi.org/10.1130/G37428.1

Shirey, S. B., & Walker, R. J. (1998). Isotope System in Cosmochemistry and High-Temperature Geochemistry. *Annual Review of Earth and Planetary Sciences*, *26*(1), 423–500. https://doi.org/10.1146/annurev.earth.26.1.423

Smoliar, M. I., Walker, R. J., & Morgan, J. W. (1996). Re-Os Ages of Group IIA, IIIA, IVA, and IVB Iron Meteorites. *Science*, *271*(5252), 1099 LP – 1102. https://doi.org/10.1126/science.271.5252.1099

Snortum, E., & Day, J. M. D. (2020). Forearc origin for Coast Range Ophiolites inferred from osmium

isotopes and highly siderophile elements. *Chemical Geology*, *550*, 119723. https://doi.org/https://doi.org/10.1016/j.chemgeo.2020.119723

Xiong, Q., Xu, Y., González-Jiménez, J. M., Liu, J., Alard, O., Zheng, J. P., Griffin, W. L., & O'Reilly, S. Y. (2020a). Sulfide in dunite channels reflects long-distance reactive migration of mid-ocean-ridge melts from mantle source to crust: A Re-Os isotopic perspective. *Earth and Planetary Science Letters*, *531*, 1–10. https://doi.org/10.1016/j.epsl.2019.115969

Xiong, Q., Xu, Y., González-Jiménez, J. M., Liu, J., Alard, O., Zheng, J. P., Griffin, W. L., & O'Reilly, S. Y. (2020b). Corrigendum to "Sulfide in dunite channels reflects long-distance reactive migration of mid-ocean-ridge melts from mantle source to crust: A Re-Os isotopic perspective" [Earth and Planetary Science Letters 531 (2020) 115969]. *Earth and Planetary Science Letters*, *535*, 1. https://doi.org/10.1016/j.epsl.2020.116136

Figure and Table Legends

Figure 1. Oman Drilling Project GT, BT, CM and BA borehole locations in the southeastern massifs (Sumail and Wadi Tayin) of the Oman ophiolite. **(a)** Simplified geological map of the region (after Nicolas, et al. (2000a)) showing the spatial distribution of the Hawasina sediments, the ophiolite crustal section, the Moho Transition Zone (MTZ) and large dunite outcrops, the mainly harzburgitic mantle section and the metamorphic sole. The inferred ridge axis (bold blue lines), mantle diapirs (stars), main dike orientations (double black lines) and limits of NE-SW dikes (black dashed curves) are indicated. **(b)** Enlarged view of the Batin region in the northeastern Wadi Tayin massif, where a large dunite (dark brown) outcrops (after Noël (2018)). Mantle and gabbro lineations (Nicolas, et al., 2000a), 45° foliation isodip (Ildefonse et al., 1993) and the Khazinah-Batin segment (Rioux et al., 2012) are shown. BA cored borehole locations (BA1B, BA3A and BA4A) are indicated (large red dots); studied samples from BA4A hole at the southernmost tip of the exposed part of the dunite body. Smaller dots show field observation sites where harzburgite (orange dots) or dunite (brown dots) is dominant or where both lithologies coexist in roughly equal proportions (purple dots). The Moho and

underlying rocks dip gently to the south, so that the stratigraphic level deepens towards the north. **(c)** SE-NW schematic vertical section (corresponding to a traverse from point X to Y in Fig. 1b) based on field observations in the Batin region, showing the distribution of the lithologies above (point X) and below (point Y) the Batin dunite.

Figure 2. Field photographs illustrating the Moho **(a)**, the Batin dunite **(b-d)**, harzburgite clasts trapped in dunitic vein networks close to this giant dunite **(e-f)** in the study area. **(a)** Moho dipping slightly to the south and overlying a very thin MTZ (1-3 meters). **(b)** Altered dunite summit crosscut by numerous gabbroic and pyroxenitic dikes and sills near the BA4A hole. **(c)** View of dunite irregular summit showing preserved harzburgite clasts (darker) in dunite or indistinguishable depleted harzburgite (lighter) (delimited contacts). G, gravel. **(d)** Lower part: Batin dunite core with massive and highly altered dunite, allowing development of a wide Wadi (river) bordered with flat terraces. Upper part: Batin dunite summit with zones richer in harzburgite, more resistant to erosion, forming reliefs (purple dots in center of Fig. 1b). **(e)** Pyroxene-rich harzburgite clasts trapped in dunitic vein network near upper limit of the Batin dunite. **(f)** Dunitic vein network below the Batin dunite (northernmost observation points of Fig. 1b).

Figure 3. Stratigraphic cross-sections of ICDP BA3A, BA1B and BA4A cored boreholes in the Batin area of the Oman ophiolite illustrating lithologies. Borehole locations are shown in insert and Fig. 1; BA3A hole structurally overlies BA1B, covering BA4A. Data from Kelemen et al. (2020) (https://www.omandrilling.ac.uk). Modified after Aupart et al. (in revision). Samples come from BA4A hole; their locations and lithologies (light orange for harzburgite and brown for dunite) are indicated.

Figure 4. Whole-rock major element compositions of Batin harzburgites and dunites, recalculated on a volatile-free basis, compared with published peridotite data from the Oman ophiolite. **(a)** Al_2O_3 vs. MgO, **(b)** FeO vs. MgO and **(c)** depth vs. Al_2O_3 (for Batin dunites only). In panel **(b)**, dotted grey lines represent constant Mg# values and bold dotted black line shows evolution of olivine composition

776 constrained by FeO + MgO = 66.67 mol% following Godard et al. (2000). Published Oman peridotite
777 data (Godard et al., 2000; Hanghøj et al., 2010; Klaessens et al., 2021) include dunites from the Moho
778 Transition Zone (MTZ), and dunites and harzburgites from the main mantle section (MMS) and the
779 basal banded unit (BBU). Attribution of samples from the literature to the three domains defined in
780 Klaessens et al. (2021) was based on their geographic positions in the mantle section.

781 **Figure 5.** Os isotope compositions of Batin harzburgites and dunites. **(a)** $^{187}Os/^{188}Os$ vs. [Os] in
782 harzburgites; **(b)** $^{187}Os/^{188}Os$ vs. [Os] in dunites; **(c)** Variations in $^{187}Os/^{188}Os$ of dunite/harzburgite
783 pairs (delimited by contours) with depth in BA4A cored borehole. In all panels, pink bands represent
784 estimated $^{187}Os/^{188}Os$ ratio for the Primitive Upper Mantle (PUM) (~0.1289 at 95 Ma (Meisel et al.,
785 2001); coherent with ~0.1285 at 95 Ma from Day et al. (2017)). Light grey, dark grey and brown
786 curves on the sides of diagrams show the probability distribution of $^{187}Os/^{188}Os$ ratios for abyssal
787 peridotites (compilation in Becker & Dale (2016); new data from Day et al. (2017) show a similar
788 distribution), MORB (MORB sulfide data from Gannoun et al. (2016)) and Oman lower crust (Peucker-
789 Ehrenbrink et al., 2012) respectively. Published Oman peridotite data are shown for comparison
790 (Hanghøj et al., 2010; Klaessens et al., 2021; Xiong et al., 2020a, 2020b); symbols as in Fig. 4.
791 Attribution of samples from the literature to the three domains defined in Klaessens et al. (2021) was
792 based on their geographic positions in the mantle section. Data for harzburgites and the three types
793 of dunites from Klaessens et al. (2021) are reported in Supplementary Table 4.

794 **Figure 6.** HSE abundances and Os isotope compositions of Batin harzburgites and dunites. **(a-b)** CI
795 chondrite (Horan et al., 2003) normalized HSE abundances of harzburgites **(a)** and dunites **(b)**. **(c)**
796 $^{187}Os/^{188}Os_{95Ma}$ vs. Pd/Ir. **(d)** [Pd] vs. [Pt]. **(e)** Variations in Batin dunites of Pd content with depth in
797 BA4A cored borehole. In all panels, pink fields represent estimated $^{187}Os/^{188}Os$ ratio and HSE
798 abundances for Primitive Upper Mantle (PUM) from Meisel et al. (2001) and Becker et al. (2006)
799 respectively, while violet fields represent HSE estimates for PUM from Day et al. (2017).
800 Harzburgite/dunite pairs are shown with same colors (filled symbols for harzburgites; open symbols
801 for dunites). Light and dark grey fields in panels **(a-b)** show HSE abundances for harzburgites and

802 dunites from the Oman main (MMS) and basal mantle sections (partially covered by translucent
803 MMS fields) respectively (Klaessens, 2021). In panels **(c-d)**, blue arrows indicate Batin dunite
804 enrichment in Pd and more limited enrichment in Pt increasing with depth. In panel **(c)**, blue dotted
805 line highlights correlation between Pd/Ir and $^{187}Os/^{188}Os$ in harzburgites, consistent with radiogenic
806 ingrowth since ancient partial melting. Published Oman peridotite data are shown for comparison
807 (Hanghøj et al., 2010; Klaessens, 2021; Klaessens et al., 2021) (symbols as in Fig. 4). Attribution of
808 samples reported in the literature to the three domains defined in Klaessens et al. (2021) was based
809 on their geographic positions in the mantle section. Osmium isotope and HSE data of Klaessens
810 (2021) and Klaessens et al. (2021) are reported in Supplementary Tables 4-5.

811 **Table 1.** Whole-rock major element compositions of the studied Batin peridotites

812 **Table 2.** HSE concentrations and Os isotope compositions of the studied Batin peridotites and UB-N
813 and MUH-1 standards

(a)

58°E

Muscat

HAYLAYN

NAKHL-RUSTAQ

Nakhl

BT

SUMAIL

Mansah

Maqsad

BAHLAH

WADI TAYIN

Batin

23°N

CM

GT

BA

0 20 40 km

after Nicolas, et al. (2000a)

ICDP drilling holes (GT, BT, CM and BA)

diapir

inferred ridge axis

main dyke orientations and limit of NE/SW dykes

Tertiary

Hawasina

crust

MTZ and dunite

HT harzburgite

LT harzburgite

metamorphic sole

(b)

Y

58° 40′ E

Wadi Dima

HT mantle lineation

45°

foliation isodip

gabbro lineation

Khazinah-Batin segment

BA4A

BA1B

BA3A

0 5 km

22° 51′ N

X

Field observation point

Main harzburgite

Main dunite

Harzburgite/dunite

Fault

Wadis

after Noël (2018)

(c)

X

0 m

1000 m

2000 m

Y

Moho

Batin dunite

depleted harzburgite

px-rich harzburgite

dunite lens, vein, patch in harzburgite
harzburgite clast in dunite

gabbroic veins

px veins/bands

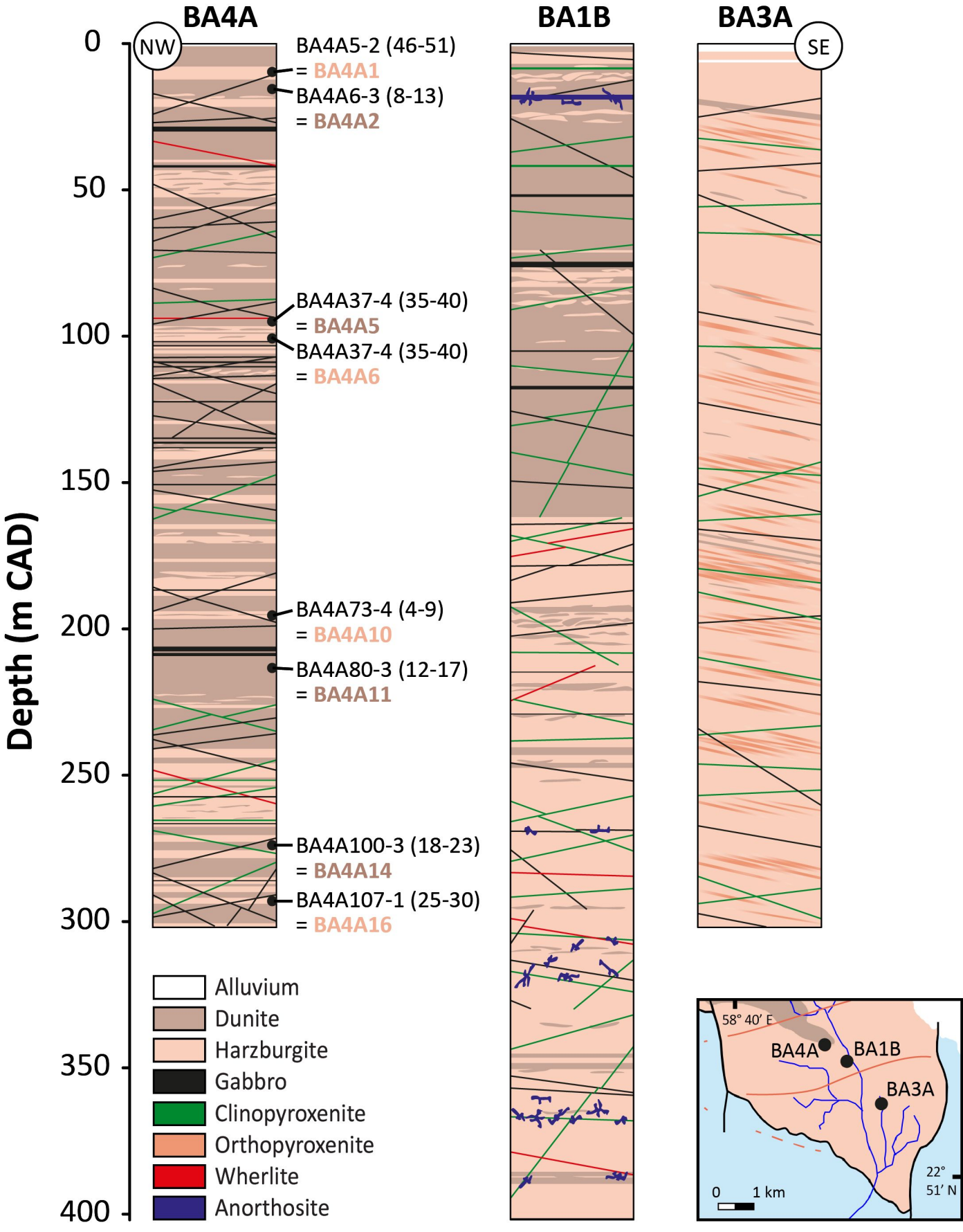
BA4A
BA1B
BA3A
NW
SE
Depth (m CAD)
0
50
100
150
200
250
300
350
400
BA4A5-2 (46-51)
= BA4A1
BA4A6-3 (8-13)
= BA4A2
BA4A37-4 (35-40)
= BA4A5
BA4A37-4 (35-40)
= BA4A6
BA4A73-4 (4-9)
= BA4A10
BA4A80-3 (12-17)
= BA4A11
BA4A100-3 (18-23)
= BA4A14
BA4A107-1 (25-30)
= BA4A16
Alluvium
Dunite
Harzburgite
Gabbro
Clinopyroxenite
Orthopyroxenite
Wherlite
Anorthosite
58° 40′ E
BA4A
BA1B
BA3A
22° 51′ N
0
1 km

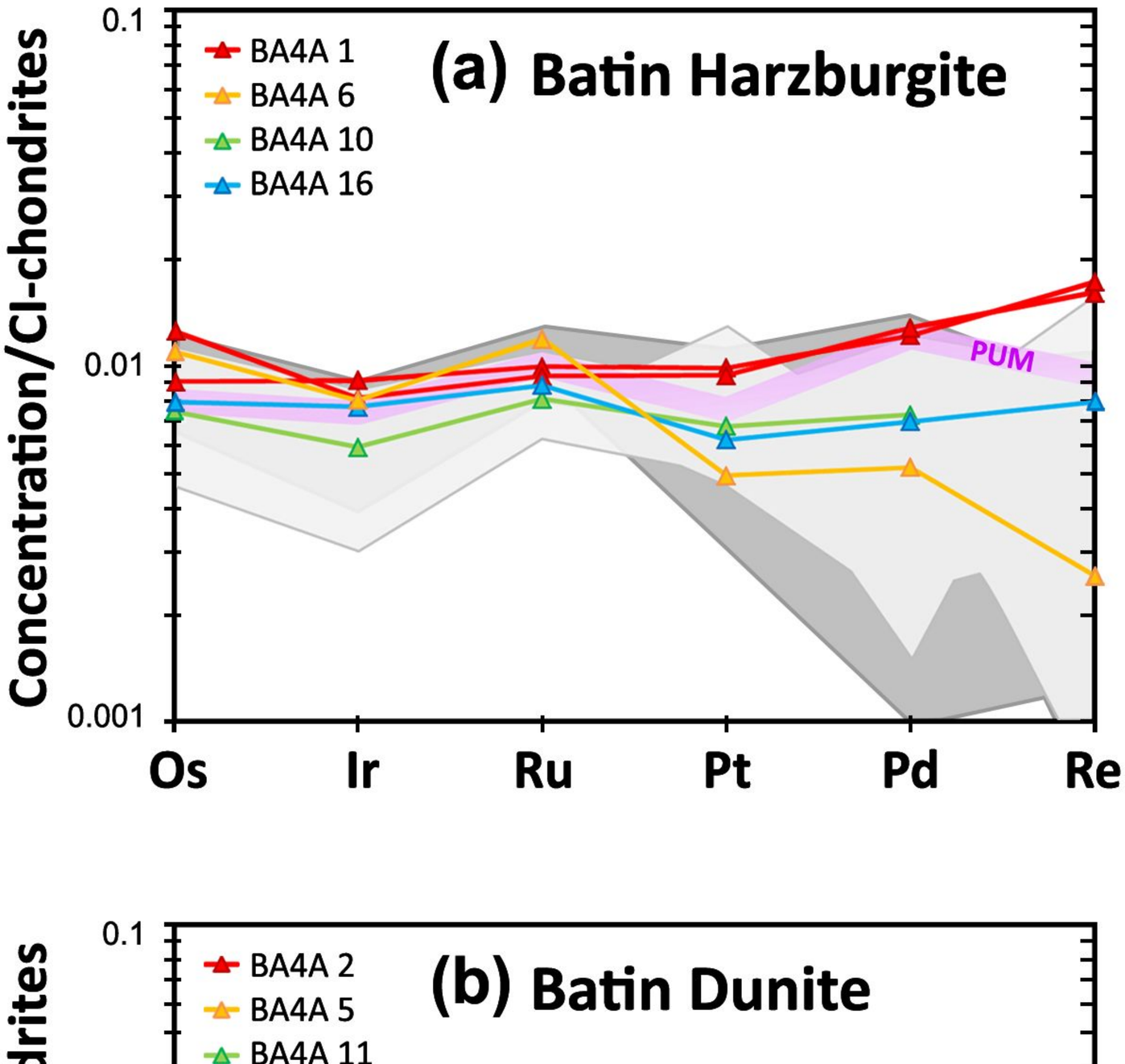
(a) Batin Harzburgite
BA4A 1
BA4A 6
BA4A 10
BA4A 16
PUM
Concentration/CI-chondrites
0.1
0.01
0.001
Os
Ir
Ru
Pt
Pd
Re

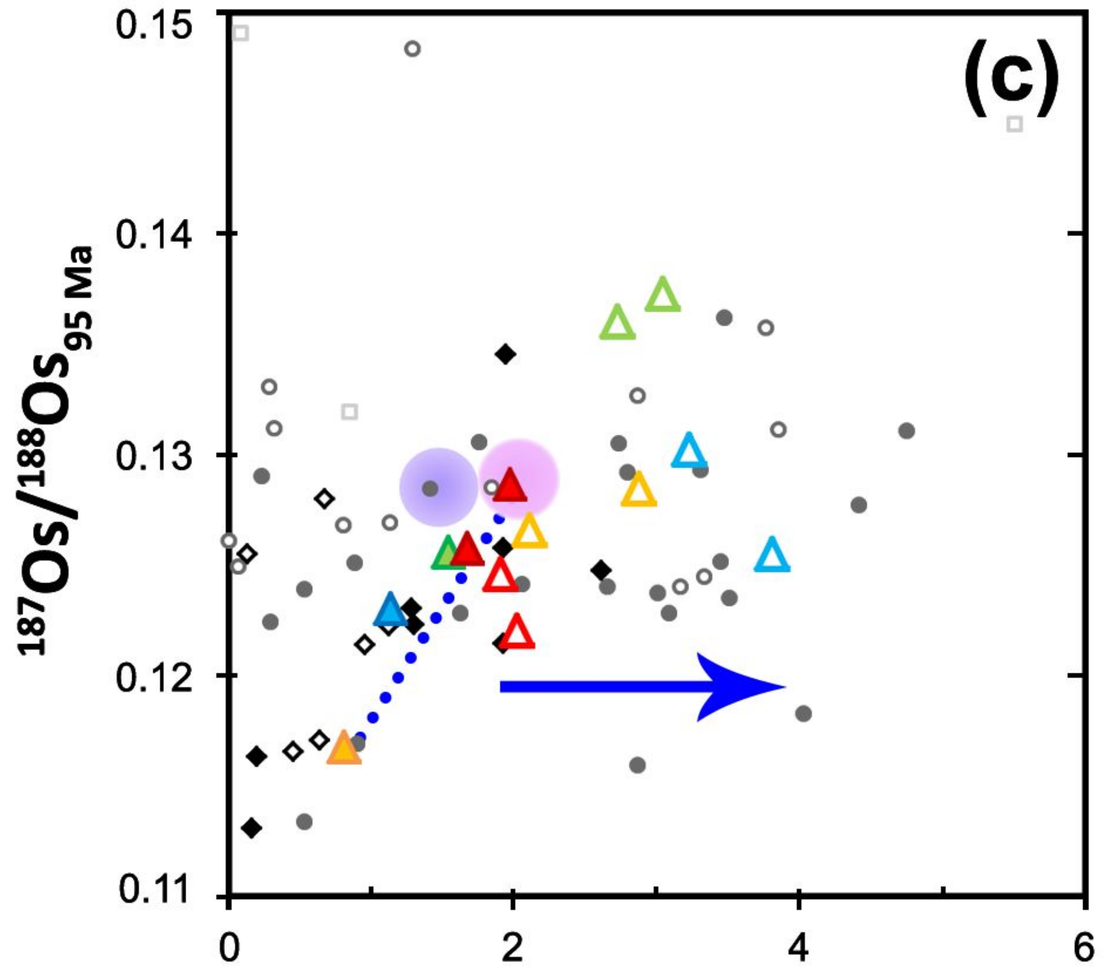
(c)
$^{187}Os/^{188}Os_{95\ Ma}$
0.15
0.14
0.13
0.12
0.11
0
2
4
6
Pd/Ir

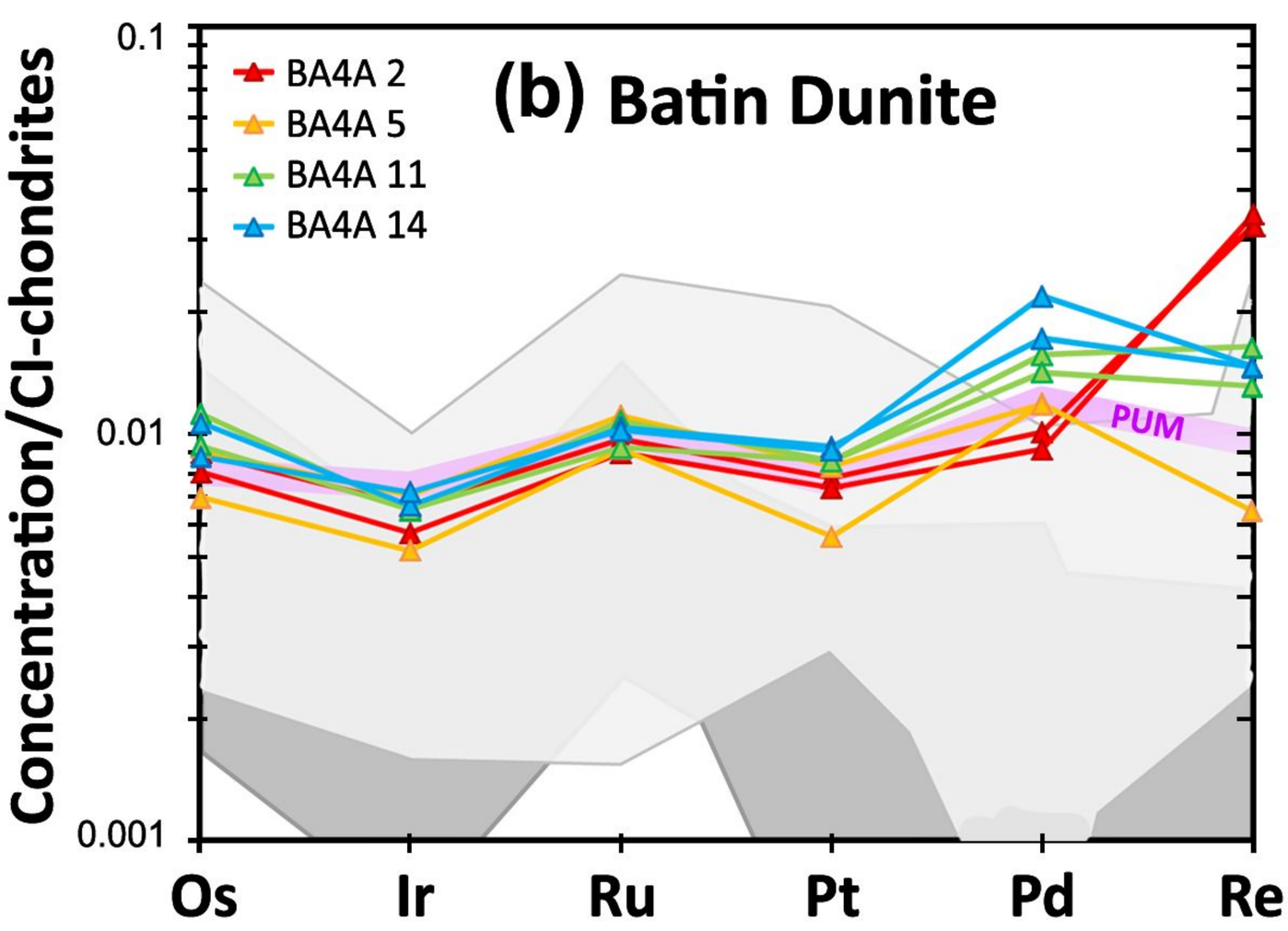
(b) Batin Dunite
BA4A 2
BA4A 5
BA4A 11
BA4A 14
PUM
Concentration/CI-chondrites
0.1
0.01
0.001
Os
Ir
Ru
Pt
Pd
Re

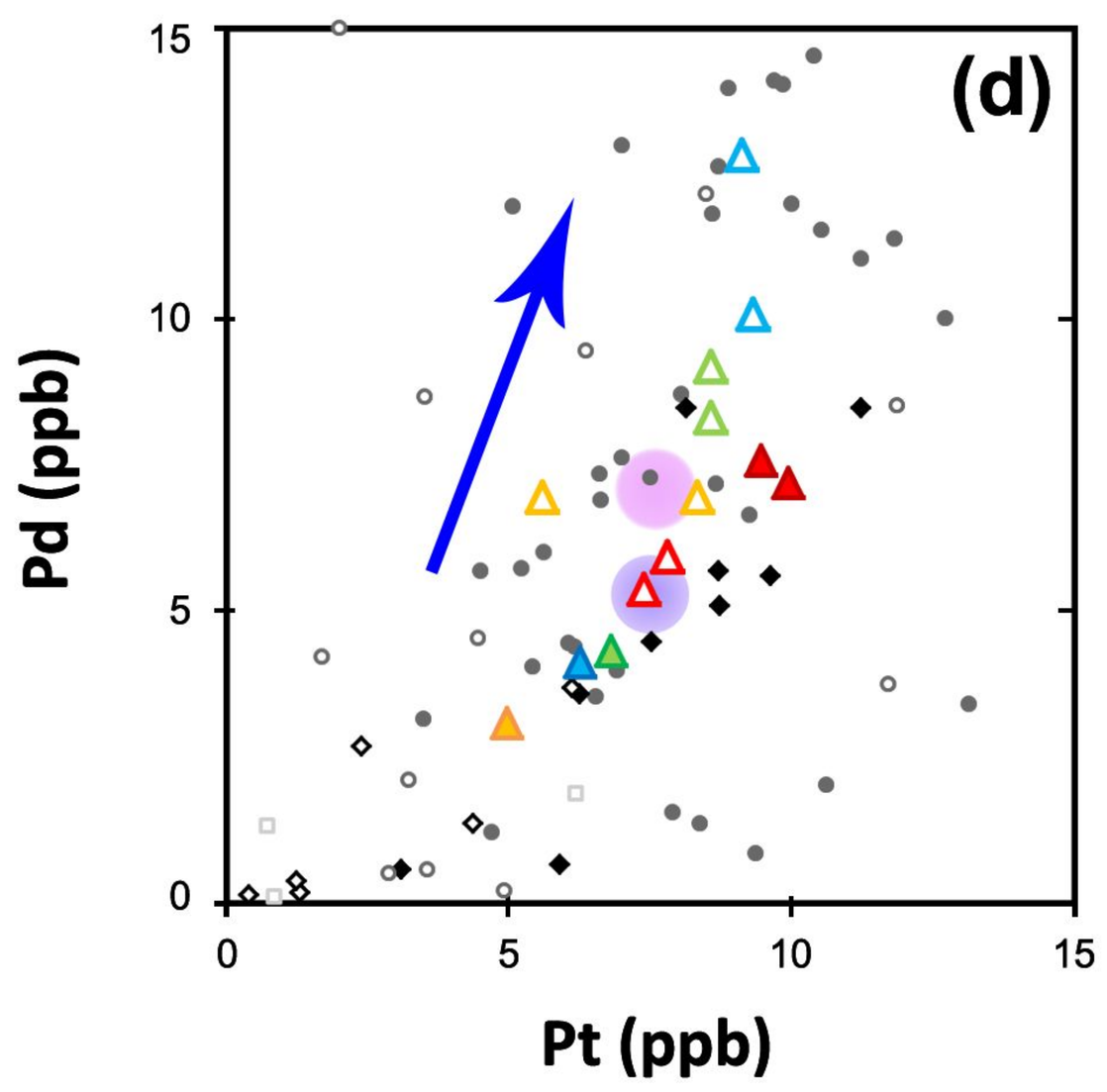
(d)
Pd (ppb)
15
10
5
0
0
5
10
15
Pt (ppb)

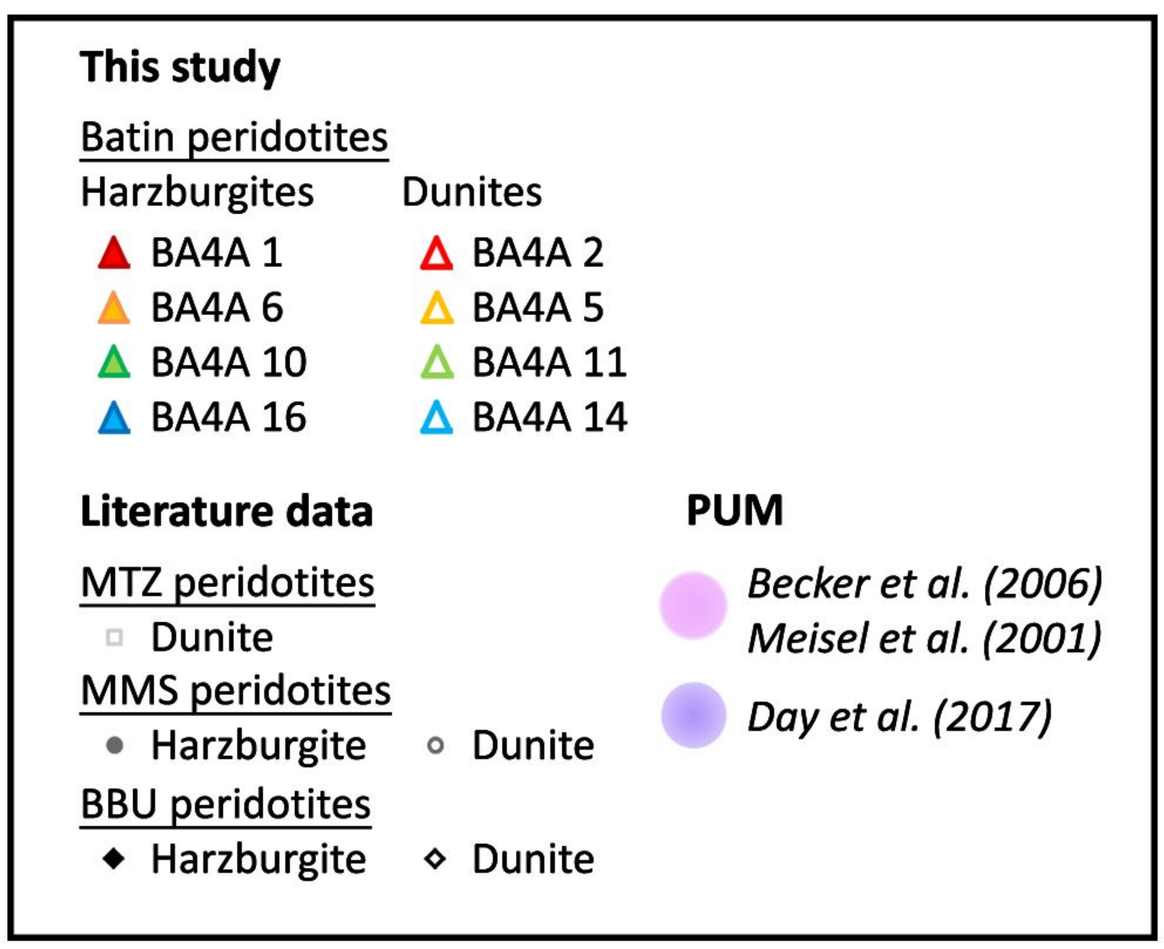
This study
Batin peridotites
Harzburgites
BA4A 1
BA4A 6
BA4A 10
BA4A 16
Dunites
BA4A 2
BA4A 5
BA4A 11
BA4A 14
Literature data
MTZ peridotites
Dunite
MMS peridotites
Harzburgite
Dunite
BBU peridotites
Harzburgite
Dunite
PUM
Becker et al. (2006)
Meisel et al. (2001)
Day et al. (2017)

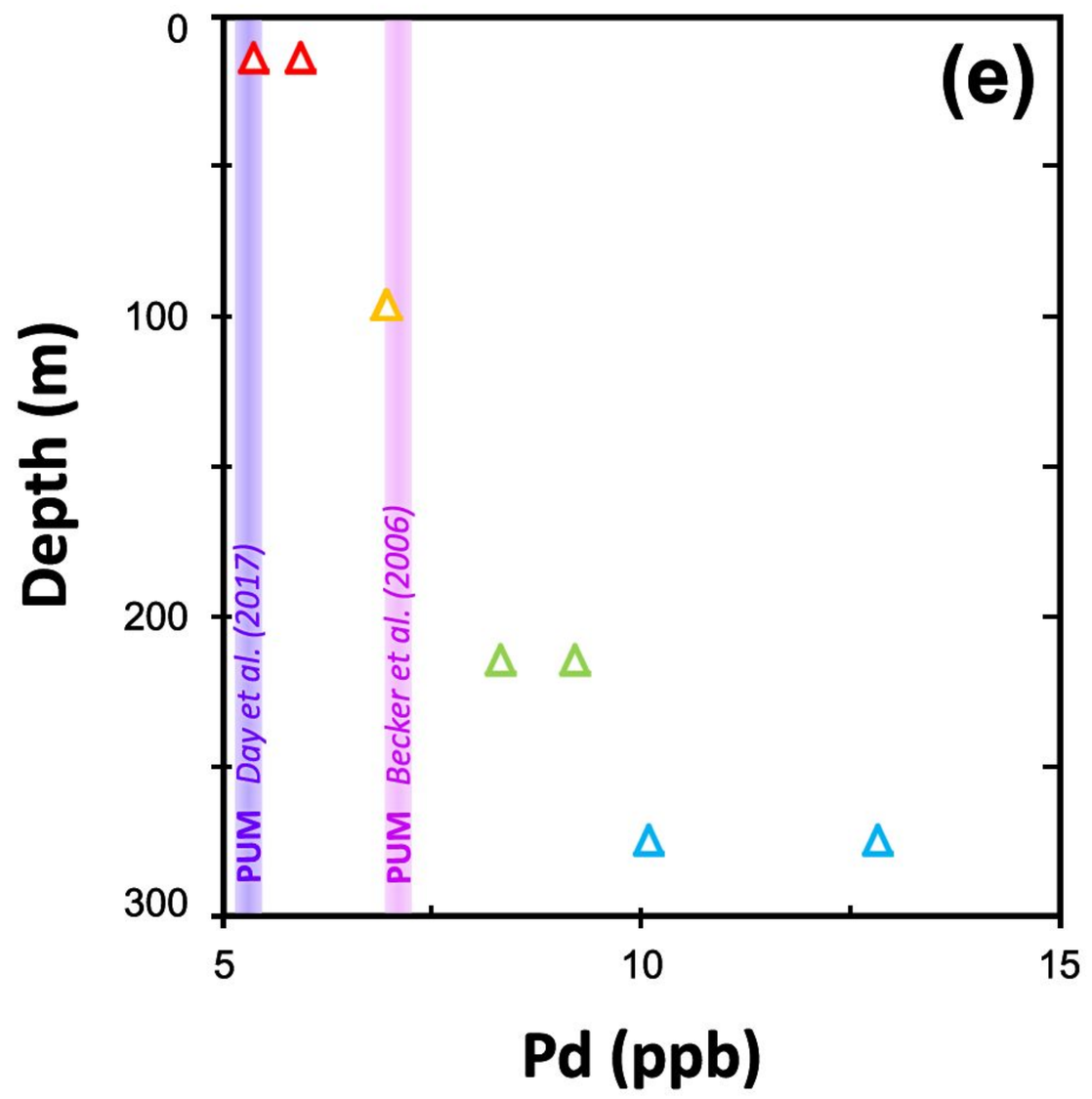
(e)
Depth (m)
0
100
200
300
PUM Day et al. (2017)
PUM Becker et al. (2006)
5
10
15
Pd (ppb)

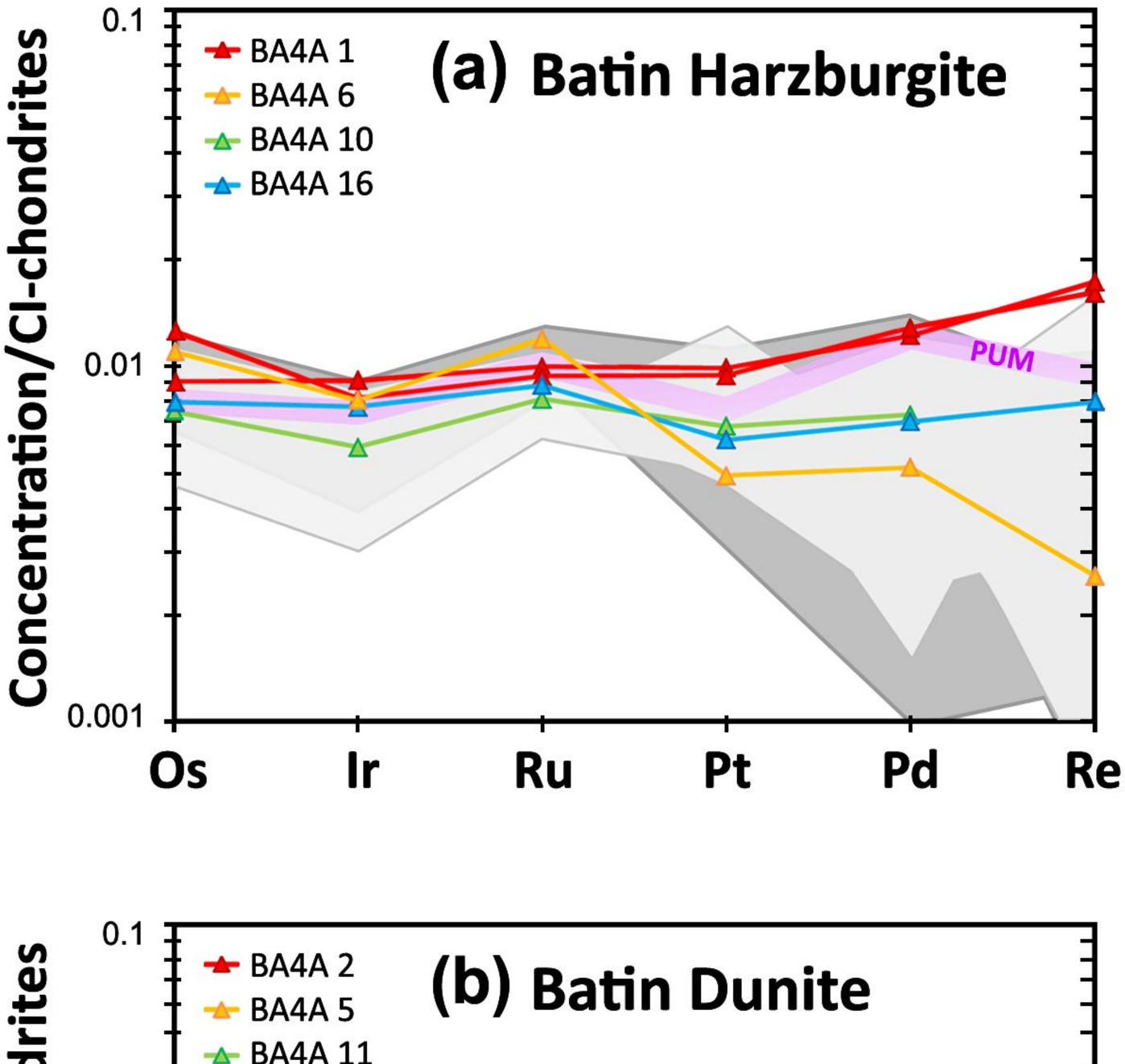
(a) Batin Harzburgite
BA4A 1
BA4A 6
BA4A 10
BA4A 16
PUM
Concentration/CI-chondrites
0.1
0.01
0.001
Os
Ir
Ru
Pt
Pd
Re

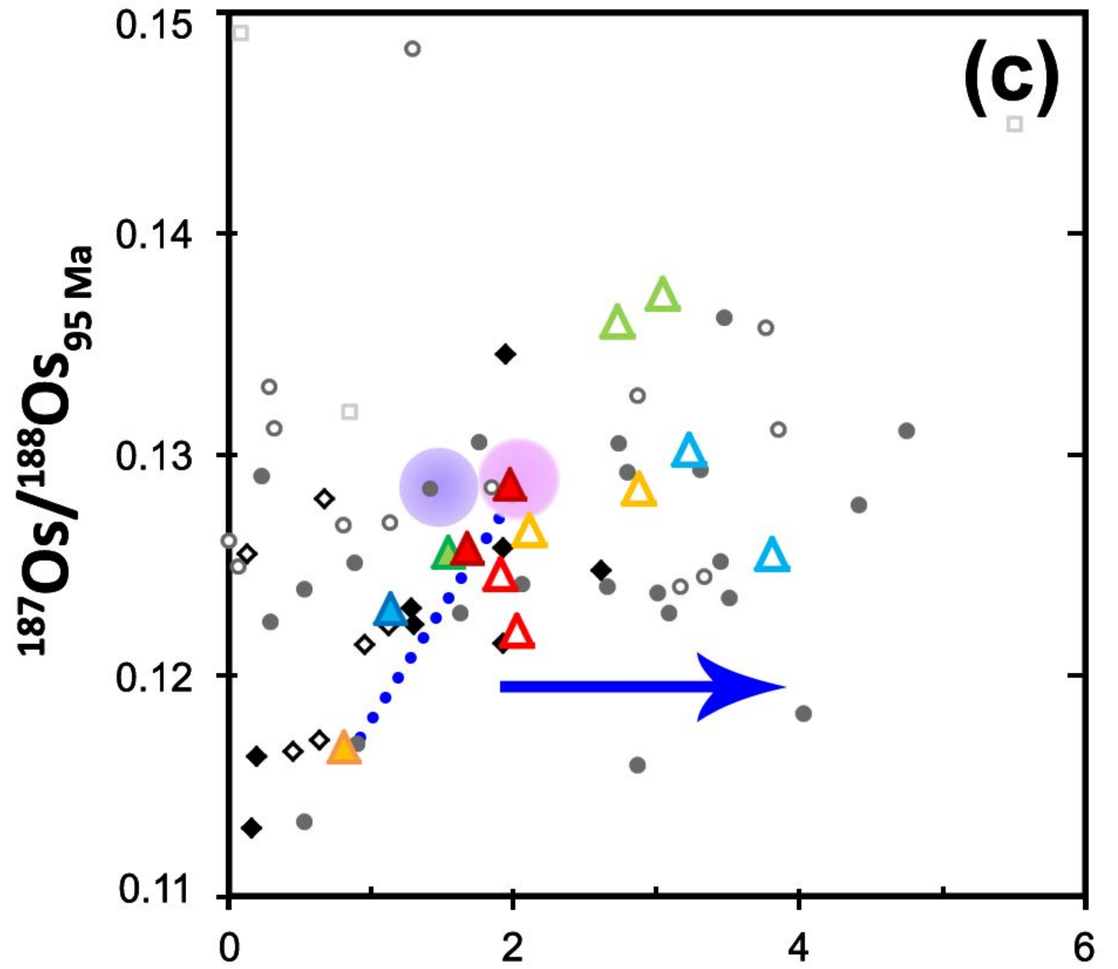
(c)
$^{187}Os/^{188}Os_{95\ Ma}$
0.15
0.14
0.13
0.12
0.11
0
2
4
6
Pd/Ir

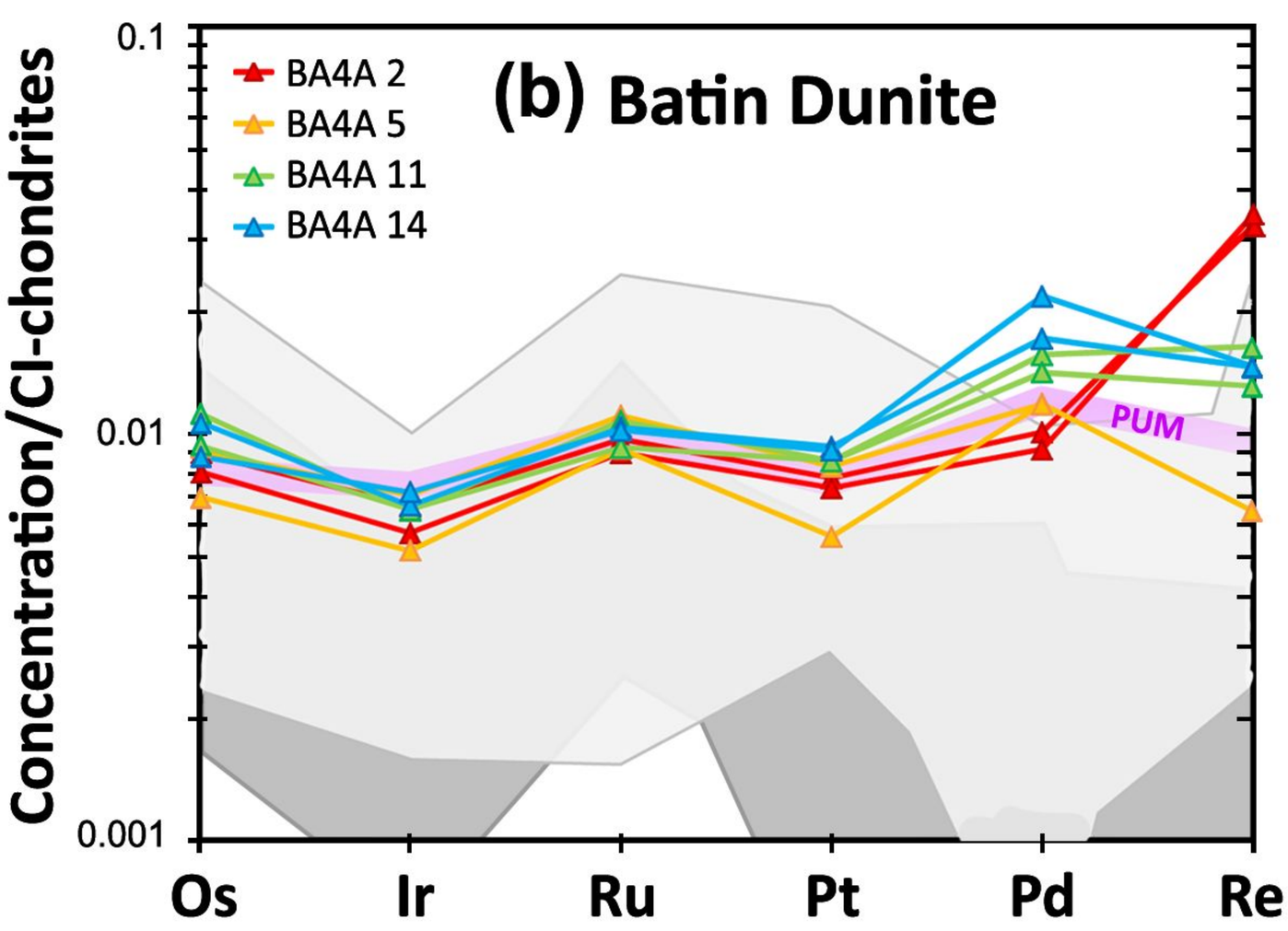
(b) Batin Dunite
BA4A 2
BA4A 5
BA4A 11
BA4A 14
PUM
Concentration/CI-chondrites
0.1
0.01
0.001
Os
Ir
Ru
Pt
Pd
Re

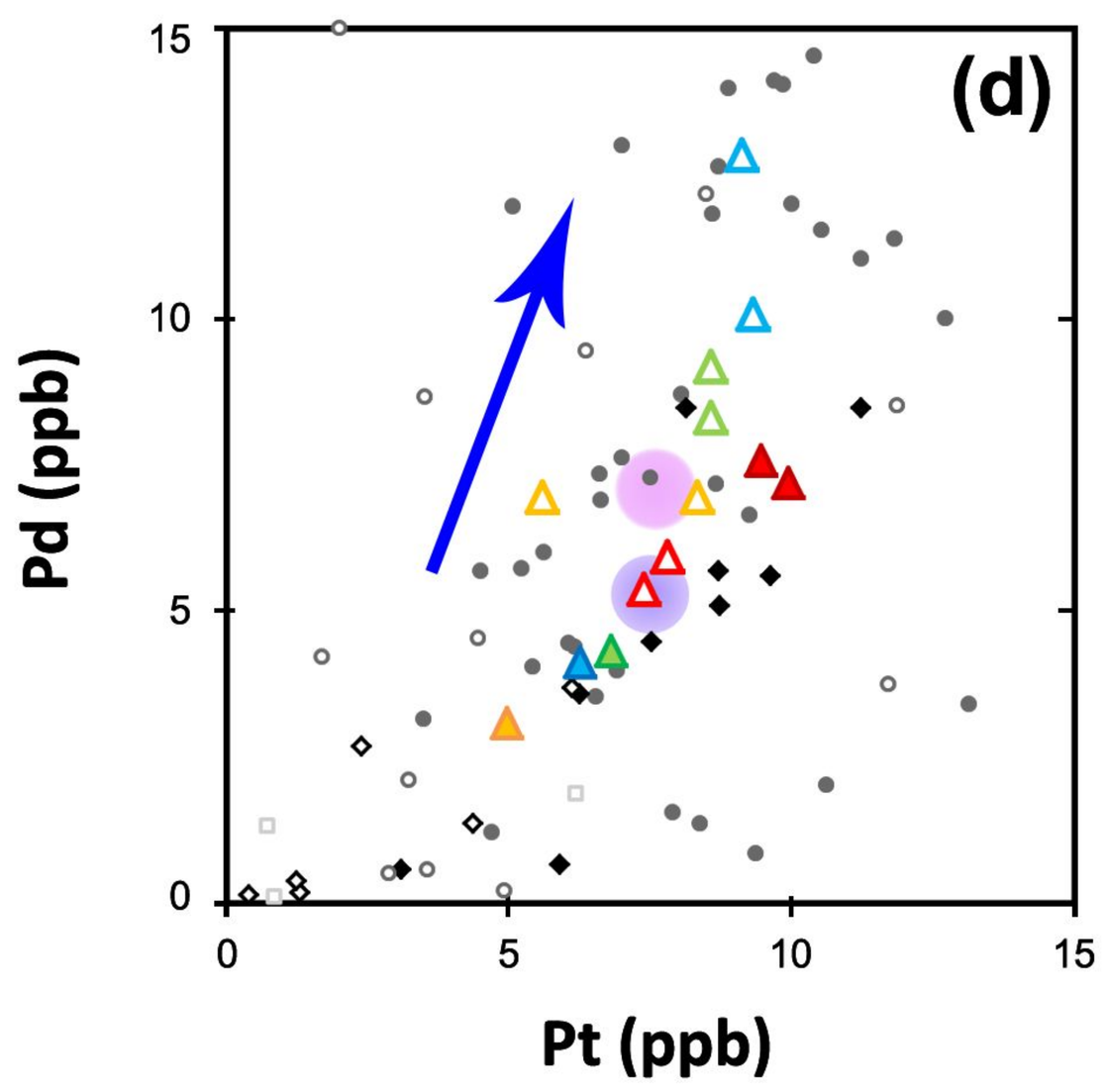
(d)
Pd (ppb)
15
10
5
0
0
5
10
15
Pt (ppb)

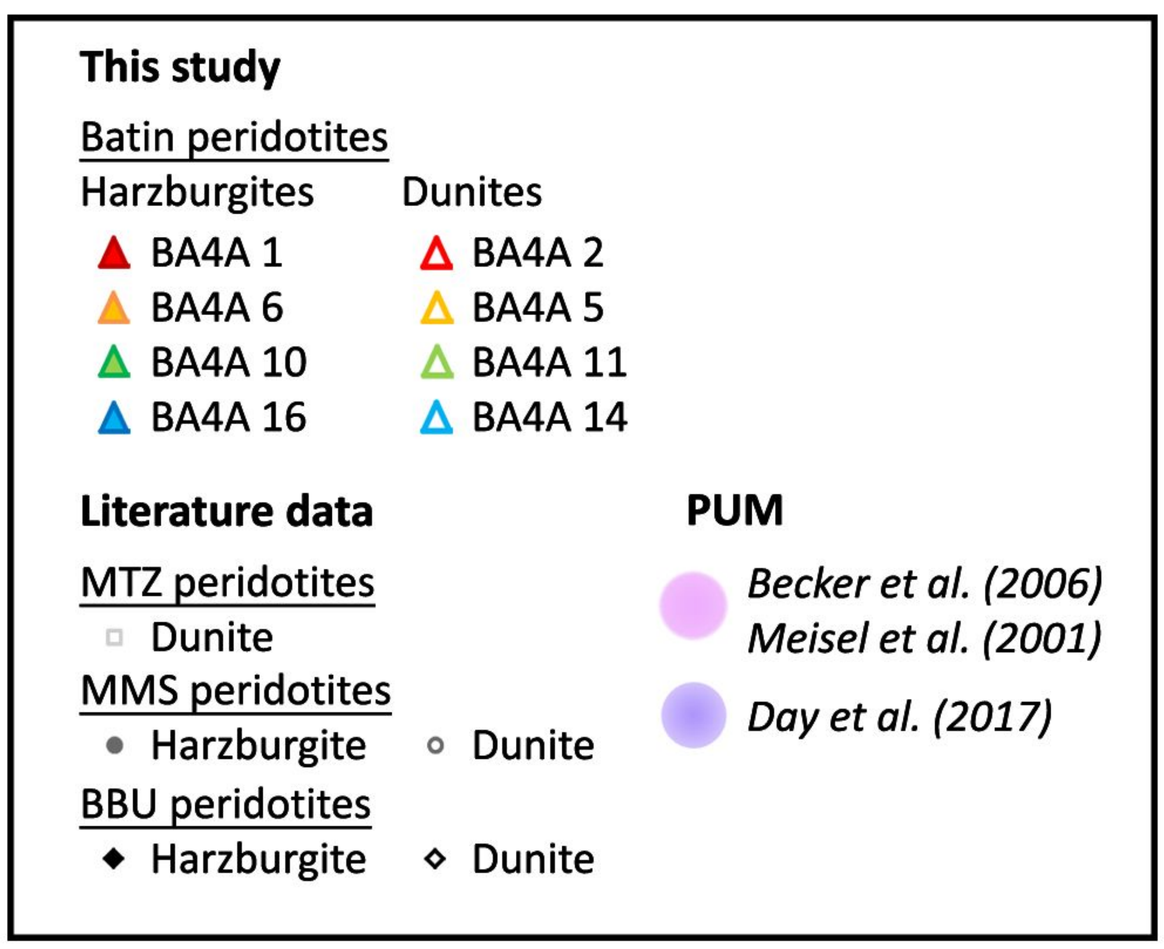
This study
Batin peridotites
Harzburgites
BA4A 1
BA4A 6
BA4A 10
BA4A 16
Dunites
BA4A 2
BA4A 5
BA4A 11
BA4A 14
Literature data
MTZ peridotites
Dunite
MMS peridotites
Harzburgite
Dunite
BBU peridotites
Harzburgite
Dunite
PUM
Becker et al. (2006)
Meisel et al. (2001)
Day et al. (2017)

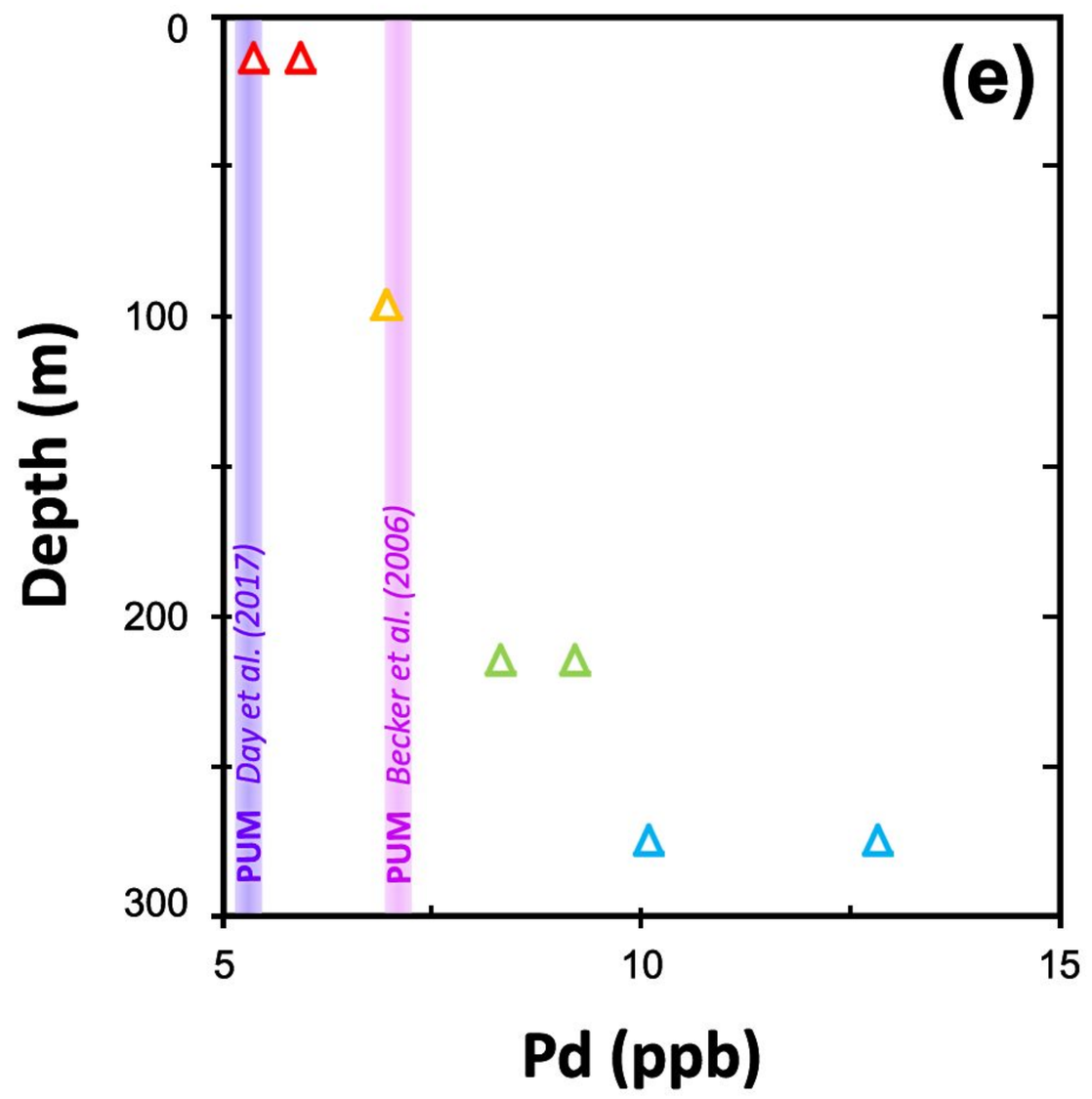
(e)
Depth (m)
0
100
200
300
PUM Day et al. (2017)
PUM Becker et al. (2006)
5
10
15
Pd (ppb)

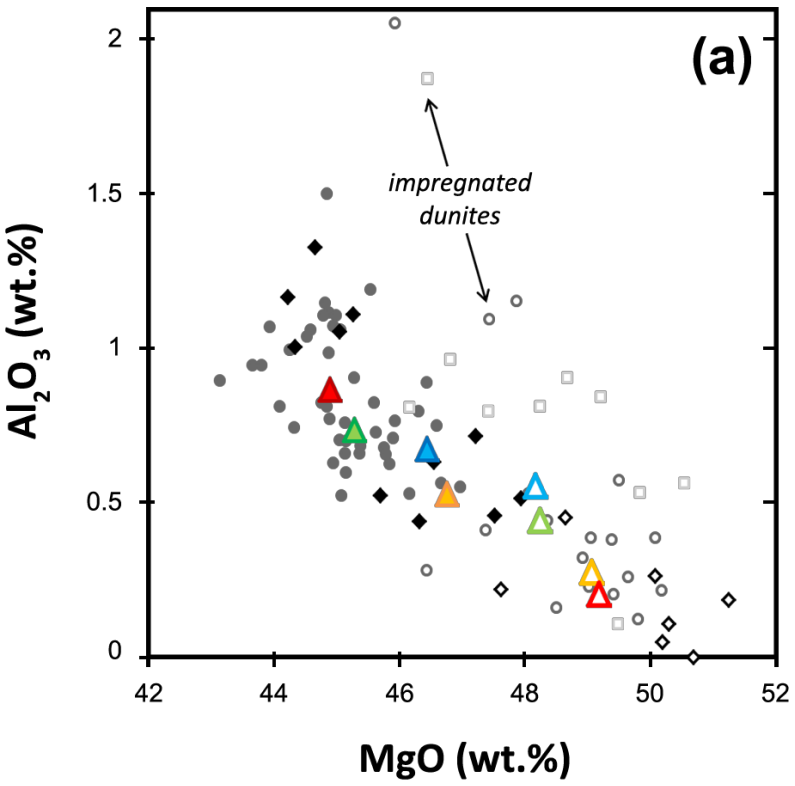

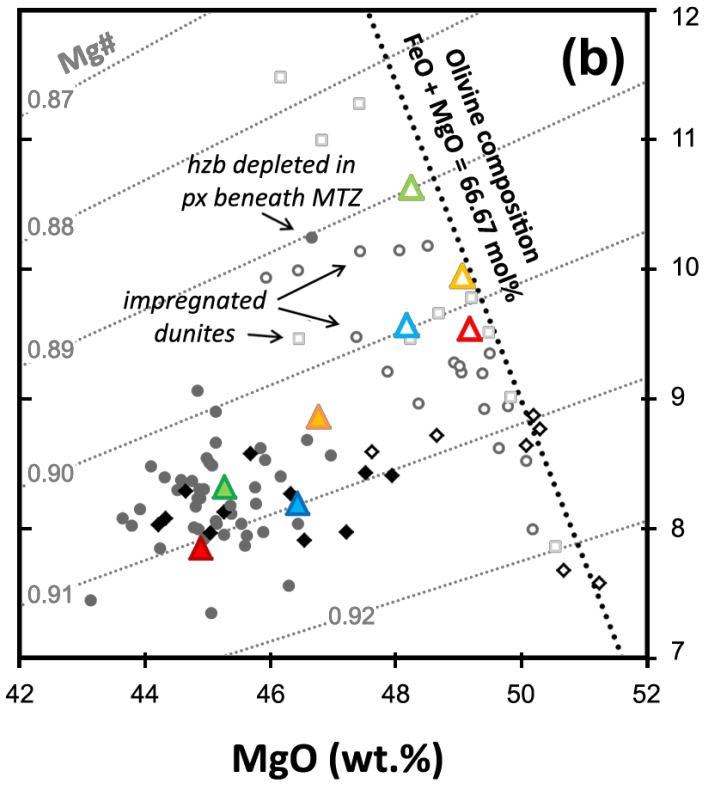

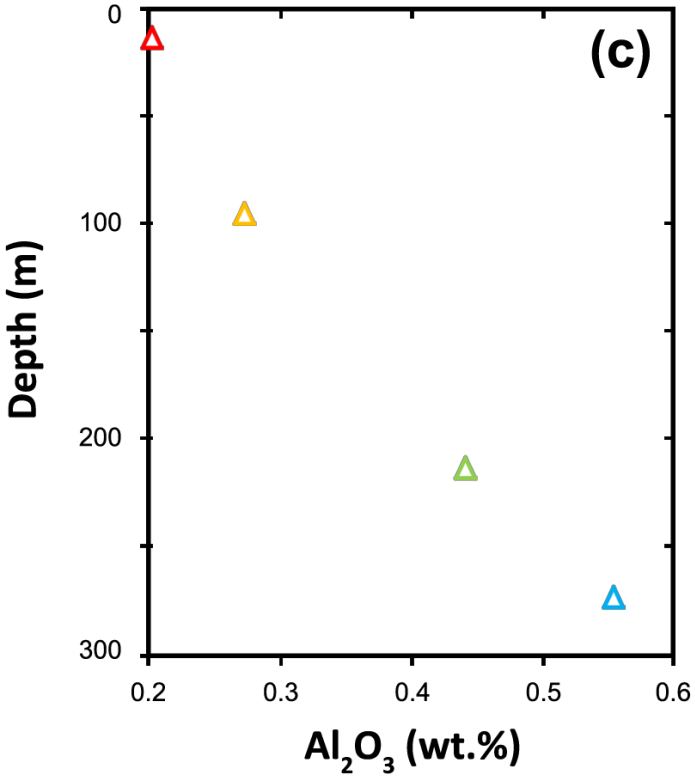

This study

Batin peridotites

Harzburgites	Dunites
BA4A 1	BA4A 2
BA4A 6	BA4A 5
BA4A 10	BA4A 11
BA4A 16	BA4A 14

Literature data

Moho transition zone (MTZ) peridotites
- Dunite

Main mantle section (MMS) peridotites
- Harzburgite
- Dunite

Basal banded unit (BBU) peridotites
- Harzburgite
- Dunite

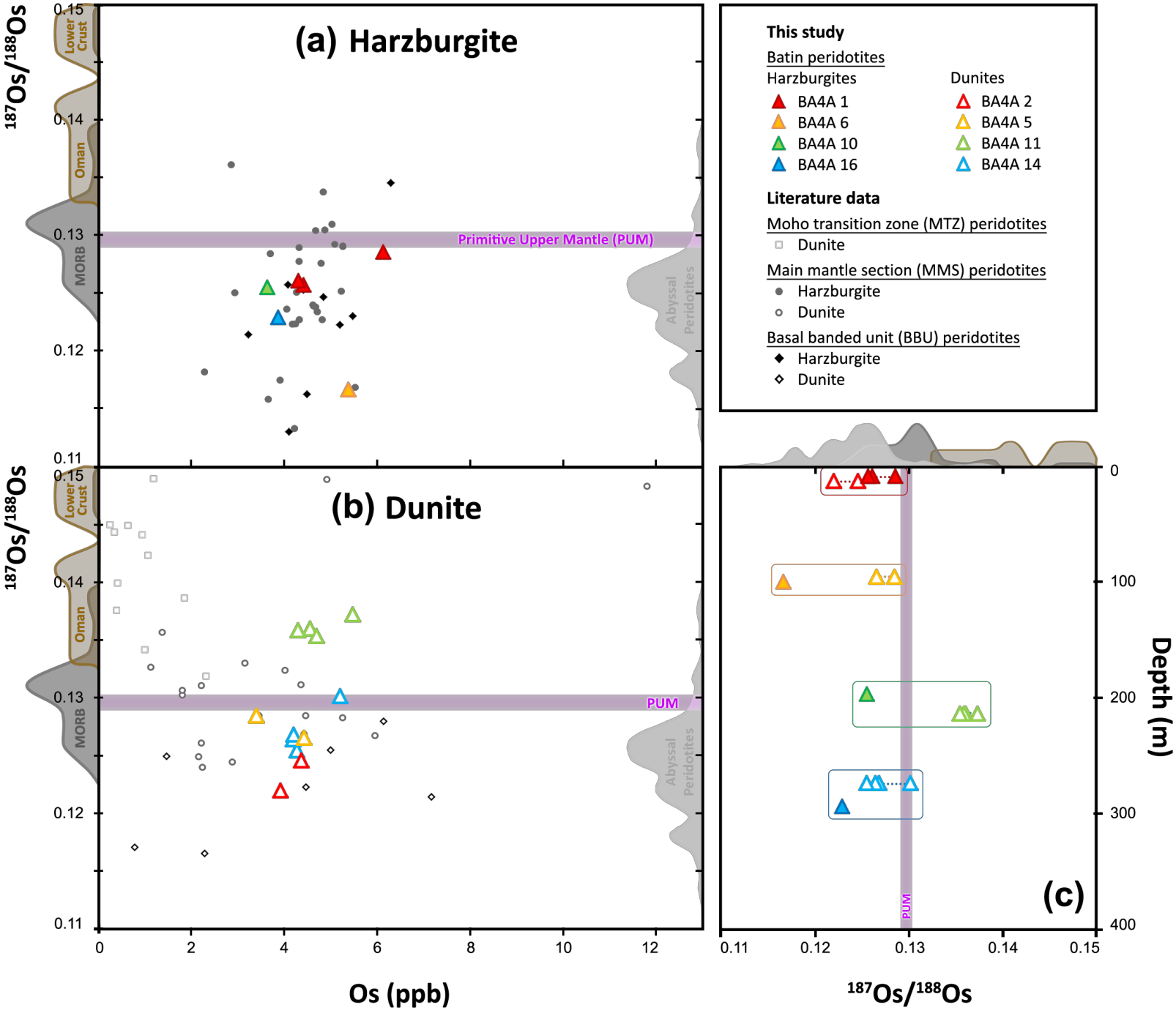
(a) Harzburgite
(b) Dunite
(c)
Primitive Upper Mantle (PUM)
PUM
Lower Crust
Oman
MORB
Abyssal Peridotites
$^{187}Os/^{188}Os$
Os (ppb)
Depth (m)
This study
Batin peridotites
Harzburgites
BA4A 1
BA4A 6
BA4A 10
BA4A 16
Dunites
BA4A 2
BA4A 5
BA4A 11
BA4A 14
Literature data
Moho transition zone (MTZ) peridotites
Dunite
Main mantle section (MMS) peridotites
Harzburgite
Dunite
Basal banded unit (BBU) peridotites
Harzburgite
Dunite

Table 1. Whole-rock major element compositions of the studied Batin peridotites

Sample	Lithology	Oman DP reference	Depth	Hzb/Dun pair distance	SiO_2	Al_2O_3	FeO*	MnO	MgO	CaO	Na_2O	LOI	Total	Mg#
			(m)	(m)	(wt.%)									
BA4A 01	hzb	5-2 (46-51)	10.16	3.175	39.09	0.74	6.76	0.11	38.65	0.73	b.d.l.	12.41	98.49	0.911
BA4A 02	dunite	6-3 (8-13)	13.33		33.12	0.17	7.73	0.12	39.85	0.04	b.d.l.	17.51	98.53	0.902
BA4A 06	hzb	39-2 (74-79)	100.24	4.620	36.71	0.45	7.53	0.12	39.75	0.44	b.d.l.	14.01	98.99	0.904
BA4A 05	dunite	37-4 (35-40)	95.62		33.06	0.23	8.17	0.13	40.29	0.25	b.d.l.	16.23	98.35	0.898
BA4A 10	hzb	73-4 (4-9)	197.20	16.965	37.88	0.63	7.09	0.11	38.58	0.92	b.d.l.	13.87	99.07	0.907
BA4A 11	dunite	80-3 (12-17)	214.17		33.31	0.37	8.84	0.14	40.08	0.32	0.04	15.38	98.47	0.890
BA4A 16	hzb	107-1 (25-30)	293.98	19.770	37.48	0.58	7.02	0.11	39.80	0.71	b.d.l.	13.42	99.11	0.910
BA4A 14	dunite	100-3 (18-23)	274.20		34.08	0.46	7.92	0.13	39.86	0.31	b.d.l.	15.43	98.18	0.900

Whole-rock major element compositions were analyzed by the SARM (Service d'Analyse des Roches et des Minéraux) at the CRPG laboratory in Nancy (France) using ICP-OES iCap6500. K_2O, TiO_2 and P_2O_5 contents are below detection limit of the instrument. Oman DP references include section unit and sample interval (cm).

**Total Fe as FeO.*

Mg# = $Mg/(Mg+Fe)_{at}$; LOI = Loss On Ignition; b.d.l. = below detection limit; Hzb = harzburgite; Dun = dunite.

Table 2. HSE concentrations and Os isotope compositions of the studied Batin peridotites and UB-N and MUH-1 standards

Sample	Lithology	Depth (m)	[Os] (ppb)	[Ir] (ppb)	[Ru] (ppb)	[Pt] (ppb)	[Pd] (ppb)	[Re] (ppb)	$^{187}Re/^{188}Os$	$(^{187}Os/^{188}Os)_m$	2σ error	$(^{187}Os/^{188}Os)_{95Ma}$	2σ error
BA4A 1	hzb	10.155	4.41	4.30	6.93	9.96	7.19	0.641	0.701	0.12682	0.00057	0.12571	0.00057
BA4A 1-d_1			6.12	3.83	6.51	9.49	7.57	0.599	0.471	0.12936	0.00145	0.12861	0.00145
BA4A 1-d_2			4.30					0.564	0.633	0.12710	0.00054	0.12610	0.00054
BA4A 2	dunite	13.330	4.35	3.12	6.69	7.81	5.93	1.203	1.331	0.12669	0.00055	0.12459	0.00055
BA4A 2-d			3.92	2.67	6.20	7.38	5.38	1.277	1.572	0.12450	0.00059	0.12201	0.00060
BA4A 6	hzb	100.245	5.38	3.79	8.28	4.97	3.07	0.096	0.086	0.11684	0.00052	0.11671	0.00052
BA4A 5	dunite	95.625	4.42	3.31	7.67	8.34	6.96	0.239	0.260	0.12696	0.00053	0.12655	0.00054
BA4A 5-d			3.398	2.42	6.35	5.60	6.95			0.12762	0.00062	0.12846	0.00063
BA4A 10	hzb	197.205	3.63	2.80	5.62	6.83	4.31			0.12548	0.00053	0.12552	0.00054
BA4A 11	dunite	214.170	5.46	3.04	7.44	8.59	9.20	0.606	0.535	0.13812	0.00124	0.13728	0.00124
BA4A 11-d_1			4.55	3.06	6.39	8.59	8.32	0.485	0.514	0.13682	0.00054	0.13601	0.00055
BA4A 11-d_2			4.69					0.631	0.649	0.13641	0.00053	0.13538	0.00053
BA4A 11-d_3			4.29					0.496	0.559	0.13675	0.00051	0.13586	0.00051
BA4A 16	hzb	293.975	3.86	3.63	6.14	6.27	4.13	0.295	0.368	0.12354	0.00054	0.12296	0.00054
BA4A 14	dunite	274.205	5.19	3.13	7.17	9.32	10.09	0.539	0.501	0.13097	0.00061	0.13018	0.00061
BA4A 14-d_1			4.27	3.37	7.06	9.13	12.82	0.542	0.612	0.12644	0.00055	0.12547	0.00055
BA4A 14-d_2			4.18					0.507	0.584	0.12736	0.00051	0.12644	0.00051
BA4A 14-d_3			4.20					0.483	0.554	0.12769	0.00053	0.12681	0.00053
Standards													
MUH-1			4.10	2.61	5.65	20.99	8.93	0.276	0.325	0.12658	0.00052		
UB-N 1			3.44	2.76	5.88	6.75	10.44	0.243	0.341	0.12725	0.00055		
UB-N 2			3.30					0.240	0.351	0.12780	0.00052		
UB-N 3			3.43					0.191	0.269	0.12690	0.00051		

HSE concentrations and Os isotopic compositions in whole rock powders were analyzed at the CRPG laboratory in Nancy (France) using MC-ICP-MS (Neptune +) and N-TIMS (Finnigan MAT 262) (Os). All uncertainties are 2SE and include all recognized sources of uncertainty, including in-run analytical precision, reproducibility of standard analyses, uncertainties related to blank variability, uncertainties related to age correction (95 Ma). Duplicate analyses were performed for several samples (noted "-d") and the UB-N standard. Details are presented in the Supplementary Tables 1-3. Hzb = harzburgite.

Supplementary material

1. Analytical methods

1.1. Major element compositions

Whole-rock major element concentrations (Table 1) were measured by the SARM at the CRPG laboratory (Nancy, France;http://helium.crpg.cnrs-nancy.fr/SARM/). Loss on Ignition (LOI) was determined by mass loss after calcination at 1000°C. The anhydrous residue was fused with $LiBO_2$ flux then digested in acid prior to major element analysis using Inductively Coupled Plasma Optical Emission Spectrometry (ICP-OES iCap6500). Detailed technique description can be found in Carignan et al. (2001). Uncertainties vary from <2% for SiO_2 to <20% for MnO, based on the concentrations.

1.2. Highly siderophile element abundances and Os isotopic compositions

Highly siderophile element abundances and Os isotopic compositions were analyzed at CRPG. Sample powders (1.5-2g) were spiked with a mixed tracer solution containing ^{190}Os, ^{101}Ru, ^{191}Ir, ^{196}Pt, ^{105}Pd and ^{185}Re, and digested in a solution of concentrated $HCl:HNO_3$ (2:5 for samples and 1.5:5 for blanks) in a High Pressure Asher (HPA-S; Anton Paar) for 16 hours at 100 bars and 285°C. This procedure brings all of the Os to its most oxidized form (OsO_4), assuring spike-sample equilibration. Osmium was chemically extracted from the sample solution into liquid bromine, for which OsO_4 has a strong affinity, and purified by microdistillation, using techniques adapted from Birck et al. (1997). Following Os extraction, other HSE were separated from the residual acidic solution by anion-exchange column chromatography using the method of Rehkämper & Halliday (1997). For several of the replicate analyses, only $^{187}Os/^{188}Os$ ratios and Os and Re concentrations were determined. In these cases, Re was separated using AG1 X8 resin columns from the residual solution.

Rhenium, Pd, Ru, Pt and Ir isotopic compositions used for concentration determinations by isotope dilution were analyzed by MC-ICP-MS (ThermoScientific Neptune +). Given that Rh and Au are monoisotopic elements, it was not possible to analyze them by this method. Instrumental mass

fractionation was corrected by standard bracketing, assuming $^{187}Re/^{185}Re$ = 1.6738, $^{108}Pd/^{106}Pd$ = 0.9236, $^{102}Ru/^{99}Ru$ = 2.4726, $^{194}Pt/^{195}Pt$ = 0.9744 and $^{191}Ir/^{193}Ir$ = 0.5949 for the standard. Osmium isotopic compositions were determined by Negative Thermal Ionization Mass Spectrometry (NTIMS) (Creaser et al., 1991; Völkening et al., 1991) using a Finnigan MAT 262 mass spectrometer. Isotopic ratios of OsO_3^- masses were obtained by peak jumping on an ETP electron multiplier. Corrections for heavy oxides, spike contributions and instrumental mass fractionation were made off-line, assuming a natural $^{192}Os/^{188}Os$ ratio of 3.08271.

Highly siderophile element abundances and Os isotope data are presented in Table 2 and Supplementary Tables 1-2. All uncertainties are 2SE and include all significant recognized sources of uncertainty (in-run analytical precision, standard reproducibility, uncertainties related to variability of the amount and isotopic composition of the analytical blank, uncertainties related to the Re/Os ratio and the ensuing age correction). These different uncertainty components are listed for each sample in Supplementary Table 3. The total analytical blanks varied between the two main analytical periods of the study: Os = 0.0007 ± 0.0002 ng, $^{187}Os/^{188}Os$ = 0.209 ± 0.122 (n = 3), Re = 0.042 ± 0.078 ng, Ir = 0.001 ± 0.002 ng, Pt = 0.015 ± 0.023 ng, Ru = 0.018 ± 0.045 ng, Pd = 0.014 ± 0.022 ng (n = 4) (first period, including all full HSE analyses); Os = 0.0010 ± 0.0000 ng (n = 2), $^{187}Os/^{188}Os$ = 0.2204 ± 0.0058 (n = 1), Re = 0.022 ± 0.003 ng (n = 2) (second period; comprising those replicates analyzed solely for $^{187}Os/^{188}Os$ and Re and Os concentrations); all uncertainties 2σ. The total 2σ uncertainties, including the blank variability, on the initial $^{187}Os/^{188}Os$ ratios of all samples are < 1.2%. UB-N and MUH-1 reference materials (Table 2 and Supplementary Tables 1-3), which like our samples are serpentinized peridotites, were analyzed concurrently with the samples, yielding mean $^{187}Os/^{188}Os$ ratios of 0.1273 ± 0.0005 (2σ) (n = 3) and 0.1266 ± 0.0005 (2σ) (n = 1) respectively, in agreement with the accepted values (MUH-1: Snortum & Day (2020); UB-N : Meisel et al. (2003)). Duplicate analyses were performed for all dunites (n = 2 for BA4A 2,5 and 4 for BA4A 11,14) and harzburgite BA4A 1 (n = 3).

2. Seawater alteration of peridotite - mixing model

To exclude a contamination of our samples with seawater, we simulate a simple two component mixture between seawater and a common peridotite in Klaessens et al. (in revision) (Supplementary Fig. 1), similar to the model used by Sanfilippo et al. (2016), using the following equations:

(1) $$[Os]_{mix} = (f \cdot [Os]_{seawater}) + \left((1-f) \cdot [Os]_{per}\right)$$

(2) $$(^{187}Os/^{188}Os)_{mix} = \frac{1}{[Os]_{mix}} \cdot (f \cdot [Os]_{seawater} \cdot (^{187}Os/^{188}Os)_{seawater}) + \left((1-f) \cdot [Os]_{per} \cdot (^{187}Os/^{188}Os)_{per}\right)$$

Th and U concentrations are calculated in the same manner as Os concentration, using Equation A.1.

where: $[Os]_{per}$: *concentration in Os of the peridotite*

$[Os]_{seawater}$: *seawater concentration in Os*

$[Os]_{mix}$: *concentration in Os of the mixture, including seawater and peridotite*

$(^{187}Os/^{188}Os)_{per}$: $^{187}Os/^{188}Os$ *ratio of the peridotite*

$(^{187}Os/^{188}Os)_{melt}$: $^{187}Os/^{188}Os$ *seawater ratio*

$(^{187}Os/^{188}Os)_{mix}$: $^{187}Os/^{188}Os$ *ratio of the mixture, including seawater and peridotite*

f: *seawater fraction*

We use the following compositions for the peridotite and Cretaceous seawater endmembers:

$(^{187}Os/^{188}Os)_{per}$ = 0.124	$(^{187}Os/^{188}Os)_{seawater}$ = 0.55
$[Os]_{per}$ = 4 ppb	$[Os]_{seawater}$ = 10^{-5} ppb
$[Th]_{per}$ = 13 ppb	$[Th]_{seawater}$ = 5 x 10^{-6} ppb
$[U]_{per}$ = 4.5 ppb	$[U]_{seawater}$ = 3.3 ppb

For the peridotite, the $^{187}Os/^{188}Os$ ratio chosen is typical of Oman harzburgites, as well as of abyssal peridotites, and its Os concentration of 4 ppb is typical of dunites and harzburgites from the Batin area (Table 1, main text). The peridotite Th and U concentrations are those of the depleted peridotite reference material PCC-1 (Govindaraju, 1994). Seawater Os, Th and U contents are the same as those used in the model of Sanfilippo et al. (2016). The seawater $^{187}Os/^{188}Os$ ratio is from Ravizza et al. (1999).

This mixing model shows that seawater contamination sufficient to produce radiogenic Os compositions similar to that of the most radiogenic Batin sample, dunite BA4A 11 ($^{187}Os/^{188}Os_{95Ma}$ ~ 0.136), would require water/rock ratios >10000, and would lower corresponding peridotite Th/U ratios to ~0.0003. In another study of the ICDP Oman Drilling Project BA borehole samples, Th/U ratios of dunites from the same hole used in our study (BA4A; some collected in close proximity with our samples) and of harzburgites from the BA3A and BA1B holes were analyzed (Aupart et al., in revision). These Th/U ratios (0.1-3.8) are all several orders of magnitude higher than 0.0003, implying that seawater contamination was much less important than that required to explain our results by this process. The dunite sample BA4A 80-4 (44-49) of Aupart et al. (in revision) was collected just next to our radiogenic dunite BA4A 11 and has an almost unperturbed Th/U ratio of 2.16. Supplementary Fig. 1 shows the Os composition and Th/U ratio range of Batin peridotites in comparison with the mixing model curve and other published Oman peridotite data (Godard et al., 2000; Hanghøj et al., 2010; Klaessens et al., 2021; Xiong et al., 2020a, 2020b). These data, in addition to the absence of correlation between LOI values and Os isotope composition in our Batin peridotite samples, argue that they have preserved the Os isotope signatures of essentially magmatic processes.

Figures

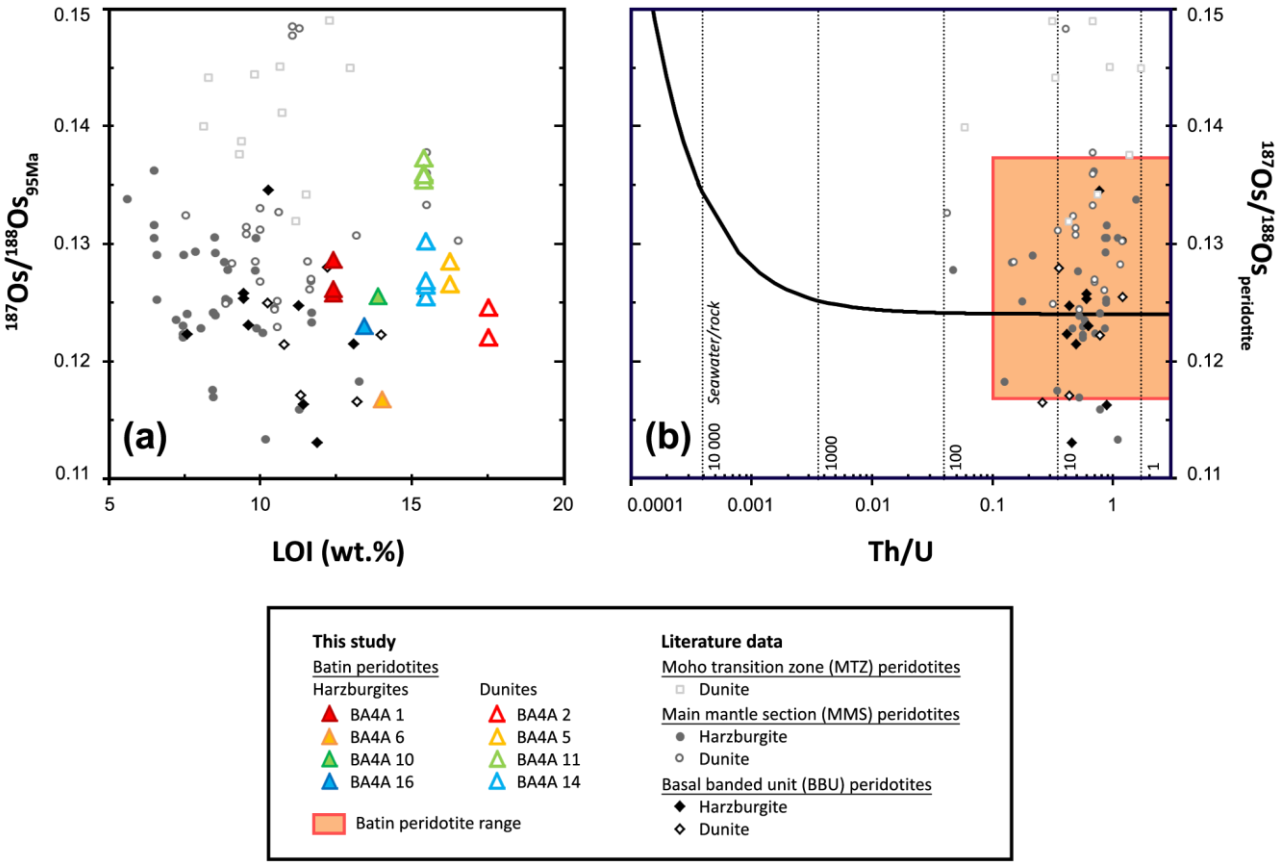

Supplementary Fig. 1. Initial osmium isotope composition vs. tracers of seawater contamination (**a**, LOI and **b**, Th/U ratio) for Batin harzburgites and dunites. $^{187}Os/^{188}Os_{95Ma}$ vs. **(a)** LOI, **(b)** Th/U ratio. In panel **(b)**, the black curve represents the compositions of a mixture of Os, Th and U from seawater ($^{187}Os/^{188}Os$ = 0.55; [Os] = 10^{-5} ppb; [Th] = 5 x 10^{-6} ppb; [U] = 3.3 ppb) and peridotite ($^{187}Os/^{188}Os$ = 0.124; [Os] = 4 ppb; [Th] = 13 ppb; [U] = 4.5 ppb). Black dotted lines indicate seawater/rock ratios of 1, 10, 100, 1000 and 10 000. The orange area represent Os compositions (this study) and Th/U ratio (Aupart et al., in revision) range of Batin peridotites. In all panels, published Oman peridotite data are shown for comparison (Godard et al., 2000; Hanghøj et al., 2010; Klaessens et al., 2021; Xiong et al., 2020a, 2020b): dunites from Moho transition zone (MTZ), dunites and harzburgites from main (MMS) and basal mantle sections (BBU). Attribution of samples reported in the literature to the three domains defined in Klaessens et al. (2021) was based on their geographic positions in the mantle

section. No correlation is observed between initial Os isotope ratios, LOI, whole-rock Th/U ratios and the Th/U model curve. This curve shows that seawater/rock ratios >10 000 would be required to produce $^{187}Os/^{188}Os$ ratios comparable to those of the MTZ dunites and Batin dunite BA4A 11, and these would be associated with Th/U ratios much lower than the observed values. Thus, seawater contamination cannot explain the radiogenic initial $^{187}Os/^{188}Os$ ratios of these samples.

Tables

Supplementary Table 1. Re and Os concentrations and Os isotope compositions of the studied Batin peridotites and UB-N and MUH-1 standards

Supplementary Table 2. HSE concentrations of the studied Batin peridotites and UB-N and MUH-1 standards

Supplementary Table 3. Different components of the uncertainties on HSE concentrations and Os isotope compositions entering into the total uncertainties

Supplementary Table 4. Re and Os concentrations and Os isotope compositions of Oman harzburgites and the three types of dunites and of the reference materials (Klaessens, 2021; Klaessens et al., 2021)

Supplementary Table 5. HSE concentrations of Oman harzburgites and the three types of dunites and of the reference materials (Klaessens, 2021; Klaessens et al., 2021)

References

Aupart, C., Morales, L., Godard, M., Jamtveit, B., & the Oman DP Science Team. (in revision). Microstructures and mass-transfer associated with early faults in peridotites from the Samail Ophiolite, Oman. Under review at EPSL. *Earth and Planetary Science Letters*.

Birck, J. L., Roy Barman, M., & Capmas, F. (1997). Re-Os Isotopic Measurements at the Femtomole Level in Natural Samples. *Geostandards Newsletter*, *21*(1), 19–27. https://doi.org/10.1111/j.1751-908X.1997.tb00528.x

Carignan, J., Hild, P., Mevelle, G., Morel, J., & Yeghicheyan, D. (2001). Routine analyses of trace elements in geological samples using flow injection and low pressure on-line liquid chromatography coupled to ICP-MS: A study of geochemical reference materials BR, DR-N, UB-N, AN-G and GH. *Geostandards Newsletter*, *25*(2–3), 187–198. https://doi.org/10.1111/j.1751-908x.2001.tb00595.x

Creaser, R. A., Papanastassiou, D. A., & Wasserburg, G. J. (1991). Negative thermal ion mass spectrometry of osmium, rhenium and iridium. *Geochimica et Cosmochimica Acta*, *55*(1), 397–401. https://doi.org/10.1016/0016-7037(91)90427-7

Godard, M., Jousselin, D., & Bodinier, J. L. (2000). Relationships between geochemistry and structure beneath a palaeo-spreading centre: A study of the mantle section in the Oman ophiolite. *Earth and Planetary Science Letters*, *180*(1–2), 133–148. https://doi.org/10.1016/S0012-821X(00)00149-7

Govindaraju, K. (1994). Compilation of working values and sample description for 383 geostandards Special issue. *Geostandards Newsletter*, *18*(July), 1–158. https://doi.org/10.1046/j.1365-2494.1998.53202081.x-i1

Hanghøj, K., Kelemen, P. B., Hassler, D., & Godard, M. (2010). Composition and genesis of depleted mantle peridotites from the Wadi Tayin massif, Oman ophiolite; Major and trace element geochemistry, and Os isotope and PGE systematics. *Journal of Petrology*, *51*(1–2), 201–227. https://doi.org/10.1093/petrology/egp077

Klaessens, D. (2021). *Migration des liquides de fusion et formation des dunites dans le manteau de l'ophiolite d'Oman*. Université de Lorraine.

Klaessens, D., Reisberg, L., Jousselin, D., Godard, M., & Aupart, C. (2021). Osmium isotope evidence for rapid melt migration towards the Moho in the Oman ophiolite. *Earth and Planetary Science Letters*, *572*, 117111. https://doi.org/10.1016/j.epsl.2021.117111

Meisel, T., Reisberg, L., Moser, J., Carignan, J., Melcher, F., & Brügmann, G. E. (2003). Re-Os systematics of UB-N, a serpentinized peridotite reference material. *Chemical Geology*, *201*(1–2), 161–179. https://doi.org/10.1016/S0009-2541(03)00234-1

Ravizza, G., Sherrell, R. M., Field, M. P., & Pickett, E. A. (1999). Geochemistry of the Margi umbers, Cyprus, and the Os isotope composition of Cretaceous seawater. *Geology*, *27*(11), 971–974. https://doi.org/10.1130/0091-7613(1999)027<0971:GOTMUC>2.3.CO;2

Rehkämper, M., & Halliday, A. N. (1997). Development and application of new ion-exchange techniques for the separation of the platinum group and other siderophile elements from geological samples. *Talanta*, *44*(4), 663–672. https://doi.org/10.1016/S0039-9140(96)02100-5

Sanfilippo, A., Morishita, T., & Senda, R. (2016). Rhenium-osmium isotope fractionation at the oceanic crust-mantle boundary. *Geology*, *44*(2), 167–170. https://doi.org/10.1130/G37428.1

Snortum, E., & Day, J. M. D. (2020). Forearc origin for Coast Range Ophiolites inferred from osmium isotopes and highly siderophile elements. *Chemical Geology*, *550*, 119723. https://doi.org/https://doi.org/10.1016/j.chemgeo.2020.119723

Völkening, J., Walczyk, T., & Heumann, K. G. (1991). Osmium isotope ratio determinations by negative thermal ionization mass spectrometry. *International Journal of Mass Spectrometry and Ion Processes*, *105*(2), 147–159. https://doi.org/10.1016/0168-1176(91)80077-Z

Xiong, Q., Xu, Y., González-Jiménez, J. M., Liu, J., Alard, O., Zheng, J. P., Griffin, W. L., & O'Reilly, S. Y. (2020a). Sulfide in dunite channels reflects long-distance reactive migration of mid-ocean-ridge melts from mantle source to crust: A Re-Os isotopic perspective. *Earth and Planetary Science Letters*, *531*, 1–10. https://doi.org/10.1016/j.epsl.2019.115969

Xiong, Q., Xu, Y., González-Jiménez, J. M., Liu, J., Alard, O., Zheng, J. P., Griffin, W. L., & O'Reilly, S. Y. (2020b). Corrigendum to "Sulfide in dunite channels reflects long-distance reactive migration of mid-ocean-ridge melts from mantle source to crust: A Re-Os isotopic perspective" [Earth and Planetary Science Letters 531 (2020) 115969]. *Earth and Planetary Science Letters*, *535*, 1. https://doi.org/10.1016/j.epsl.2020.116136

Supplementary Table 1. Re and Os concentrations and Os isotope compositions of the studied Batin peridotites and UB-N and MUH-1 standards

Sample	Lithology	Depth (m)	Mass (g)	[Os] (ppb)	2σ error	[Re] (ppb)	2σ error	^{188}Os (M/g)	2σ error	$^{187}Re/^{188}Os$	2σ error	$(^{187}Os/^{188}Os)_m$	2σ error	$(^{187}Os/^{188}Os)_{95\ Ma}$	2σ error
BA4A 1	harzburgite	10.155	2.01412	4.411	0.000	0.641	0.039	3.08E-12	2.22E-14	0.701	0.043	0.12682	0.00057	0.12571	0.00057
BA4A 1-d_1			2.00379	6.123	0.000	0.599	0.039	4.27E-12	1.90E-13	0.471	0.037	0.12936	0.00145	0.12861	0.00145
BA4A 1-d_2			1.54518	4.295	0.000	0.564	0.005	3.00E-12	1.91E-14	0.633	0.007	0.12710	0.00054	0.12610	0.00054
BA4A 2	dunite	13.330	2.00336	4.354	0.000	1.203	0.039	3.04E-12	1.75E-14	1.331	0.044	0.12669	0.00055	0.12459	0.00055
BA4A 2-d			1.51420	3.916	0.000	1.277	0.052	2.73E-12	1.54E-14	1.572	0.064	0.12450	0.00059	0.12201	0.00060
BA4A 6	harzburgite	100.245	2.00763	5.375	0.000	0.096	0.039	3.76E-12	1.64E-14	0.086	0.035	0.11684	0.00052	0.11671	0.00052
BA4A 5	dunite	95.625	2.00897	4.416	0.000	0.239	0.039	3.08E-12	1.40E-14	0.260	0.042	0.12696	0.00053	0.12655	0.00054
BA4A 5-d			1.52049	3.398	0.000			2.37E-12	3.05E-14			0.12762	0.00062	0.12846	0.00063
BA4A 10	harzburgite	197.205	2.00718	3.630	0.000			2.53E-12	1.11E-14			0.12548	0.00053	0.12552	0.00054
BA4A 11	dunite	214.170	2.08374	5.463	0.000	0.606	0.038	3.81E-12	9.90E-14	0.535	0.036	0.13812	0.00124	0.13728	0.00124
BA4A 11-d_1			1.52127	4.552	0.000	0.485	0.051	3.17E-12	1.78E-14	0.514	0.054	0.13682	0.00054	0.13601	0.00055
BA4A 11-d_2			1.54478	4.686	0.000	0.631	0.002	3.27E-12	3.71E-14	0.649	0.008	0.13641	0.00053	0.13538	0.00053
BA4A 11-d_3			1.62985	4.286	0.000	0.496	0.002	2.99E-12	3.17E-14	0.559	0.006	0.13675	0.00051	0.13586	0.00051
BA4A 16	harzburgite	293.975	2.00632	3.861	0.000	0.295	0.039	2.70E-12	1.24E-14	0.368	0.049	0.12354	0.00054	0.12296	0.00054
BA4A 14	dunite	274.205	2.03097	5.191	0.000	0.539	0.039	3.62E-12	3.90E-14	0.501	0.036	0.13097	0.00061	0.13018	0.00061
BA4A 14-d_1			1.55373	4.269	0.000	0.542	0.050	2.98E-12	1.61E-14	0.612	0.057	0.12644	0.00055	0.12547	0.00055
BA4A 14-d_2			1.56883	4.185	0.000	0.507	0.002	2.92E-12	1.87E-14	0.584	0.004	0.12736	0.00051	0.12644	0.00051
BA4A 14-d_3			1.52166	4.198	0.000	0.483	0.002	2.93E-12	2.42E-14	0.554	0.005	0.12769	0.00053	0.12681	0.00053
Standards															
MUH-1 4			1.53566	4.096	0.000	0.276	0.051	2.86E-12	9.46E-15	0.325	0.060	0.12658	0.00052		
UB-N 5			2.00186	3.436	0.000	0.243	0.039	2.40E-12	1.26E-14	0.341	0.055	0.12725	0.00055		
UB-N 6			1.61348	3.298	0.000	0.240	0.002	2.30E-12	9.59E-15	0.351	0.003	0.12780	0.00052		
UB-N 7			1.53837	3.426	0.000	0.191	0.010	2.39E-12	9.16E-15	0.269	0.014	0.12690	0.00051		

Re and Os concentrations and Os isotopic compositions in whole rock powders were analyzed at the CRPG laboratory in Nancy (France) using MC-ICPMS (Neptune +) and N-TIMS (Finnigan MAT 262) (Os). All uncertainties are 2 σ and include all recognized sources of uncertainty, including in-run analytical precision, reproducibility of standard analyses, uncertainties related to the variability of the blank and its isotope composition, uncertainties related to the age correction (95 Ma). Duplicate analyses were performed for several samples (noted "-d") and the UB-N standard.

Supplementary Table 2. HSE concentrations of the studied Batin peridotites and UB-N and MUH-1 standards

Sample	Lithology	Depth (m)	Mass (g)	[Os] (ppb)	2σ error	[Ir] (ppb)	2σ error	[Ru] (ppb)	2σ error	[Pt] (ppb)	2σ error	[Pd] (ppb)	2σ error	[Re] (ppb)	2σ error	Ir/Os	Ir/Ru	Pd/Ir	Re/Os
BA4A 1	harzburgite	10.155	2.01412	4.411	0.000	4.305	0.002	6.931	0.023	9.960	0.012	7.194	0.011	0.641	0.039	0.98	0.62	1.67	0.15
BA4A 1-d_1			2.00379	6.123	0.000	3.834	0.002	6.508	0.023	9.488	0.013	7.566	0.011	0.599	0.039	0.63	0.59	1.97	0.10
BA4A 1-d_2			1.54518	4.295	0.000									0.564	0.005				0.13
BA4A 2	dunite	13.330	2.00336	4.354	0.000	3.115	0.001	6.691	0.023	7.809	0.012	5.931	0.011	1.203	0.039	0.72	0.47	1.90	0.28
BA4A 2-d			1.51420	3.916	0.000	2.672	0.001	6.205	0.030	7.383	0.016	5.379	0.015	1.277	0.052	0.68	0.43	2.01	0.33
BA4A 6	harzburgite	100.245	2.00763	5.375	0.000	3.787	0.001	8.283	0.023	4.972	0.012	3.069	0.011	0.096	0.039	0.70	0.46	0.81	0.02
BA4A 5	dunite	95.625	2.00897	4.416	0.000	3.314	0.001	7.671	0.023	8.344	0.012	6.965	0.011	0.239	0.039	0.75	0.43	2.10	0.05
BA4A 5-d			1.52049	3.398	0.000	2.419	0.001	6.349	0.030	5.599	0.016	6.948	0.015			0.71	0.38	2.87	
BA4A 10	harzburgite	197.205	2.00718	3.630	0.000	2.797	0.001	5.620	0.023	6.830	0.012	4.312	0.011			0.77	0.50	1.54	
BA4A 11	dunite	214.170	2.08374	5.463	0.000	3.035	0.001	7.439	0.022	8.588	0.012	9.205	0.011	0.606	0.038	0.56	0.41	3.03	0.11
BA4A 11-d_1			1.52127	4.552	0.000	3.055	0.002	6.390	0.030	8.587	0.016	8.320	0.015	0.485	0.051	0.67	0.48	2.72	0.11
BA4A 11-d_2			1.54478	4.686	0.000									0.631	0.002				0.13
BA4A 11-d_3			1.62985	4.286	0.000									0.496	0.002				0.12
BA4A 16	harzburgite	293.975	2.00632	3.861	0.000	3.630	0.001	6.139	0.023	6.271	0.012	4.129	0.011	0.295	0.039	0.94	0.59	1.14	0.08
BA4A 14	dunite	274.205	2.03097	5.191	0.000	3.127	0.001	7.174	0.023	9.324	0.012	10.088	0.011	0.539	0.039	0.60	0.44	3.23	0.10
BA4A 14-d_1			1.55373	4.269	0.000	3.372	0.002	7.058	0.030	9.127	0.016	12.816	0.015	0.542	0.050	0.79	0.48	3.80	0.13
BA4A 14-d_2			1.56883	4.185	0.000									0.507	0.002				0.12
BA4A 14-d_3			1.52166	4.198	0.000									0.483	0.002				0.12
Standards																			
MUH-1 4			1.53566	4.096	0.000	2.613	0.001	5.654	0.030	20.991	0.015	8.931	0.015	0.276	0.051	0.64	0.46	3.42	0.07
UB-N 5			2.00186	3.436	0.000	2.756	0.001	5.882	0.023	6.746	0.012	10.436	0.013	0.243	0.039	0.80	0.47	3.79	0.07
UB-N 6			1.61348	3.298	0.000									0.240	0.002				0.07
UB-N 7			1.53837	3.426	0.000									0.191	0.010				0.06

HSE concentrations in whole rock powders were analyzed at the CRPG laboratory in Nancy (France) using MC-ICPMS (Neptune +) and N-TIMS (Finnigan MAT 262) (Os). All uncertainties are 2 σ and include all recognized sources of uncertainty, including in-run analytical precision, reproducibility of standard analyses, uncertainties related to the variability of the blank and its isotope composition, uncertainties related to the age correction (95 Ma). Duplicate analyses were performed for several samples (noted "-d") and the UB-N standard.

Supplementary Table 3. Different components of the uncertainties on HSE concentrations and Os isotope compositions entering into the total uncertainties

Sample	Mass	Associated blank		[Os] uncertainty			^{188}Os uncertainty			Measured ^{187}Os/^{188}Os uncertainty				
		Os	Re	measurement	due to blank variability	Total	measurement	due to blank variability	Total	measurement	due to variability of blank ^{188}Os	due to variability of blank ^{187}Os/^{188}Os	due to long term reproducibility of standard	Total
	(g)			(2σ-m) (ppb)	(2σ)	(2σ)	(2σ-m) (M/g)	(2σ)	(2σ)	(2σ-m)	(2σ)	(2σ)	(2σ)	(2σ)
BA4A 1	2.01412	a	a	0.032	0.000	0.032	2.22E-14	8.95E-17	2.22E-14	0.00026	0.00000	0.00001	0.00050	0.00057
BA4A 1-d$_1$	2.00379	a	a	0.273	0.000	0.273	1.90E-13	8.99E-17	1.90E-13	0.00136	0.00000	0.00001	0.00050	0.00145
BA4A 1-d$_2$	1.54518	b	b	0.027	0.000	0.027	1.91E-14	1.23E-18	1.91E-14	0.00020	0.00000	0.00000	0.00050	0.00054
BA4A 2	2.00336	a	a	0.025	0.000	0.025	1.75E-14	8.99E-17	1.75E-14	0.00022	0.00000	0.00001	0.00050	0.00055
BA4A 2-d	1.51420	a	a	0.022	0.000	0.022	1.54E-14	1.19E-16	1.54E-14	0.00032	0.00000	0.00001	0.00050	0.00059
BA4A 6	2.00763	a	a	0.023	0.000	0.023	1.64E-14	8.97E-17	1.64E-14	0.00014	0.00000	0.00001	0.00050	0.00052
BA4A 5	2.00897	a	a	0.020	0.000	0.020	1.40E-14	8.97E-17	1.40E-14	0.00019	0.00000	0.00001	0.00050	0.00053
BA4A 5-d	1.52049	a	a	0.044	0.000	0.044	3.05E-14	1.18E-16	3.05E-14	0.00037	0.00000	0.00002	0.00050	0.00062
BA4A 10	2.00718	a	a	0.016	0.000	0.016	1.11E-14	8.98E-17	1.11E-14	0.00018	0.00000	0.00001	0.00050	0.00053
BA4A 11	2.08374	a	a	0.142	0.000	0.142	9.90E-14	8.65E-17	9.90E-14	0.00114	0.00000	0.00001	0.00050	0.00124
BA4A 11-d$_1$	1.52127	a	a	0.026	0.000	0.026	1.78E-14	1.18E-16	1.78E-14	0.00021	0.00000	0.00001	0.00050	0.00054
BA4A 11-d$_2$	1.54478	b	b	0.053	0.000	0.053	3.71E-14	1.23E-18	3.71E-14	0.00018	0.00000	0.00000	0.00050	0.00053
BA4A 11-d$_3$	1.62985	b	b	0.045	0.000	0.045	3.17E-14	1.16E-18	3.17E-14	0.00011	0.00000	0.00000	0.00050	0.00051
BA4A 16	2.00632	a	a	0.018	0.000	0.018	1.24E-14	8.98E-17	1.24E-14	0.00020	0.00000	0.00001	0.00050	0.00054
BA4A 14	2.03097	a	a	0.056	0.000	0.056	3.90E-14	8.87E-17	3.90E-14	0.00035	0.00000	0.00001	0.00050	0.00061
BA4A 14-d$_1$	1.55373	a	a	0.023	0.000	0.023	1.61E-14	1.16E-16	1.61E-14	0.00022	0.00000	0.00001	0.00050	0.00055
BA4A 14-d$_2$	1.56883	b	b	0.027	0.000	0.027	1.87E-14	1.21E-18	1.87E-14	0.00008	0.00000	0.00000	0.00050	0.00051
BA4A 14-d$_3$	1.52166	b	b	0.035	0.000	0.035	2.42E-14	1.25E-18	2.42E-14	0.00018	0.00000	0.00000	0.00050	0.00053
Standards														
MUH-1 4	1.53566	a	a	0.014	0.000	0.014	9.45E-15	1.17E-16	9.46E-15	0.00016	0.00000	0.00001	0.00050	0.00052
UB-N 5	2.00186	a	a	0.018	0.000	0.018	1.26E-14	9.00E-17	1.26E-14	0.00023	0.00000	0.00001	0.00050	0.00055
UB-N 6	1.61348	b	b	0.014	0.000	0.014	9.59E-15	1.18E-18	9.59E-15	0.00015	0.00000	0.00000	0.00050	0.00052
UB-N 7	1.53837	b	b	0.013	0.000	0.013	9.16E-15	1.23E-18	9.16E-15	0.00010	0.00000	0.00000	0.00050	0.00051

Supplementary Table 3 (suite). Different components of the uncertainties on HSE concentrations and Os isotope compositions entering into the total unce

Sample	[Re] uncertainty			Total ^{187}Re uncertainty	^{187}Re/^{188}Os uncertainty	Effect of ^{187}Re/^{188}Os uncertainty on ^{187}Os/^{188}Os age	Total uncertainty initial ^{187}Os/^{188}Os	Total ^{187}Os/^{188}Os uncertainty
	measurement (2σ-m) (ppb)	due to blank variability (2σ)	Total (2σ)	(2σ) (M/g)	(2σ)	(2σ)	(2σ)	(%)
BA4A 1	0.005	0.039	0.039	1.32E-13	0.043	0.00007	0.00057	0.45
BA4A 1-d_1	0.004	0.039	0.039	1.32E-13	0.037	0.00006	0.00145	1.13
BA4A 1-d_2	0.004	0.002	0.005	1.54E-14	0.007	0.00001	0.00054	0.43
BA4A 2	0.003	0.039	0.039	1.31E-13	0.044	0.00007	0.00055	0.44
BA4A 2-d	0.003	0.052	0.052	1.74E-13	0.064	0.00010	0.00060	0.49
BA4A 6	0.000	0.039	0.039	1.31E-13	0.035	0.00006	0.00052	0.45
BA4A 5	0.001	0.039	0.039	1.31E-13	0.042	0.00007	0.00054	0.43
BA4A 5-d	0.000	0.000	0.000				0.00063	0.49
BA4A 10	0.000	0.009	0.009				0.00054	0.43
BA4A 11	0.000	0.038	0.038	1.26E-13	0.036	0.00006	0.00124	0.90
BA4A 11-d_1	0.000	0.051	0.051	1.73E-13	0.054	0.00009	0.00055	0.40
BA4A 11-d_2	0.001	0.002	0.002	6.21E-15	0.008	0.00001	0.00053	0.39
BA4A 11-d_3	0.001	0.002	0.002	5.78E-15	0.006	0.00001	0.00051	0.38
BA4A 16	0.000	0.039	0.039	1.31E-13	0.049	0.00008	0.00054	0.44
BA4A 14	0.000	0.039	0.039	1.29E-13	0.036	0.00006	0.00061	0.47
BA4A 14-d_1	0.000	0.050	0.050	1.69E-13	0.057	0.00009	0.00055	0.44
BA4A 14-d_2	0.000	0.002	0.002	5.97E-15	0.004	0.00001	0.00051	0.40
BA4A 14-d_3	0.001	0.002	0.002	6.15E-15	0.005	0.00001	0.00053	0.42
Standards								
MUH-1 4	0.000	0.051	0.051	1.71E-13	0.060	0.00009	0.00053	0.42
UB-N 5	0.001	0.039	0.039	1.31E-13	0.055	0.00009	0.00056	0.44
UB-N 6	0.000	0.002	0.002	5.79E-15	0.003	0.00000	0.00052	0.41
UB-N 7	0.010	0.002	0.010	3.32E-14	0.014	0.00002	0.00051	0.40

Supplementary Table 3 (suite). Different components of the uncertainties on HSE concentrations and Os isotope compositions entering into the total uncertainties

Sample	[Ir] uncertainty			[Ru] uncertainty			[Pt] uncertainty			[Pd] uncertainty		
	measurement (2σ-m) (ppb)	due to blank variability (2σ)	Total (2σ)	measurement (2σ-m) (ppb)	due to blank variability (2σ)	Total (2σ)	measurement (2σ-m) (ppb)	due to blank variability (2σ)	Total (2σ)	measurement (2σ-m) (ppb)	due to blank variability (2σ)	Total (2σ)
BA4A 1	0.001	0.001	0.002	0.005	0.023	0.023	0.005	0.011	0.012	0.002	0.011	0.011
BA4A 1-d_1	0.001	0.001	0.002	0.005	0.023	0.023	0.005	0.011	0.013	0.003	0.011	0.011
BA4A 1-d_2												
BA4A 2	0.001	0.001	0.001	0.005	0.023	0.023	0.004	0.011	0.012	0.003	0.011	0.011
BA4A 2-d	0.001	0.001	0.001	0.004	0.030	0.030	0.005	0.015	0.016	0.002	0.015	0.015
BA4A 6	0.001	0.001	0.001	0.006	0.023	0.023	0.004	0.011	0.012	0.002	0.011	0.011
BA4A 5	0.001	0.001	0.001	0.005	0.023	0.023	0.005	0.011	0.012	0.002	0.011	0.011
BA4A 5-d	0.001	0.001	0.001	0.004	0.030	0.030	0.004	0.015	0.016	0.003	0.015	0.015
BA4A 10	0.001	0.001	0.001	0.004	0.023	0.023	0.004	0.011	0.012	0.002	0.011	0.011
BA4A 11	0.001	0.001	0.001	0.005	0.022	0.022	0.005	0.011	0.012	0.002	0.011	0.011
BA4A 11-d_1	0.001	0.001	0.002	0.005	0.030	0.030	0.005	0.015	0.016	0.002	0.015	0.015
BA4A 11-d_2												
BA4A 11-d_3												
BA4A 16	0.001	0.001	0.001	0.004	0.023	0.023	0.005	0.011	0.012	0.002	0.011	0.011
BA4A 14	0.001	0.001	0.001	0.005	0.022	0.023	0.005	0.011	0.012	0.001	0.011	0.011
BA4A 14-d_1	0.001	0.001	0.002	0.005	0.029	0.030	0.005	0.015	0.016	0.005	0.014	0.015
BA4A 14-d_2												
BA4A 14-d_3												
Standards												
MUH-1 4	0.000	0.001	0.001	0.004	0.030	0.030	0.004	0.015	0.015	0.004	0.014	0.015
UB-N 5	0.000	0.001	0.001	0.004	0.023	0.023	0.002	0.011	0.012	0.008	0.011	0.013
UB-N 6												
UB-N 7												

Supplementary Table 3 (suite). Different components of the uncertainties on HSE concentrations and Os isotope compositions entering into the total uncertainties

Notes:

Column C : Os blanks associated with two different analytical periods: a) 0.0007 ± 0.0002 ng, $^{187}Os/^{188}Os$ = 0.209 ± 0.122 (n = 3); b) 0.0010 ± 0.0000 ng (n = 2), $^{187}Os/^{188}Os$ = 0.220 ± 0.006 (n = 1); uncertainties 2σ

Column D: Re blanks associated with two different analytical periods: a) 0.042 ± 0.078 ng (n = 4); b) 0.022 ± 0.003 ng (n = 2); uncertainties 2σ

Column E : Based on in-run uncertainty on $^{190}Os/^{188}Os$ used in isotope dilution calculations

Column F From difference between [Os] corrected using Os blank + 2σ and [Os] corrected using Os blank - 2σ

Column G : Total uncertainty on [Os] based on combination of uncertainties in columns C and D (square root of individual values squared)

Column H : Based on in-run uncertainty on $^{190}Os/^{188}Os$ used in isotope dilution calculations

Column I : From difference between ^{188}Os corrected using Os blank + 2σ and ^{188}Os corrected using Os blank - 2σ

Column J : Total uncertainty on ^{188}Os based on combination of uncertainties in columns F and G

Column K : In-run uncertainty on $^{187}Os/^{188}Os$

Column L : From difference between $^{187}Os/^{188}Os$ corrected using ^{188}Os blank + 2σ and $^{187}Os/^{188}Os$ corrected using ^{188}Os blank - 2σ; blank $^{187}Os/^{188}Os$ held constant at mean value

Column M : From difference between $^{187}Os/^{188}Os$ corrected using $^{187}Os/^{188}Os$ blank + 2σ and $^{187}Os/^{188}Os$ corrected using $^{187}Os/^{188}Os$ blank - 2σ; blank ^{188}Os held constant at mean value

Column N : Long-term 2σ reproducibility of in-house liquid standard run by peak jumping on an ETP electron multiplier

Column O : Total uncertainty on $^{187}Os/^{188}Os$ based on combination of uncertainties in columns I through L

Column P : Based on in-run uncertainty on $^{187}Re/^{185}Re$ used in isotope dilution calculations

Column Q : From difference between [Re] corrected using Re blank + 2σ and [Re] corrected using Re blank - 2σ

Column R : Total uncertainty on [Re] based on combination of uncertainties in columns N and O (square root of individual values squared)

Column S : Total uncertainty on ^{187}Re - proportional to total uncertainty on [Re]

Column T : Total uncertainty on $^{187}Re/^{188}Os$ based on combination of uncertainties in columns H and Q

Column U : Uncertainty on age (95 Ma) corrected value of $^{187}Os/^{188}Os$ related to $^{187}Re/^{188}Os$ uncertainty.
Uncertainties on age correction related to ^{187}Re decay constant, ophiolite age and spike calibration are not considered as they should be very small and systematic for all samples (i.e., they cannot produce inter-sample variability)

Column V : Total uncertainty on initial $^{187}Os/^{188}Os$ based on combination of uncertainty on measured value (column M) and uncertainty related to age correction (column S)

Column X Based on in-run uncertainty on $^{191}Ir/^{193}Ir$ used in isotope dilution calculations

Column Y : From difference between [Ir] corrected using Ir blank + 2σ and [Ir] corrected using Ir blank - 2σ

Column Z : Total uncertainty on [Ir] based on combination of uncertainties in columns I and J (square root of individual values squared)

Column AA : Based on in-run uncertainty on $^{102}Ru/^{99}Ru$ used in isotope dilution calculations

Column AB : From difference between [Ru] corrected using Ru blank + 2σ and [Ru] corrected using Ru blank - 2σ

Column AC : Total uncertainty on [Ru] based on combination of uncertainties in columns L and M (square root of individual values squared)

Column AD : Based on in-run uncertainty on $^{194}Pt/^{195}Pt$ used in isotope dilution calculations

Column AE : From difference between [Pt] corrected using Pt blank + 2σ and [Pt] corrected using Pt blank - 2σ

Column AF : Total uncertainty on [Pt] based on combination of uncertainties in columns O and P (square root of individual values squared)

Column AG : Based on in-run uncertainty on $^{108}Pd/^{106}Pd$ used in isotope dilution calculations

Column AH : From difference between [Pd] corrected using Pd blank + 2σ and [Pd] corrected using Pd blank - 2σ

Column AI : Total uncertainty on [Pd] based on combination of uncertainties in columns R and S (square root of individual values squared)

Supplementary Table 4. Re and Os concentrations and Os isotope compositions of Oman harzburgites and the three types of dunites and of the reference materials (Klaessens, 2021; Klaessens et al., 2021)

Sample	Massif	Lithology	Hzb/Dun pairs	Normalized height in the section	Mass	[Os]	2σ error	[Re]	2σ error	^{188}Os	2σ error	$^{187}Re/^{188}Os$	2σ error	$(^{187}Os/^{188}Os)_m$	2σ error	$(^{187}Os/^{188}Os)_{95\ Ma}$	2σ error	T_{RD} age
					(g)	(ppb)		(ppb)		(M/g)								(Ga)
Moho Transition Zone (MTZ) peridotites																		
10 OM 25	Sumail (Maqsad)	pl-impregnated dunite		0.030	1.09260	0.399	0.002	0.114	0.007	2.77E-13	1.40E-15	1.376	0.090	0.1421	0.0005	0.1400	0.0006	-1.8
10 OM 45C	Sumail (Maqsad)	pure dunite		0.030	1.08114	0.947	0.002	0.050	0.007	6.60E-13	1.69E-15	0.255	0.038	0.1446	0.0006	0.1442	0.0006	-2.1
18 OK 26	Sumail (Maqsad)	cpx-bearing dunite		0.040	1.53157	0.628	0.000	0.409	0.051	4.37E-13	8.76E-16	3.149	0.393	0.1499	0.0006	0.1449	0.0009	-2.9
10 OM 5C*	Sumail (Mansah)	pure dunite		0.025	1.01170	1.063	0.002			7.40E-13	1.72E-15			0.1423	0.0005	0.1411	0.0005	-1.8
10 OM 5C-d					1.00295			0.168	0.008			0.760	0.037					
07 OD 1	Sumail (Mansah)	dunite		0.050	1.07011	0.390	0.002	0.199	0.008	2.71E-13	1.43E-15	2.462	0.100	0.1415	0.0005	0.1376	0.0006	-1.7
16 OL 11B	Wadi Tayin	pure dunite		0.000	2.00833	1.173	0.005	0.033	0.038	8.16E-13	3.88E-15	0.137	0.158	0.1492	0.0008	0.1490	0.0008	-2.8
16 OL 34B	Wadi Tayin	pl/px-impregnated dunite / troctolite		0.028	2.00647	2.305	0.003	0.053	0.043	1.61E-12	5.70E-15	0.111	0.091	0.1321	0.0020	0.1319	0.0020	-0.3
Main mantle section (MMS) peridotites																		
16 OD 5C	Nakhl-Rustaq	pl-impregnated depleted harzburgite		0.007	2.03522	2.274	0.003	0.448	0.009	1.59E-12	5.28E-15	0.948	0.019	0.1198	0.0020	0.1183	0.0020	1.3
16 OD 5D	Nakhl-Rustaq	harzburgite		0.007	2.04176	4.211	0.003	0.152	0.009	2.94E-12	1.15E-14	0.174	0.010	0.1136	0.0012	0.1133	0.0012	2.2
16 OD 7	Nakhl-Rustaq	harzburgite		0.053	2.02020	2.921	0.003	0.025	0.009	2.04E-12	6.29E-15	0.042	0.015	0.1252	0.0016	0.1251	0.0016	0.6
16 OD $4D_{Hzb}$	Nakhl-Rustaq	harzburgite	16 OD $4D_{Dun}$	0.073	1.61671	5.519	0.007	0.358	0.054	3.86E-12	5.01E-14	0.312	0.047	0.1174	0.0005	0.1169	0.0005	1.7
16 OD 9C	Nakhl-Rustaq	harzburgite	16 OD 9A	0.089	2.03326	3.691	0.003	0.130	0.009	2.57E-12	2.33E-14	0.170	0.012	0.1287	0.0013	0.1284	0.0013	0.1
16 OD 2	Nakhl-Rustaq	harzburgite		0.241	2.02082	4.314	0.003	0.500	0.009	3.01E-12	8.44E-15	0.559	0.010	0.1299	0.0011	0.1290	0.0011	0.0
16 OD 1A	Nakhl-Rustaq	harzburgite	16 OD 1B	0.337	1.72667	4.164	0.006	0.599	0.050	2.91E-12	2.05E-14	0.693	0.058	0.1235	0.0006	0.1224	0.0006	0.8
16 OD 10	Nakhl-Rustaq	harzburgite		0.419	2.07269	4.855	0.003	0.381	0.009	3.39E-12	3.19E-14	0.378	0.009	0.1311	0.0011	0.1305	0.0011	-0.2
11 OD 15A	Sumail	harzburgite		0.280	1.00937	3.894	0.002	0.152	0.008	2.72E-12	2.22E-14	0.187	0.010	0.1178	0.0006	0.1175	0.0006	1.6
07 OD 24	Sumail	harzburgite		0.254	1.03742	4.826	0.002	0.460	0.011	3.36E-12	1.35E-14	0.459	0.011	0.1345	0.0005	0.1338	0.0005	-0.7
07 OD 27B	Sumail	harzburgite		0.344	1.02319	4.314	0.002	0.221	0.008	3.01E-12	9.53E-15	0.247	0.009	0.1282	0.0005	0.1278	0.0005	0.2
07 OD 8C	Sumail	harzburgite		0.150	1.04900	5.246	0.002	0.379	0.010	3.66E-12	2.31E-14	0.348	0.009	0.1296	0.0007	0.1291	0.0007	0.0
07 OD 8C-d					1.01024	5.228	0.002	0.321	0.008	3.65E-12	2.41E-14	0.295	0.008	0.1257	0.0006	0.1252	0.0006	0.5
16 OD 4C	Nakhl-Rustaq	pl/cpx-impregnated dunite (vein)	(16 OD $4D_{Hzb}$)	0.073	1.56818	1.120	0.007	0.305	0.055	7.81E-13	4.92E-15	1.312	0.239	0.1347	0.0010	0.1327	0.0011	-0.7
16 OD $4D_{Dun}$	Nakhl-Rustaq	cpx-impregnated dunite (vein)	16 OD $4D_{Hzb}$	0.073	1.53878	5.954	0.007	0.414	0.056	4.15E-12	2.08E-14	0.335	0.046	0.1273	0.0005	0.1268	0.0005	0.3
16 OD 9A	Nakhl-Rustaq	pure dunite (band)	16 OD 9C	0.089	2.04511	11.802	0.003	0.431	0.009	8.21E-12	6.48E-14	0.177	0.004	0.1486	0.0006	0.1483	0.0006	-2.7
16 OD 1B	Nakhl-Rustaq	px-bearing dunite (vein)	16 OD 1A	0.337	2.02651	3.145	0.005	0.087	0.043	2.19E-12	9.82E-15	0.134	0.066	0.1332	0.0006	0.1330	0.0006	-0.5
16 OD 1B-d					2.01184	4.353	0.005	0.094	0.043	3.04E-12	1.15E-14	0.104	0.048	0.1314	0.0006	0.1312	0.0006	-0.2
16 OD 31	Wadi Tayin	px-bearing dunite (band)		0.116	2.00913	2.147	0.003	0.910	0.009	1.50E-12	6.50E-15	2.043	0.023	0.1281	0.0021	0.1249	0.0021	0.2
Basal peridotites																		
16 OD 13C	Nakhl-Rustaq	harzburgite	16 OD 13B	0.637	2.01014	4.415	0.005	0.415	0.043	3.08E-12	1.17E-14	0.453	0.047	0.1261	0.0005	0.1254	0.0005	0.5
16 OD 13C-d					2.01725	4.076	0.005	0.379	0.043	2.84E-12	2.00E-14	0.448	0.051	0.1265	0.0006	0.1258	0.0006	0.4
16 OL 25	Wadi Tayin	harzburgite		0.724	2.02610	6.289	0.003	0.081	0.009	4.38E-12	3.93E-14	0.062	0.007	0.1346	0.0009	0.1345	0.0009	-0.7
16 OL 26B	Wadi Tayin	harzburgite	16 OL 26A	0.724	2.01238	3.214	0.003	0.022	0.032	2.24E-12	8.84E-15	0.032	0.048	0.1215	0.0015	0.1215	0.0015	1.1
16 OL 27B	Wadi Tayin	harzburgite	16 OL 27A	0.784	2.01118	4.843	0.003	0.314	0.009	3.38E-12	2.68E-14	0.312	0.009	0.1252	0.0011	0.1247	0.0011	0.6
16 OL 27C	Wadi Tayin	harzburgite		0.784	2.00975	4.097	0.003	0.046	0.009	2.86E-12	1.75E-14	0.053	0.011	0.1131	0.0012	0.1131	0.0012	2.2
16 OL 28B	Wadi Tayin	cpx-bearing harzburgite		0.860	2.02988	4.481	0.003	0.168	0.043	3.13E-12	2.11E-14	0.180	0.046	0.1166	0.0011	0.1163	0.0011	1.8
16 OL 29	Wadi Tayin	cpx-bearing depleted harzburgite		0.872	2.03098	5.187	0.003	0.169	0.009	3.62E-12	2.54E-14	0.157	0.008	0.1226	0.0010	0.1223	0.0010	1.0
16 OL 24	Wadi Tayin	harzburgite		0.878	2.00603	5.475	0.003	0.221	0.009	3.82E-12	2.22E-14	0.194	0.008	0.1234	0.0010	0.1230	0.0010	0.9
16 OD 13B	Nakhl-Rustaq	px-bearing dunite (band)	16 OD 13C	0.637	1.57217	7.169	0.007	0.158	0.055	5.01E-12	3.04E-14	0.106	0.037	0.1216	0.0005	0.1214	0.0005	1.1
16 OD 15E	Nakhl-Rustaq	px-bearing dunite (band)		0.934	1.55944	2.291	0.007	0.106	0.056	1.60E-12	6.96E-15	0.223	0.117	0.1169	0.0007	0.1165	0.0007	1.7
16 OD 18B	Sumail	opx-bearing dunite (band)		0.969	2.01165	6.134	0.005	0.018	0.030	4.28E-12	4.84E-14	0.014	0.024	0.1280	0.0006	0.1280	0.0006	0.2
16 OD 19A	Sumail	pure dunite (band)		0.946	2.00354	0.774	0.005	0.066	0.043	5.41E-13	3.81E-15	0.413	0.269	0.1177	0.0011	0.1171	0.0012	1.6
16 OL 26A	Wadi Tayin	px-bearing dunite (band)	16 OL 26B	0.724	2.01473	4.460	0.003	0.014	0.029	3.11E-12	1.86E-14	0.015	0.031	0.1223	0.0011	0.1222	0.0011	1.0
16 OL 27A	Wadi Tayin	px-bearing dunite (band)	16 OL 27B	0.784	2.01151	4.998	0.003	0.079	0.009	3.49E-12	1.36E-14	0.077	0.009	0.1256	0.0010	0.1255	0.0010	0.6
14 11E	Haylayn	pure dunite (band)		0.990	1.03494	1.474	0.002	0.157	0.008	1.03E-12	2.98E-15	0.512	0.026	0.1257	0.0005	0.1249	0.0005	0.5

Supplementary Table 4 (suite). Re and Os concentrations and Os isotope compositions of Oman harzburgites and the three types of dunites and of the reference materials (Klaessens, 2021; Klaessens et al., 2021)

Sample	Massif	Lithology	Hzb/Dun pairs	Normalized height in the section	Mass	[Os]	2σ error	[Re]	2σ error	^{188}Os	2σ error	$^{187}Re/^{188}Os$	2σ error	$(^{187}Os/^{188}Os)_m$	2σ error	$(^{187}Os/^{188}Os)_{95\ Ma}$	2σ error	T_{RD} age
					(g)	(ppb)		(ppb)		(M/g)								(Ga)
Reference materials (UB-N, MUH-1, HARZ-01 and OKUM)																		
UB-N 1					1.52295	2.805	0.007	0.191	0.057	1.96E-12	1.11E-14	0.328	0.098	0.1279	0.0007	0.1274	0.0007	0.2
UB-N 2					1.71621	3.908	0.006	0.232	0.051	2.73E-12	1.39E-14	0.286	0.062	0.1274	0.0006	0.1270	0.0006	0.3
UB-N 3					2.00842	3.533	0.005	0.208	0.043	2.46E-12	8.70E-15	0.283	0.059	0.1272	0.0006	0.1268	0.0006	0.3
UB-N 4					2.04999	3.995	0.005	0.211	0.042	2.79E-12	1.99E-14	0.254	0.051	0.1272	0.0006	0.1268	0.0006	0.3
UB-N 5					2.00186	3.436	0.000	0.243	0.039			0.341		0.1273	0.0005	0.1267	0.0006	0.3
MUH-1 1					2.01885	4.111	0.005	0.222	0.043	2.87E-12	1.51E-14	0.260	0.050	0.1275	0.0006	0.1271	0.0006	0.3
MUH-1 2					2.00321	5.624	0.005	0.177	0.043	3.92E-12	1.70E-14	0.151	0.037	0.1271	0.0005	0.1269	0.0005	0.3
MUH-1 3					2.01237	5.808	0.005	0.186	0.043	4.05E-12	1.79E-14	0.154	0.036	0.1265	0.0005	0.1263	0.0005	0.4
MUH-1 4					1.53566	4.096	0.000	0.276	0.051			0.325		0.1266	0.0005	0.1261	0.0005	0.4
HARZ-01 1					2.03967	3.540	0.005	0.073	0.043	2.47E-12	1.16E-14	0.099	0.058	0.1261	0.0006	0.1259	0.0006	0.5
HARZ-01 2					2.02701	4.261	0.005	0.561	0.043	2.97E-12	3.14E-14	0.634	0.049	0.1273	0.0007	0.1263	0.0007	0.3
HARZ-01 3					2.01448	5.082	0.005	0.110	0.043	3.55E-12	2.57E-14	0.105	0.041	0.1259	0.0005	0.1257	0.0006	0.5
HARZ-01 4					2.01454	3.776	0.003	0.068	0.009	2.63E-12	8.27E-15	0.087	0.012	0.1278	0.0013	0.1276	0.0013	0.3
OKUM 1					2.00675	0.864	0.005	0.568	0.043	5.92E-13	4.59E-15	3.223	0.247	0.2630	0.0014	0.2579	0.0014	-22.1
OKUM 2					2.01264	1.030	0.005	0.541	0.043	7.08E-13	1.78E-13	2.572	0.680	0.2455	0.0011	0.2414	0.0015	-18.7

Re and Os concentrations and Os isotopic compositions in whole rock powders were analyzed at the CRPG laboratory in Nancy (France) using MC-ICPMS (Neptune +) and N-TIMS (Finnigan MAT 262) (Os). All uncertainties are 2 σ and include all recognized sources of uncertainty, including in-run analytical precision, reproducibility of standard analyses, uncertainties related to the variability of the blank and its isotope composition, uncertainties related to the age correction (95 Ma). Duplicate analyses were performed for several samples (noted "-d") and the reference materials (UB-N, MUH-1, HARZ-01 and OKUM). Samples belonging to harzburgite/dunite pairs collected in close proximity (<1 meter) are indicated. For each sample, an approximate estimation of its height in the mantle section was obtained by normalizing to the total section height to compare samples from different cross-sections. Re-depletion model ages (T_{RD}) were calculated by comparing measured $^{187}Os/^{188}Os$ values directly with the mantle evolution curve. They represent minimum ages of melt extraction and should not be equated with true ages.

** For 10 OM 5C sample, $(^{187}Os/^{188}Os)_{95\ Ma}$ was calculated using Re compositions of its duplicate.*

Hzb = harzburgite; Dun = dunite; Px = pyroxene; Opx = orthopyroxene; Cpx = clinopyroxene; Pl = plagioclase.

Supplementary Table 5. HSE concentrations of Oman harzburgites and the three types of dunites and of the reference materials (Klaessens, 2021; Klaessens et al., 2021)

Sample	Massif	Lithology	Hzb/Dun pairs	Normalized height in the section	Mass	[Os]	2σ error	[Ir]	2σ error	[Ru]	2σ error	[Pt]	2σ error	[Pd]	2σ error	[Re]	2σ error	Ir/Os	Ir/Ru	Pd/Ir	Re/Os
					(g)	(ppb)		(ppb)		(ppb)		(ppb)		(ppb)		(ppb)					
Moho Transition Zone (MTZ) peridotites																					
10 OM 25	Sumail (Maqsad)	pl-impregnated dunite		0.030	1.09260	0.399	0.002									0.114	0.007				0.29
10 OM 45C	Sumail (Maqsad)	pure dunite		0.030	1.08114	0.947	0.002									0.050	0.007				0.05
18 OK 26	Sumail (Maqsad)	cpx-bearing dunite		0.040	1.53157	0.628	0.000	0.240	0.001	1.057	0.030	0.726	0.015	1.320	0.015	0.409	0.051	0.38	0.23	5.50	0.65
10 OM 5C	Sumail (Mansah)	pure dunite		0.025	1.01170	1.063	0.002														
10 OM 5C-d					1.00295											0.168	0.008				
07 OD 1	Sumail (Mansah)	dunite		0.050	1.07011	0.390	0.002									0.199	0.008				0.51
16 OL 11B	Wadi Tayin	pure dunite		0.000	2.00833	1.173	0.005	1.265	0.011	1.673	0.006	0.854	0.075	0.100	0.000	0.033	0.038	1.08	0.76	0.08	0.03
16 OL 34B	Wadi Tayin	pl/px-impregnated dunite / troctolite		0.028	2.00647	2.305	0.003	2.220	0.011	4.012	0.009	6.185	0.076	1.873	0.307	0.053	0.043	0.96	0.55	0.84	0.02
Main mantle section (MMS) peridotites																					
16 OD 5C	Nakhl-Rustaq	pl-impregnated depleted harzburgite		0.007	2.03522	2.274	0.003	1.429	0.011	4.531	0.016	5.221	0.076	5.743	0.303	0.448	0.009	0.63	0.32	4.02	0.20
16 OD 5D	Nakhl-Rustaq	harzburgite		0.007	2.04176	4.211	0.003	2.299	0.011	6.620	0.023	4.692	0.075	1.222	0.302	0.152	0.009	0.55	0.35	0.53	0.04
16 OD 7	Nakhl-Rustaq	harzburgite		0.053	2.02020	2.921	0.003	3.886	0.013	5.360	0.019	13.143	0.079	3.415	0.305	0.025	0.009	1.33	0.72	0.88	0.01
16 OD 4D$_{Hzb}$*	Nakhl-Rustaq	harzburgite	16 OD 4D$_{Dun}$	0.073	1.61671	5.519	0.007	3.940	0.026	7.079	0.308	6.531	0.122	3.545	0.021	0.358	0.054	0.71	0.56	0.90	0.06
16 OD 9C	Nakhl-Rustaq	harzburgite	16 OD 9A	0.089	2.03326	3.691	0.003	2.878	0.012	4.778	0.017	5.425	0.076	4.055	0.303	0.130	0.009	0.78	0.60	1.41	0.04
16 OD 2	Nakhl-Rustaq	harzburgite		0.241	2.02082	4.314	0.003	3.755	0.013	6.622	0.023	9.379	0.078	0.866	0.305	0.500	0.009	0.87	0.57	0.23	0.12
16 OD 1A*	Nakhl-Rustaq	harzburgite	16 OD 1B	0.337	1.72667	4.164	0.006	3.594	0.025	5.860	0.282	6.914	0.120	3.986	0.022	0.599	0.050	0.86	0.61	1.11	0.14
16 OD 10	Nakhl-Rustaq	harzburgite		0.419	2.07269	4.855	0.003	4.109	0.013	7.742	0.028	8.669	0.075	7.198	0.298	0.381	0.009	0.85	0.53	1.75	0.08
11 OD 15A	Sumail	harzburgite		0.280	1.00937	3.894	0.002									0.152	0.008				0.04
07 OD 24	Sumail	harzburgite		0.254	1.03742	4.826	0.002									0.460	0.011				0.10
07 OD 27B	Sumail	harzburgite		0.344	1.02319	4.314	0.002									0.221	0.008				0.05
07 OD 8C	Sumail	harzburgite		0.150	1.04900	5.246	0.002									0.379	0.010				0.07
07 OD 8C-d					1.01024	5.228	0.002									0.321	0.008				0.06
16 OD 4C*	Nakhl-Rustaq	pl/cpx-impregnated dunite (vein)	(16 OD 4D$_{Hzb}$)	0.073	1.56818	1.120	0.007	0.738	0.005	1.042	0.309	3.224	0.124	2.113	0.017	0.305	0.055	0.66	0.71	2.86	0.27
16 OD 4D$_{Dun}$*	Nakhl-Rustaq	cpx-impregnated dunite (vein)	16 OD 4D$_{Hzb}$	0.073	1.53878	5.954	0.007	4.692	0.030	8.485	0.334	11.727	0.173	3.756	0.032	0.414	0.056	0.79	0.55	0.80	0.07
16 OD 9A	Nakhl-Rustaq	pure dunite (band)	16 OD 9C	0.089	2.04511	11.802	0.003	4.820	0.015	17.233	0.073	20.894	0.082	6.203	0.302	0.431	0.009	0.41	0.28	1.29	0.04
16 OD 1B	Nakhl-Rustaq	px-bearing dunite (vein)	16 OD 1A	0.337	2.02651	3.145	0.005	1.828	0.011	5.712	0.012	2.877	0.075	0.514	0.304	0.087	0.043	0.58	0.32	0.28	0.03
16 OD 1B-d					2.01184	4.353	0.005	1.792	0.011	8.332	0.017	3.564	0.075	0.570	0.306	0.094	0.043	0.41	0.22	0.32	0.02
16 OD 31	Wadi Tayin	px-bearing dunite (band)		0.116	2.00913	2.147	0.003	3.023	0.012	2.307	0.010	4.918	0.077	0.220	0.307	0.910	0.009	1.41	1.31	0.07	0.42
Basal peridotites																					
16 OD 13C	Nakhl-Rustaq	harzburgite	16 OD 13B	0.637	2.01014	4.415	0.005	3.664	0.012	6.697	0.014	9.624	0.077	5.606	0.307	0.415	0.043	0.83	0.55	1.53	0.09
16 OD 13C-d					2.01725	4.076	0.005	2.962	0.012	6.451	0.005	8.706	0.076	5.691	0.306	0.379	0.043	0.73	0.46	1.92	0.09
16 OL 25	Wadi Tayin	harzburgite		0.724	2.02610	6.289	0.003	4.396	0.014	9.102	0.033	11.228	0.078	8.501	0.305	0.081	0.009	0.70	0.48	1.93	0.01
16 OL 26B	Wadi Tayin	harzburgite	16 OL 26A	0.724	2.01238	3.214	0.003	1.872	0.011	5.612	0.012	6.252	0.076	3.596	0.306	0.022	0.032	0.58	0.33	1.92	0.01
16 OL 27B	Wadi Tayin	harzburgite	16 OL 27A	0.784	2.01118	4.843	0.003	3.256	0.012	6.791	0.024	8.150	0.077	8.491	0.307	0.314	0.009	0.67	0.48	2.61	0.06
16 OL 27C	Wadi Tayin	harzburgite		0.784	2.00975	4.097	0.003	3.774	0.013	6.558	0.023	3.090	0.076	0.585	0.307	0.046	0.009	0.92	0.58	0.15	0.01
16 OL 28B	Wadi Tayin	cpx-bearing harzburgite		0.860	2.02988	4.481	0.003	3.451	0.012	6.902	0.014	5.904	0.075	0.654	0.304	0.168	0.043	0.77	0.50	0.19	0.04
16 OL 29	Wadi Tayin	cpx-bearing depleted harzburgite		0.872	2.03098	5.187	0.003	3.948	0.013	8.173	0.029	8.738	0.077	5.101	0.304	0.169	0.009	0.76	0.48	1.29	0.03
16 OL 24	Wadi Tayin	harzburgite		0.878	2.00603	5.475	0.003	3.524	0.013	7.285	0.026	7.521	0.077	4.489	0.308	0.221	0.009	0.64	0.48	1.27	0.04
16 OD 13B*	Nakhl-Rustaq	px-bearing dunite (band)	16 OD 13C	0.637	1.57217	7.169	0.007	2.815	0.021	7.816	0.311	2.386	0.119	2.686	0.019	0.158	0.055	0.39	0.36	0.95	0.02
16 OD 15E*	Nakhl-Rustaq	px-bearing dunite (band)		0.934	1.55944	2.291	0.007	0.873	0.007	3.623	0.310	1.226	0.125	0.389	0.020	0.106	0.056	0.38	0.24	0.45	0.05
16 OD 18B	Sumail	opx-bearing dunite (band)		0.969	2.01165	6.134	0.005	2.032	0.011	10.651	0.022	4.365	0.076	1.362	0.306	0.018	0.030	0.33	0.19	0.67	0.00
16 OD 19A	Sumail	pure dunite (band)		0.946	2.00354	0.774	0.005	0.316	0.011	1.774	0.006	1.296	0.075	0.200	0.308	0.066	0.043	0.41	0.18	0.63	0.09
16 OL 26A	Wadi Tayin	px-bearing dunite (band)	16 OL 26B	0.724	2.01473	4.460	0.003	3.307	0.012	7.149	0.014	6.112	0.076	3.701	0.306	0.014	0.029	0.74	0.46	1.12	0.00
16 OL 27A	Wadi Tayin	px-bearing dunite (band)	16 OL 27B	0.784	2.01151	4.998	0.003	1.257	0.011	3.508	0.013	0.395	0.075	0.150	0.306	0.079	0.009	0.25	0.36	0.12	0.02
14 11E	Haylayn	pure dunite (band)		0.990	1.03494	1.474	0.002									0.157	0.008				0.11

Supplementary Table 5 (suite). HSE concentrations of Oman harzburgites and the three types of dunites and of the reference materials (Klaessens, 2021; Klaessens et al., 2021)

Sample	Massif	Lithology	Hzb/Dun pairs	Normalized height in the section	Mass	[Os]	2σ error	[Ir]	2σ error	[Ru]	2σ error	[Pt]	2σ error	[Pd]	2σ error	[Re]	2σ error	Ir/Os	Ir/Ru	Pd/Ir	Re/Os
					(g)	(ppb)		(ppb)		(ppb)		(ppb)		(ppb)		(ppb)					
Reference materials (UB-N, MUH-1, HARZ-01 and OKUM)																					
UB-N 1*					1.52295	2.805	0.007	1.497	0.011	5.025	0.329	6.808	0.138	6.119	0.081	0.191	0.057	0.53	0.30	4.09	0.07
UB-N 2*					1.71621	3.908	0.006	2.749	0.015	5.730	0.287	7.231	0.123	5.687	0.029	0.232	0.051	0.70	0.48	2.07	0.06
UB-N 3					2.00842	3.533	0.005	3.157	0.024	5.804	0.012	6.549	0.078	5.674	0.309	0.208	0.043	0.89	0.54	1.80	0.06
UB-N 4					2.04999	3.995	0.005	3.650	0.025			7.256	0.077	5.368	0.305	0.211	0.042	0.91		1.47	0.05
UB-N 5					2.00186	3.436	0.000	2.756	0.001	5.882	0.023	6.746	0.012	10.436	0.013	0.243	0.039	0.80	0.47	3.79	0.07
MUH-1 1					2.01885	4.111	0.005	3.951	0.027			8.134	0.080	9.570	0.343	0.222	0.043	0.96		2.42	0.05
MUH-1 2					2.00321	5.624	0.005	2.943	0.022	9.809	0.020	7.350	0.080	8.230	0.314	0.177	0.043	0.52	0.30	2.80	0.03
MUH-1 3					2.01237	5.808	0.005	3.915	0.012	5.846	0.008	25.628	0.084	8.359	0.306	0.186	0.043	0.67	0.67	2.14	0.03
MUH-1 4					1.53566	4.096	0.000	2.613	0.001	5.654	0.030	20.991	0.015	8.931	0.015	0.276	0.051	0.64	0.46	3.42	0.07
HARZ-01 1					2.03967	3.540	0.005	2.319	0.021	6.731	0.010	9.438	0.200	7.372	0.321	0.073	0.043	0.66	0.34	3.18	0.02
HARZ-01 2					2.02701	4.261	0.005	2.317	0.011	5.075	0.007	10.511	0.076	4.998	0.304	0.561	0.043	0.54	0.46	2.16	0.13
HARZ-01 3					2.01448	5.082	0.005	2.717	0.012	5.574	0.008	8.795	0.076	5.680	0.306	0.110	0.043	0.53	0.49	2.09	0.02
HARZ-01 4					2.01454	3.776	0.003	3.409	0.013	5.170	0.019	8.771	0.077	13.127	0.308	0.068	0.009	0.90	0.66	3.85	0.02
OKUM 1					2.00675	0.864	0.005	0.909	0.011	4.387	0.023	14.607	0.078	11.638	0.315	0.568	0.043	1.05	0.21	12.81	0.66
OKUM 2					2.01264	1.030	0.005	1.032	0.013	5.916	0.022	13.135	0.081	11.343	0.313	0.541	0.043	1.00	0.17	10.99	0.53

HSE concentrations in whole rock powders were analyzed at the CRPG laboratory in Nancy (France) using N-TIMS (Finnigan MAT 262) (Os), MC-ICP-MS (Neptune +) and Q-ICP-MS (XSERIES). All uncertainties are 2 σ and include all recognized sources of uncertainty, including in-run analytical precision, reproducibility of standard analyses, uncertainties related to the variability of the blank and its isotope composition. Duplicate analyses were performed for several samples (noted "-d") and the reference materials (UB-N, MUH-1, HARZ-01 and OKUM). Samples belonging to harzburgite/dunite pairs collected in close proximity (<1 meter) are indicated. For each sample, an approximate estimation of its height in the mantle section was obtained by normalizing to the total section height to compare samples from different cross-sections.

** Analyses using Q-ICP-MS XSERIES.*

Hzb = harzburgite; Dun = dunite; Px = pyroxene; Opx = orthopyroxene; Cpx = clinopyroxene; Pl = plagioclase